Multimodal resonant plasmonic antennas and their slot plasmonic counterparts

Zur Erlangung des akademischen Grades eines

DOKTOR-INGENIEURS

von der KIT-Fakultät für
Elektrotechnik und Informationstechnik
des Karlsruher Instituts für Technologie (KIT)

genehmigte

DISSERTATION

von

M.Sc. Nikola Bralović

Tag der mündlichen Prüfung: 04.11.2025
Hauptreferent: Prof. Dr. rer. nat. Uli Lemmer
Korreferent: Prof. Dr. rer. nat. habil. Marc Eichhorn

Acknowledgments

It is my pleasure to acknowledge all the people who were giving me support during my studies in Karlsruhe.

Firstly, I am grateful to my supervisor, Professor Dr Ulrich Lemmer, for his scientific support and for giving me the opportunity to participate in the EUROPHOTONICS Joint Doctorate Erasmus Mundus programme in this very interesting field.

Moreover, I would like to thank Dr. Mohamed Hussein for his huge scientific and organizational support.

I would also like to thank Dr. Hans Eisler for making me feel welcome as a visitor and for several years of insightful advice.

During my time at LTI, I was lucky to be surrounded by a great group and work environment.

I would also like to acknowledge the generous funding for this work, mainly provided by the EUROPHOTONICS Joint Doctorate Programme, but also to Light Technology Institute, KIT.

Finally, I am thankful to all my family, especially my wife, Jelena Uskoković, for making this long trip possible.

ABSTRACT

All subwavelength metallic nanostructures allow us to manipulate light on a nanoscale. By tuning the volume, shape, and dielectric function of these nanostructures surrounding the medium, we can control their near-field and far-field optical and near-infrared (near-IR) properties.

Plasmonic antennas have become very popular in recent years since they can enhance the field in small gaps beyond the diffraction limit. In this thesis, we investigate optical and near-IR resonant antennas. The antennas investigated in this thesis show monomodal, bimodal, and triple-modal resonant behavior in the optical and near-IR spectrum.

In this work, the behavior of nanoantennas was investigated and optimized using numerical simulations. Besides existing nanoantenna geometries, this work contributes to a better understanding of novel antenna concepts. It is shown that the behavior of different antenna types can be optimized simply by changing elementary parameters like antenna length or gap size. Many antenna types, such as monomodal rod antennas (single and coupled versions), L-shaped bimodal antennas, and cross-shaped triple-modal and bimodal antennas, have been investigated before. However, there is a lack of literature that demonstrates essential scaling laws representing the relationship between antenna dimensions and resonant wavelengths. Moreover, there is a need for more research regarding field enhancement for L-shaped and cross-shaped coupled nanoantennas; especially, there is no research concerning cross-shaped triple-modal single antennas.

One of the main points of the thesis is the development of bimodal coupled L-shaped and cross-shaped antennas. This nanoantenna behavior is crucial for coupling with quantum emitters. Besides geometrical parameters, the behavior of nanoantennas is strongly influenced by polarization. Polarization angle deviation allows both resonances to be set independently of one another and also separated. Finally, a significant influence on resonant behavior has the dielectric properties of the antenna material and substrate.

While nanoantennas are already being used successfully for high-resolution microscopy and spectroscopy applications (Raman), this antenna can also be used as coupling elements in light-emitting diodes, optical sensors, and solar cells.

Monomodal plasmonic antennas, such as single ellipsoid-shaped and rod-shaped, coupled rod-shaped antennas, are studied in detail. It is found that the coupled L-shaped ROA with a very small 2 nm gap width exhibits field enhancements of 40 and 147.3 on the scale $|E_{TOT}|/|E_{IN}|$

for the high energy and low energy resonance, respectively. Also, it is found that the coupled cross-shaped ROA with a very small 2 nm gap width exhibits field enhancements of 45.9 and 149.4 on the scale $|E_{TOT}|/|E_{IN}|$ for the high energy and low energy resonance, respectively. For all the aforementioned plasmonic antennas, we investigated their slot antenna counterparts. Those slot antennas are rod-shaped, L-shaped, and cross-shaped holes in a gold layer that are deposited on the dielectric. In this part of the thesis, we rely on Babinet's principle. The aim of this work is to describe all these aforementioned antennas and provide a theoretical proposal for the design path of bimodal and triple-modal resonant plasmonic and slot antennas.

KURZFASSUNG

Alle metallischen Nanostrukturen unterhalb der Wellenlänge ermöglichen es uns, Licht auf einer Nanoskala zu manipulieren. Durch die Abstimmung des Volumens, der Form und der dielektrischen Funktion dieser Nanostrukturen, die das Medium umgeben, können wir ihre optischen Eigenschaften im Nah- und Fernfeld sowie im nahen Infrarot (nahes IR) steuern.

Plasmonische Antennen sind in den letzten Jahren sehr beliebt geworden, da sie das Feld in kleinen Lücken über die Beugungsgrenze hinaus verstärken können. In dieser Arbeit untersuchen wir optische und Nah-Infrarot-Resonanzantennen. Die in dieser Arbeit untersuchten Antennen zeigen monomodales, bimodales und trimodales Resonanzverhalten im optischen und Nah-Infrarot-Spektrum.

In dieser Arbeit wurde das Verhalten von Nanoantennen mithilfe numerischer Simulationen untersucht und optimiert. Neben den bestehenden Nanoantennen-Geometrien trägt diese Arbeit zu einem besseren Verständnis neuartiger Antennenkonzepte bei. Es wird gezeigt, dass das Verhalten verschiedener Antennentypen einfach durch die Änderung elementarer Parameter wie Antennenlänge oder Spaltgröße optimiert werden kann. Viele Antennentypen, wie monomodale Stabantennen (einzelne und gekoppelte Versionen), L-förmige bimodale Antennen und kreuzförmige trimodale und bimodale Antennen, wurden bereits untersucht. Es gibt jedoch nur wenige Literaturstellen, die die wesentlichen Skalierungsgesetze aufzeigen, die die Beziehung zwischen den Abmessungen der Antenne und den Resonanzwellenlängen darstellen. Darüber hinaus besteht weiterer Forschungsbedarf hinsichtlich der Feldverstärkung für L-förmige und kreuzförmige gekoppelte Nanoantennen; insbesondere gibt es keine Forschung zu kreuzförmigen dreifach-modalen Einzelantennen.

Einer der Hauptpunkte der Dissertation ist die Entwicklung bimodaler gekoppelter L- und kreuzförmiger Antennen. Dieses Verhalten von Nanoantennen ist für die Kopplung mit Quantenemittern von entscheidender Bedeutung. Neben geometrischen Parametern wird das Verhalten von Nanoantennen stark von der Polarisation beeinflusst. Durch die Abweichung des Polarisationswinkels können beide Resonanzen unabhängig voneinander eingestellt und auch getrennt werden. Schließlich haben die dielektrischen Eigenschaften des Antennenmaterials und des Substrats einen signifikanten Einfluss auf das Resonanzverhalten.

Während Nanoantennen bereits erfolgreich für hochauflösende Mikroskopie- und Spektroskopieanwendungen (Raman) eingesetzt werden, kann diese Antenne auch als Kopplungselement in Leuchtdioden, optischen Sensoren und Solarzellen verwendet werden.

Monomodale plasmonische Antennen, wie einzelne ellipsoid- und stabförmige, gekoppelte stabförmige Antennen, werden eingehend untersucht. Es wurde festgestellt, dass die gekoppelte L-förmige ROA mit einer sehr kleinen Spaltbreite von 2 nm Feldverstärkungen von 40 bzw. 147.3 auf der Skala $|E_{TOT}|/|E_{IN}|$ für die Hochenergie- bzw. Niederenergienresonanz aufweist. Außerdem wurde festgestellt, dass die gekoppelte kreuzförmige ROA mit einer sehr kleinen Spaltbreite von 2 nm Feldverstärkungen von 45.9 und 149.4 auf der Skala $|E_{TOT}|/|E_{IN}|$ für die Hochenergie- bzw. Niederenergienresonanz aufweist.

Für alle oben genannten plasmonischen Antennen haben wir ihre Gegenstücke in Form von Schlitzantennen untersucht. Diese Schlitzantennen sind stabförmige, L-förmige und kreuzförmige Löcher in einer Goldschicht, die auf dem Dielektrikum aufgebracht sind. In diesem Teil der Arbeit stützen wir uns auf das Babinetsche Prinzip. Das Ziel dieser Arbeit ist es, alle oben genannten Antennen zu beschreiben und einen theoretischen Vorschlag für den Entwurfspfad von bimodalen und trimodalen resonanten plasmonischen und Schlitzantennen zu liefern.

Contents

List of publications

1: Bralović, N., Lemmer, U. & Hussein, M. Asymmetric, “L-shaped resonant optical antennas with plasmon length tuning and high-electric field enhancement”, *Opt Quant Electron* 55, 824 (2023). https://doi.org/10.1007/s11082-023-05117-9

2: Bralović, N., Lemmer, U. & Hussein, M., “Asymmetric Cross-Shaped Optical Antennas with Wide Spectral Tunability and High Optical Cross-Sections,” *Plasmonics* 19, 179–191 (2024). https://doi.org/10.1007/s11468-023-01969-9

3: Semenov, A. and Charaev, I. and Lusche, R. and Ilin, K. and Siegel, M. and Hübers, H.-W. and Bralović, N. and Dopf, K. and Vodolazov, D. Yu., “Asymmetry in the effect of magnetic field on photon detection and dark counts in bended nanostrips”, Phys. Rev. B 92, 174518 (2015). https://doi.org/10.1103/PhysRevB.92.174518

1 Introduction and motivation

1.1 Introduction

Nanophotonics is one of the fundamental research areas on which modern science is based. Photonics became very important after the big “boom” of high-speed CPUs in the 1990s. By this time, the miniaturization of these devices had become one of the biggest challenges, and nanophotonics took a leading role in the scientific community because photonic devices can operate at much higher frequencies than standard microelectronic devices.

Plasmonics is a new area in nanophotonics and one of the most interesting subjects of light-matter interaction. Roughly speaking, plasmons are electromagnetic (EM) waves at the interface between metal and the surrounding dielectric that can operate at optical frequencies. They can also localize the EM field at the boundary between the metal and the dielectric. Due to this ability, plasmons are very sensitive to any changes in the metallic surface (without altering the volume of the metal), and scientists manipulate this behavior intensely since this characteristic provides many applications. One of the essential characteristics of metals that exhibit plasmonic behavior is the ability to confine the field in the vicinity of the metal in space, which is much smaller than the incident light wavelength [1].

Around every metal, there exists a cloud of electrons. If that metal has a negative real and positive imaginary dielectric constant due to the interaction with EM radiation, it exhibits coherent oscillations of its surface electrons. These oscillations are surface plasmons, which propagate along the metal-medium surface. If EM radiation interacts with nanoparticles much smaller than the operating wavelengths, then surface plasmons are called localized surface plasmons.

In the high-frequency (THz) regime (visible and near-IR), metals exhibit considerable dissipation, posing challenges for all nanophotonic devices and their performance. As previously mentioned, the dielectric function of these metals is an important variable related to dissipation characteristics.

For a long time, metallic nanostructures have been observed to exhibit resonant behavior in the optical and near-IR spectral ranges. These structures have become particularly interesting

because of their unique properties when interacting with light, which causes collective oscillations of the free electrons at the metal-dielectric interface. This amplifies the electromagnetic field near the particle, which is spatially confined to a few nanometers. That is why light can be controlled below the diffraction limit. Resonant metallic nanostructures can efficiently convert freely propagating optical radiation to localized energy and vice versa. In general, research on plasmonics holds promising applications in nanooptics. One of the most important research topics in plasmonics is resonant optical antennas, especially following significant advances in nanofabrication. Considerable research efforts have been devoted to investigating the relationship between RF and optical antennas and their analogy. In this thesis, we numerically investigate optical antennas and their applications.

The thesis begins with fundamental theory and develops into an investigation of bimodal L-shaped and cross-shaped resonant optical antennas. This bimodal behavior is crucial for surface-enhanced Raman spectroscopy (SERS), nano-router design, and optical vortex phase plate applications. Additionally, quantum emitters and molecules are coupled to different plasmonic structures with resonant behavior, utilizing an optical antenna's ability to boost the signal. Since plasmonic nanostructures also show resonant behavior in the infrared spectrum (IR), they can be used in Fourier-transform infrared spectroscopy (FTIR), allowing for measurements of the signal in the far-field region. Optical antennas could be used for future high-bandwidth communication at the nanoscale.

1.2 Thesis structures

Theoretically, the Maxwell equations based on antenna theory should be length-invariant, but frequency-dependent material properties lead to deviations from the classic antenna.

This thesis consists of several chapters. After an introduction and motivation in Chapter 1, Chapter 2 describes the fundamental theory of electromagnetism, scattering models, and antennas. Chapter 3 explains the numerical simulation methodology used in the thesis. Chapter 4 describes various optical antennas, especially bimodal and triple-modal plasmonic optical and near-infrared, and L-shaped and cross-shaped antennas. Also, this chapter includes a literature review. Finally, Chapter 5 investigates slot antennas as resonant optical antenna counterparts.

1.3 Context and motivation of the study

As well known, resonant optical antennas (ROAs) can enhance the electromagnetic field in their vicinity and scatter the EM wave in the far-field [1, 2]. They are very promising structures due to their ability to convert free-propagating optical radiation to localized energy efficiently and vice versa [2, 3, 4, 5, 6, 7]. Due to the collective oscillations of the free carriers confined to the metal particle volume or so-called localized surface plasmon resonances, noble metal nanoparticles are prominent for their volume-dependent scattering and absorption properties that furthermore can be tuned throughout the visible and NIR wavelength range by shaping their specific geometry, their materials composition properties and their environment [8]. Resonant behaviour can be influenced by the length scale over which the free-electron oscillation occurs. Therefore, the resonance design toolbox parameter, the so-called plasmon length, is introduced [9]. This parameter is very useful if we want to tune the response in the vis/NIR-wavelength region and the locally enhanced fields for some specific application needs. The enhanced field is localized in the volume below the diffraction limit [10, 11]. Their ability to exhibit strong field enhancement in the gap makes them suitable for coupling with quantum emitters [12, 13, 14, 15] but also for other purposes like nanodimers, Fano resonances, and SERS [16, 17, 18, 19]. Moreover, highly localized near-fields at certain frequencies and specific light polarization conditions are essential for new nonlinear optical effects, such as nonlinear plasmonics via four-wave mixings [20]. Finally, nanoantennas are used in the latest generation of photovoltaic devices [21]. Different shapes for nanoantennas have already been investigated. Those are V-shaped [22], “bowtie”-shaped [23], and Yagi-Uda [24] nanoantennas. In this thesis will be examined L-shaped plasmonic antennas and cross-shaped plasmonic antennas. As is shown in previous research, L-shaped antennas can show bimodal behavior [25, 26, 27, 28, 29, 30, 31, 32, 33, 34, 35]. It is worth mentioning that [34] analyzed the coupling of L-shaped nanodimers to investigate second harmonic generation over the transition from capacitive to conductive coupling. Also, in [35], different polarization conditions for symmetric L-shaped structures are examined to design ultra-thin optical vortex phase plates (VPP), which can generate optical vortex beams with different topological charges. However, there was a lack of literature that in detail describes asymmetric L-shaped nanoantennas, especially the polarization nature of these antennas and mode behavior for both single and coupled versions. Therefore, another work is published [36]. Previous research also shows that cross-shaped antennas exhibit bimodal behavior [37, 38, 39]. Later, it was published

in detail, describing different types of cross-shaped nanoantennas concerning the symmetry level, mode reconstruction, and polarization sensitivity [40]. That work also found that cross-shaped nanoantenna can also show triple-modal behavior besides bimodal behavior under some geometrical and polarization conditions. Both of these antenna types are low-symmetry and polarization-sensitive. The coupled version is investigated for both antenna types, and they both exhibit two tunable resonances in the optical and near-infrared wavelength regions with ultra-high field enhancement in the gaps. In an already published paper, cross-shaped nanoantennas exhibit a field enhancement of 45.9 for the high energy resonance (700 nm-800 nm wavelength region) and 149.4 for the low energy resonance (900 nm-1000 nm wavelength region), respectively, on $|E_{TOT}|/|E_{IN}|$ scale. On the other hand, it is found that the coupled L-shaped ROA with a very small 2 nm gap width exhibits field enhancements 40 and 147.3 on scale $|E_{TOT}|/|E_{IN}|$ for the high energy and low energy resonance, respectively.
Table 1 summarizes the current study compared to the previous work.

Table 1: Comparison of the suggested design with similar structures

Ref no.	Design	No of resonant peaks	Resonance wavelengths	Gap (nm)	Field Enhancement (FE)	
[41]	Bowtie	1	1100 nm	5	86	
[42]	Bowtie	3	960 nm, 1050 nm, 1400 nm	2	35, 5, 82	
[40]	Cross-shaped ROA	2 (for coupled version)	766 nm, 952 nm	2	45.9, 149.4	
[36]	L-shaped ROA	2 (for coupled version)	692 nm, 1086 nm	2	40, 147.3	

The reported designs [36, 40] offer two or even three resonance modes, i.e., bimodal or three-modal longitudinal antenna resonance behavior with a high enhancement factor. These two resonances can be selectively excited by changing the linear polarization angle. The obtained

results and the analysis open a new route for multiple plasmon resonance devices with ultra-high field enhancement that can be easily integrated with future nano-optical circuits operating at multiple frequencies.

1.4 Objectives and research contributions

This thesis investigates asymmetric L-shaped and cross-shaped resonant optical antennas, both single and coupled versions, in detail for the first time. The biggest numerical investigation challenge is finding a correlation between the size of the optical antenna geometry and resonant wavelengths.

2 Antenna, theory, and parameters

In 1968, Viktor Veselago first described materials with negative dielectric permittivity and magnetic permeability [43]. In that paper he covered some fundamental topics that were proved many years later. Specifically, plasmonics is a field of optics that investigates the impact of EM waves in optical and IR ranges in nanostructured materials. The dispersion formula which describes EM wave propagation in materials is:

$$\frac{\omega^2}{c^2} \cdot \varepsilon_{xy} \cdot \mu_{xy} - k^2 \cdot \delta_{xy} + k_x \cdot k_y = 0 \tag{2.1}$$

In this equation, material parameters are ε_{xy} and μ_{xy} represented as components of tensor dielectric permittivity and magnetic permeability. δ_{xy} is Kronecker delta, ω is wave frequency, and k is the vector wave. This formula is simplified for isotropic materials:

$$\frac{\omega^2}{c^2} \cdot \varepsilon \cdot \mu = k^2 \tag{2.2}$$

2.1 Wave equation

Investigating Maxwell's equations is vital in wave optics because of their physical meaning. As a first step, we need to employ macroscopic Maxwell equations. These equations are fundamental in classical electrodynamics, which describe the theory of the propagation of electromagnetic waves by summarizing the theories for the description of electric and magnetic fields together. They were established by Scottish scientist James Clerk Maxwell, a mathematician in the mathematical physics field, in 1865 [44]. They can describe both the spatial and temporal behavior of the wave or light in the medium. Here will be shown macroscopic Maxwell equations in differential form in the time domain, which include vectorial differential operators $\nabla \cdot$ (divergence) and $\nabla \times$ (curl).

1. Faraday's law is a principle concerning electromagnetic induction. In the case of a wire loop, any change in magnetic field can induce electromotive force and current in this wire. Negative changes in magnetic flux through this loop over time are equal to the electromotive force. Maxwell-Faraday equation describes the relation between the changing of the electric field in space and the changing of the magnetic flux in time.

$$\nabla \times \vec{E}(\vec{r}, t) = -\frac{\partial \vec{B}(\vec{r}, t)}{\partial t} \tag{2.3}$$

2. Amper-circuit law relates the sum of magnetic fields across the closed loop to the electric current that passes through the loop. The differential formula would be:

$$\nabla \times \vec{H}(\vec{r},t) = -\frac{\partial \vec{D}(\vec{r},t)}{\partial t} + \vec{J}_e(\vec{r},t) \tag{2.4}$$

3. Gauss's law of electric charges states that the electric flux through a closed surface is proportional to the total electric charge enclosed by this surface:

$$\nabla \cdot \vec{D}(\vec{r},t) = \rho_e(\vec{r},t) \tag{2.5}$$

4. Gauss's law of magnetic charges states that the divergence of the magnetic field is 0.

$$\nabla \cdot \vec{B}(\vec{r},t) = 0 \tag{2.6}$$

Here $\vec{E}$ is the electric field, $\vec{B}$ is magnetic flux density, $\vec{D}$ is an electric displacement field, $\vec{H}$ magnetic field strength, $\vec{J}_e$ is free current density, and ρ_e is volume charge density.

Time harmonic form of Maxwell equations

Wave equations depict the propagation of light in the medium. For homogenous wave equations, Maxwell equations can be modified since $\vec{J}_e = 0$ and $\rho_e = 0$. Now equations (2.5) and (2.6) become:

$$Gauss\ law\ of\ electric\ charges: \quad \nabla \cdot \vec{D}(\vec{r},t) = 0 \tag{2.7}$$

$$Gauss\ law\ of\ magnetic\ charges: \ \nabla \cdot \vec{B}(\vec{r},t) = 0 \tag{2.8}$$

For lossless, isotropic, and linear media, the dielectric function and magnetic permeability are not variables but constants. Therefore:

$$\vec{D}(\vec{r},t) = \varepsilon_0 \cdot \varepsilon_r \cdot \vec{E}(\vec{r},t) \tag{2.9}$$

$$\vec{B}(\vec{r},t) = \mu_0 \cdot \mu_r \cdot \vec{H}(\vec{r},t) \tag{2.10}$$

Here, magnetic susceptibility is $\mu_r = 1$

If in equations (2.3) and (2.4) are used, equations (2.9) and (2.10), the result will be:

$$\nabla \times \vec{E}(\vec{r},t) = -\mu_0 \cdot \frac{\partial \vec{H}(\vec{r},t)}{\partial t} \tag{2.11}$$

$$\nabla \times \vec{H}(\vec{r},t) = \varepsilon_0 \cdot \varepsilon_r \cdot \frac{\partial \vec{E}(\vec{r},t)}{\partial t} \tag{2.12}$$

By applying the curl operator on equation (2.11), the equation is:

$$\nabla \times \nabla \times \vec{E}(\vec{r},t) = \nabla \times (-\mu_0 \cdot \frac{\partial \vec{H}(\vec{r},t)}{\partial t}) = -\mu_0 \cdot \frac{\partial (\nabla \times \vec{H}(\vec{r},t))}{\partial t} \tag{2.13}$$

By using the Amper-Maxwell circuit law and equations (2.9) and (2.13), we obtain the following:

$$\nabla \times \nabla \times \vec{E}(\vec{r},t) = -\mu_0 \cdot \varepsilon_0 \cdot \varepsilon_r \cdot \frac{\partial^2 \vec{E}(\vec{r},t)}{\partial t^2} \tag{2.14}$$

If it is used well-known formula for speed light in a specific medium, the formula is:

$$\nabla \times \nabla \times \vec{E}(\vec{r},t) = -\frac{1}{c^2} \cdot \frac{\partial^2 \vec{E}(\vec{r},t)}{\partial t^2} \tag{2.15}$$

From the vector theory, there is an identity:

$$\nabla \times \nabla \times \vec{E}(\vec{r},t) = \nabla \cdot (\nabla \cdot \vec{E}(\vec{r},t)) - \nabla^2 \vec{E}(\vec{r},t) \tag{2.16}$$

For lossless, isotropic, and linear media, the formula for Gauss law for electric charges can be applied to the electric field, not only to the electric field displacement. Thus, equation (2.16) becomes:

$$\nabla^2 \vec{E}(\vec{r},t) - \frac{1}{c^2} \cdot \frac{\partial^2 \vec{E}(\vec{r},t)}{\partial t^2} = 0 \tag{2.17}$$

In time-harmonic form, the electric field is:

$$\vec{E}(\vec{r},t) = \vec{E}_0 \cdot e^{-j \cdot \omega \cdot t} \tag{2.18}$$

Combining (2.17) and (2.18) result is:

$$\nabla^2 \vec{E}(\vec{r},t) + \frac{\omega^2}{c^2} \cdot \vec{E}(\vec{r},t) = 0 \tag{2.19}$$

In further analysis will be introduced wave number:

$$k = \frac{2 \cdot \pi}{\lambda} = \frac{\omega}{c} \cdot \varepsilon_r = k_0 \cdot \varepsilon_r \tag{2.20}$$

Finally, wave equations for the electric field in the time-harmonic form are:

$$\nabla^2 \vec{E}(\vec{r},t) + k^2 \cdot \vec{E}(\vec{r},t) = 0 \tag{2.21}$$

The same procedure can be applied to a magnetic field, which gives:

$$\nabla^2 \vec{H}(\vec{r},t) + k^2 \cdot \vec{H}(\vec{r},t) = 0 \tag{2.22}$$

These equations are general 3D wave equations for electric and magnetic fields. Later, these equations will be used intensively in surface plasmon polaritons analysis and boundary conditions.

2.2 Electromagnetism of Metals

Metals are well-known as reflective materials in the EM frequency band. However, in optical and near-IR regimes, EM waves penetrate through metal, which causes dissipation. If the frequency rises, we are talking about the UV band, and in that frequency range, metal behaves almost like a dielectric. No matter which dispersive property of the metal is discussed, each can be described by a complex dielectric function. The interaction between EM and metals can be described by applying Maxwell equations. This interaction became interesting a couple of years after Thomson discovered the electron.

2.2.1 Drude model

Around 1900, Paul Drude developed a new model to explain the transport properties of electrons in metals. According to this model, the position of the surface plasmon band of metallic nanoparticles depends heavily on the surrounding medium [45]. Whether we analyze sub-wavelength apertures [46], nano-waveguides [47], or nanoantennas [48, 49], we need to investigate the optical response of the medium to the external EM field. Of course, classical electrodynamics is always a good starting point to perform this investigation. In Drude model, several assumptions are made. Metals have two components – ions, which are heavy, static, and immersed in a cloud of light, and electrons, which can easily move and form an electron gas. This electron gas is in relation to Maxwell-Boltzmann statistics. A critical assumption is that electron-electron interactions are neglected. Therefore, Drude only analyses ion-electron interactions, not electron-electron interactions. When these electrons impact the positive part of the atom, damping occurs. The oscillation of the electron gas can be approximated as a harmonic oscillator. Here, we can introduce tau as the relaxation time, the time between two collisions. In equations, the physical quantity $\gamma = 1/\tau$, which is the collision frequency. At room temperature, the typical value would be around 100THz. So, Drude model sees the metal as a mass of positively charged ions. From that mass of ions, a number of free electrons are detached. The assumption is this: metal comes in contact with some surrounding medium. Therefore, the valence level of the metal atom comes in contact with the potential of an atom

of the surrounding medium, and that contact causes the localization of electrons. The surface plasmon band can be range from 500 nm to 550 nm for gold nanoparticles. The exact value of the source depends on the surrounding medium (particularly its refractive index). With the increase in the refractive index of the surrounding medium, the surface plasmon band shifts toward the lower energy band (or toward longer wavelengths). Also, chemical reactions between the material and the surface of the metal could cause shifting of the plasmon band due to a changed distribution of free electrons. Here, we can make one analogy. Ohm's law introduces conductivity, a value that depends on the material from which the conductor is made. So, the external electric field ($\vec{E}$) causes electron movement, and therefore, current density ($\vec{J}$).

$$\vec{J} = \sigma \cdot \vec{E} \tag{2.23}$$

On the other hand, Drude model can estimate the movement of electrons in the electron gas as a result of the applied external field with frequency ω. The external field is already expressed in (2.18). According to the free electron Drude model, oscillations of free electrons in an electron gas have π phase shift relative to the electromagnetic field [10]. This behavior is essential for surface plasmon resonance, where we need the negative permittivity of noble metals. A significant part of the plasmonic investigation is based on the frequency-dependent permittivity of the metal. Every metal has surface or volume charge density, and noble metals can sustain collective oscillations of those surface or volume charge densities with resonant waves called plasmons. Also, an essential part of the investigation is the dispersion relation of SPPs at the metal/insulator interface. Therefore, Maxwell's equations also need to be discussed. The behavior of noble metals in the optical and near-IR regimes could be described by the Drude and Lorentz models for the frequency-dependent complex permittivity. Drude model helps us understand how free electrons in metals interact with an external field at a particular frequency. Free electrons are not bound to any atom and can move without a restoring force [50]. Electric field (space and time-dependent) could be expressed in this form:

$$\vec{E}(\vec{r}, t) = R_e(E_0 \cdot \vec{e}_x \cdot e^{-i\omega t}) \tag{2.24}$$

There are two forces which are relevant for the oscillator in this model [10]:

$$\text{Driving force: } -e \cdot E_x = -e \cdot E_0 \cdot e^{-i\omega t} \tag{2.25}$$

$$\text{Damping force: } -m_e \cdot \gamma \cdot v = -m_e \cdot \gamma \cdot \frac{dx}{dt} \tag{2.26}$$

where γ is the damping rate, which is related to the electron mean free path caused by scattering events (or related to the rate of collisions between electrons that constitute the gas), and m_e and e are the free electrons' effective mass and electric charge. x is the electron displacement, and v is the velocity. Since, in Drude model, the electrons are not bound to the atomic core, there is no restoring force or resonance. Considering that there is no restoring force, the natural frequency ω_0 is zero. The Drude model equation for free-electron gas is:

$$m_e \cdot \frac{d^2x}{dt^2} + m_e \cdot \gamma \cdot \frac{dx}{dt} = -e \cdot E_0 \cdot e^{-i\omega t} \tag{2.27}$$

Since the applied field has harmonic dependence in time, we can suppose that the solution of this equation will also be harmonic. The solution of this equation can be represented as:

$$x(t) = A \cdot e^{-i\omega t} \tag{2.28}$$

If we substitute equation (2.28) into (2.27) we get:

$$A = \frac{e \cdot E_0}{m_e} \cdot \frac{1}{\omega^2 + i \cdot \gamma \cdot \omega} \tag{2.29}$$

Now displacement is:

$$x(t) = \frac{e \cdot E_0}{m_e} \cdot \frac{1}{\omega^2 + i \cdot \gamma \cdot \omega} \cdot e^{-i\omega t} \tag{2.30}$$

If we want to do vector analysis instead of scalar analysis, we have:

$$\vec{r}(t) = \vec{r}_0 \cdot e^{-i\omega t} \tag{2.31}$$

Based on this equation, we can calculate the derivative (first and second) and, therefore, velocity and acceleration:

$$\frac{d\vec{r}(t)}{dt} = -j \cdot \omega \cdot e^{-i\omega t} \tag{2.32}$$

$$\frac{d^2\vec{r}(t)}{dt^2} = -\omega^2 \cdot e^{-i\omega t} \tag{2.33}$$

Now, from the motion equation (2.27), we can get the final formula for the motion:

$$\vec{r}(t) = \frac{e}{m \cdot (\omega^2 + i \cdot \gamma \cdot \omega)} \cdot \vec{E}(t) \tag{2.34}$$

As might be seen, the amplitude oscillation of the free electron is complex. Here, we can observe the phase shift caused by the external EM field and its dependence on the collision rate between the free electrons and other electrons in the gas.

Unsurprisingly, we have complex values in response to an incident EM field. As it is well known, complex dielectric function has physical meaning in the case of conductors. As

mentioned, applying an external electric field over certain materials causes the movement of material charge carriers. That movement is described with $\vec{r}(t)$. Especially in noble metals where the density of free charge carriers is high, such movement generates an electric dipole momentum inside the material $\vec{p}$. Since we speak about the concentration of charge carriers, we can introduce macroscopic polarization:

$$\vec{P} = n \cdot \vec{p} \tag{2.35}$$

n is the volume concentration of charge carriers (or the number of charge carriers per unit volume). We assume that noble metals are linear, isotropic, and homogenous, which is very important for the relation between polarization and the electric field:

$$\vec{D}(\omega) = \varepsilon_0 \cdot \varepsilon_r \cdot \vec{P}(\omega) = \varepsilon_0 \cdot \vec{E}(\omega) + \vec{P}(\omega) \tag{2.36}$$

The formula for electric dipole moment is:

$$\vec{p} = -e \cdot \vec{r} \tag{2.37}$$

That equation gives us macroscopic polarization, where we introduce the concentration n:

$$\vec{P} = -n \cdot e \cdot \vec{r} \tag{2.38}$$

This equation can also be called dipole momentum per unit volume. If we combine the equation of motion with this equation, then we get:

$$\vec{P} = \frac{n \cdot e^2}{m_e} \cdot \frac{1}{-\omega^2 - i \cdot \gamma \cdot \omega} \cdot \vec{E} \tag{2.39}$$

At the same time, from equation (2.36) we can get:

$$\vec{P}(\omega) = \varepsilon_0 \cdot (\varepsilon_r - 1) \cdot \vec{E}(\omega) \tag{2.40}$$

Combining equations for relative permittivity and resonant macroscopic polarization, we obtain the complex permittivity of metals:

$$\varepsilon_r(\omega) = 1 - \frac{\omega_p^2}{\omega^2 + i \cdot \gamma \cdot \omega} \tag{2.41}$$

Here, we introduced volume plasma frequency:

$$\omega_p = \sqrt{\frac{n \cdot e^2}{\varepsilon_0 \cdot m_e}} \tag{2.42}$$

n is the concentration of free electrons (or the number of free electrons per volume unit) here. From the formula (2.41), we can find the real and imaginary parts of dielectric permittivity.

$$\varepsilon_{REAL} = 1 - \frac{\omega_p^2}{\omega^2 + \gamma^2} \tag{2.43}$$

$$\varepsilon_{IMAG} = 1 - \frac{\omega_p^2 \cdot \gamma}{\omega \cdot (\omega^2 + \gamma^2)} \tag{2.44}$$

Based on these formulas, we can also define complex refractive index from the relative permittivity and permeability:

$$\bar{n} = \sqrt{\varepsilon \cdot \mu} \tag{2.45}$$

Since relative permittivity is a complex number, the refractive index will also be a complex number. The real part is in relation to the phase velocity of light in that particular material, and the imaginary part is in relation to absorption in the material. That imaginary part is. Therefore, it is essential and significant when we want to analyze which amount of the EM wave can be scattered or absorbed by the nanoparticle. Now, we can explore this equation. If the frequency ω is below ω_p, metal will still have metallic character since ε_{REAL} is below 0. If we have a negative real part of the dielectric function, we have a very high k. Accordingly, EM waves can penetrate to a small length. On the other hand, if we analyze high frequencies, the damping factor can be considered negligible. If we analyze very high frequencies, the damping factor can be regarded as negligible. In that case, we have undamped free electron plasma, and equation (2.43) can be simplified:

$$\varepsilon_{REAL}(\omega) = 1 - \frac{\omega_p^2}{\omega^2} \tag{2.46}$$

If the frequency is higher than the plasma frequency, permittivity is positive, and the metal starts to exhibit dielectric behavior. Drude model is extended by Sommerfeld, who observed the electron gas not as a free gas. In this model, we are not proceeding with the electron mass but with the effective mass.

2.2.2 Lorentz model

Unfortunately, although Drude model predicts how the metal will behave in the IR regime, this model is unsuitable for higher frequency bands (or wavelengths shorter than 650nm) because interband transitions are neglected. The imaginary part of the dielectric function in that band is much higher than the value calculated by Drude model [10]. The explanation is that photons with high energy can excite electrons from lower-lying energy valence bands to higher energy conduction bands. This model treats electrons as damped harmonic oscillations bound to the atomic nucleus. What does the classical Lorentz dipole oscillator actually describe? Every atom

has its own "natural" frequencies (but here, we consider only one resonant frequency). If the oscillating EM field has the same frequency as the atom (ω), the system will go into a resonant state, and the atom can absorb the energy. Otherwise, the atom is optically transparent. That EM field causes the harmonic motion of electrons, that are bound to atoms. The Lorentz dipole oscillator describes this behavior. So, besides the driving and damping forces that we had in Drude model (equations (2.25) and (2.26)), here we introduce bound electrons, which are influenced by restoring force and can be described using the mass-spring system or spring force. Therefore, there is one more relevant force for oscillators:

$$\text{Spring force:} \quad k_{SPRING} \cdot x \tag{2.47}$$

m_b is the effective mass of bound electrons, and it should not be mixed with the mass of free electrons. k_{SPRING} is spring constant, which can be obtained from:

$$\omega_0 = \sqrt{\frac{k_{SPRING}}{m_b}} \tag{2.48}$$

γ is the damping rate related to the radiative damping in the case of bound electrons. The presence of natural frequency ω_0 is proof that the electron is bounded. Now, the new motion equation is:

$$m_b \cdot \frac{d^2x}{dt^2} + m_b \cdot \gamma \cdot \frac{dx}{dt} + m_b \cdot \omega_0^2 \cdot x = -e \cdot E_0 \cdot e^{-i\omega t} \tag{2.49}$$

The rest of the mathematical operations are the same as in Drude model, but new variables exist. In the Drude model, we had a concentration of electrons, but here, we have a concentration of bound electrons to the atoms (N' instead of N). Finally, in Drude model, we had plasma frequency. Here we have:

$$\omega_p{}' = \sqrt{\frac{N' \cdot e^2}{\varepsilon_0 \cdot m_b}} \tag{2.50}$$

In Drude model, we had a movement:

$$\vec{r} = \frac{(e/m) \cdot \vec{E}}{\omega^2 + i \cdot \gamma \cdot \omega} \tag{2.51}$$

Here we have:

$$\vec{r} = \frac{(e/m_b) \cdot \vec{E}}{-\omega_0 + \omega^2 + i \cdot \gamma \cdot \omega} \tag{2.52}$$

In Drude model, we had a formula for the dielectric function:

$$\varepsilon_{r\_DRUDE}(\omega) = 1 - \frac{\omega_p^2}{\omega^2 + i \cdot \gamma \cdot \omega} \tag{2.53}$$

Here in Lorentz model we wave:

$$\varepsilon_{r\_LORENTZ}(\omega) = 1 - \frac{{\omega_p}'^2}{-{\omega_0}^2 + \omega^2 + i \cdot \gamma \cdot \omega} \tag{2.54}$$

We can express this equation as a separated real and imaginary part:

$$\varepsilon_{REAL\_LORENTZ} = \frac{({\omega_0}^2 - \omega^2 + {\omega_p}'^2) \cdot ({\omega_0}^2 - \omega^2) + \gamma^2 \cdot \omega^2}{({\omega_0}^2 - \omega^2)^2 + \gamma^2 \cdot \omega^2} \tag{2.55}$$

$$\varepsilon_{IMAG\_LORENTZ} = \frac{{\omega_p}'^2 \cdot \gamma \cdot \omega}{({\omega_0}^2 - \omega^2)^2 + \gamma^2 \cdot \omega^2} \tag{2.56}$$

Bound electrons transit from low energy to the conduction band by absorbing a photon. The natural frequency of ω_0 is directly proportional to the energy of that photon. Thus, we can say that ω_0 defines the resonant frequency that metal can have in interaction with an EM wave. In the "real world," there is no material with only one resonance; there are many. The reason is that bound electrons begin their transition from different levels. An electron that occupies one state (1s) needs a different amount of energy for photon absorption than the electron occupying another state (2s). Therefore, in some mathematical calculations, the sum or superposition of more than one resonance should be used. That would be called Lorentz's multiple oscillator. Based on equation (2.54) it can be written:

$$\varepsilon_{\mathrm{MULTIPLE\_LORENTZ}}(\omega) = 1 + \sum_{j=1}^{n} \frac{f_j \cdot {\omega_{p,j}}'^2}{{\omega_{0,j}}^2 - \omega^2 - i \cdot \Gamma_j \cdot \omega} \tag{2.57}$$

f_j represents oscillator strength. With the Lorentz-Drude model, we can calculate the dielectric constant of some noble metals, considering both free and bound electron effects. Of course, Johnson and Christy [51] and Palik [52] are widely recognized sources of optical constants of metals.

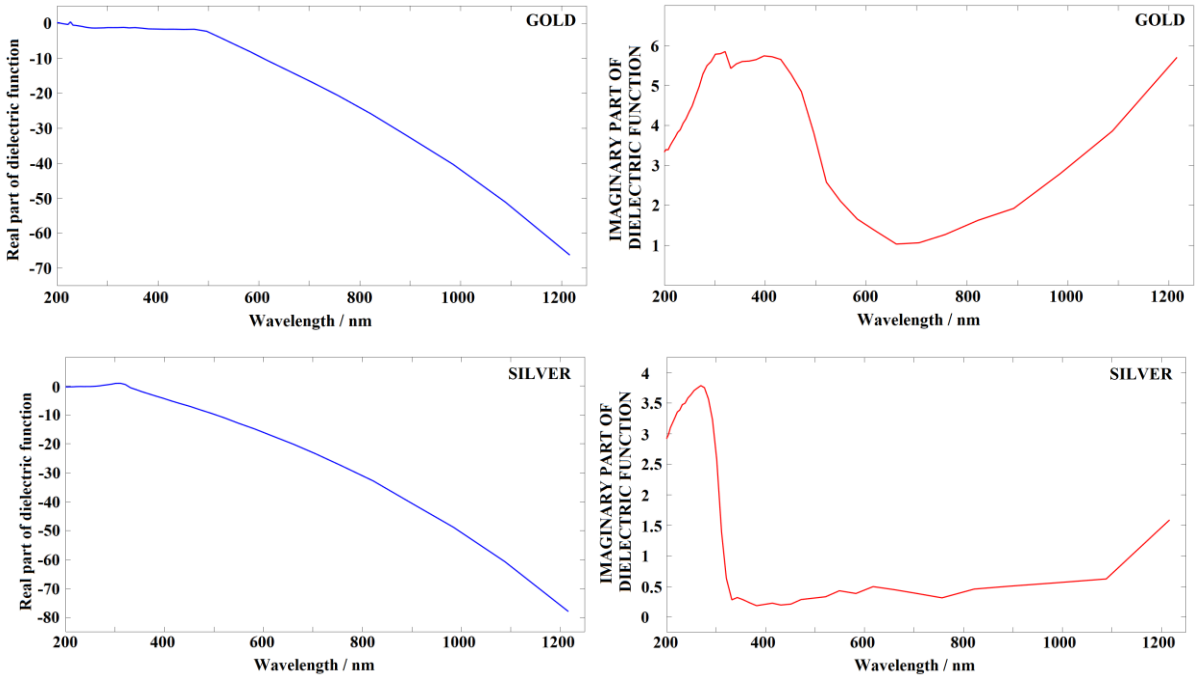

Figure 2.1: Gold and silver material properties - real and imaginary parts of dielectric function concerning the wavelength; values are taken from the literature [51].

As shown in Figure 2.1, silver has a much larger real part than the imaginary part of the dielectric function, so it is considered a low-loss material. It has a high melting point, good conductivity, and an interband transition region in the UV range. Since the UV region is very far from the infrared range, the bound electron effect explained by Lorentz is not included in the calculation of optical constants for silver.

2.2.3 Lorentz-Drude Model

This model combines both previous models, with which we can describe material through several transition bands:

$$\varepsilon_{\text{LORENTZ–DRUDE}}(\omega) = 1 - \frac{\omega_p^2}{\omega^2 + i \cdot \gamma \cdot \omega} + \sum_{\text{j=1}}^{\text{n}} \frac{f_j \cdot {\omega_{\text{p,j}}}'^2}{{\omega_{0,\text{j}}}^2 - \omega^2 - \text{i} \cdot \Gamma_\text{j} \cdot \omega} \tag{2.58}$$

It is evident that these models can successfully represent the dielectric function of metals. However, due to the high sensitivity of plasmonic behavior to the dielectric function, we rely on experimental data. The complex dielectric function $\varepsilon(\omega)$ and the complex refractive index of the medium are related through these formulas:

$$\bar{n} = n(\omega) + i \cdot k(\omega) \tag{2.59}$$

Based on (2.59) and (2.45) we get:

$$\varepsilon_{REAL} = n(\omega)^2 - k(\omega)^2 \tag{2.60}$$

$$\varepsilon_{IMAG} = 2 \cdot n(\omega) \cdot k(\omega) \tag{2.61}$$

In these formulas $k(\omega)$ is the extinction coefficient. It directly influences the absorption of optical EM waves, which propagate through the medium. It is important to mention Beers law (or Beer–Lambert law). This law relates the exponential attenuation of EM waves to the dielectric properties of the material through which the light is passing. If we introduce beam intensity $I(x)$, we can express this law through the following formula:

$$I(x) = I_0 \cdot e^{-\alpha_{coef} \cdot x} \tag{2.62}$$

In this formula α_{coef} is the attenuation coefficient. As we know:

$$|E| \sim e^{i \cdot \frac{\omega}{c} \cdot (n(\omega) + i \cdot k(\omega)) \cdot x} \tag{2.63}$$

Since beam intensity is directly related to the square of electric field intensity, we can write:

$$|I| \sim e^{2\varepsilon \cdot i \cdot \frac{\omega}{c} \cdot (n(\omega) + i \cdot k(\omega)) \cdot x} \tag{2.64}$$

From (2.62) and (2.64) we can define attenuation:

$$\alpha_{coef} = 2 \cdot \varepsilon \cdot i \cdot \frac{\omega}{c} \cdot (n(\omega) + i \cdot k(\omega) \tag{2.65}$$

2.3 Classical antennas

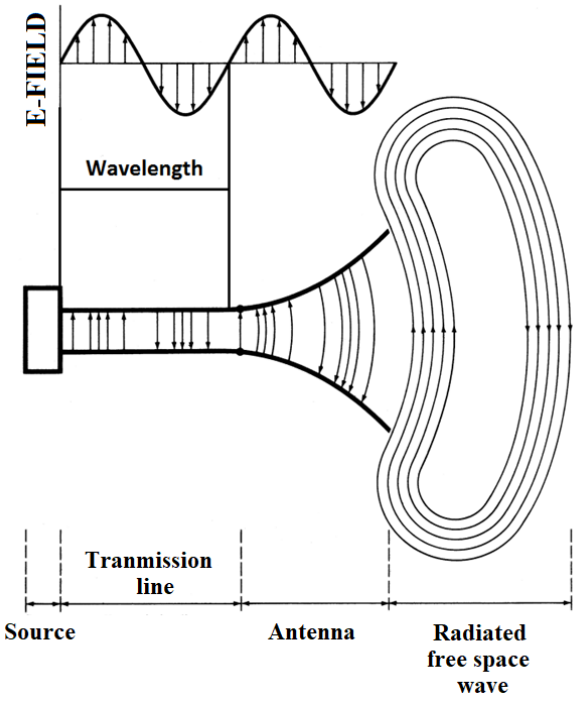

Figure 2.2: Antenna as a transition device, picture taken from [54]

Antennas are components for sending and/or receiving electromagnetic waves and acting as a converter between bound and freely propagating electromagnetic energy. Three important scientists in antenna theory are Guglielmo Marconi, Heinrich Hertz, and Nikola Tesla. Marconi developed a wireless telegraph system based on radio waves. Heinrich Hertz proved the existence of electromagnetic waves, which are theorized and analyzed by Maxwell [53, 54, 55]. Finally, Nikola Tesla, a Serbian-American inventor, provided new solutions for wireless transmission.

When we analyze the antenna definition and Figure 2.2, the transmission line is the guiding device, the free space is the area where radiation comes out, and the antenna cross-section is, in this case, the device with a pyramidal shape (horn antenna). From the engineering practice point of view, the transmission line can be a waveguide (rectangular, cylindrical, or elliptical) or a coaxial cable.

2.4 Hertzian Dipole

The Hertzian dipole is a simple radiating element. The other name used is the infinitesimal dipole. It can be represented as two-point charges separated by some infinitesimal distance or as a conductor (wire) with an infinitesimal length through which current flows, as shown in Figure 2.3.

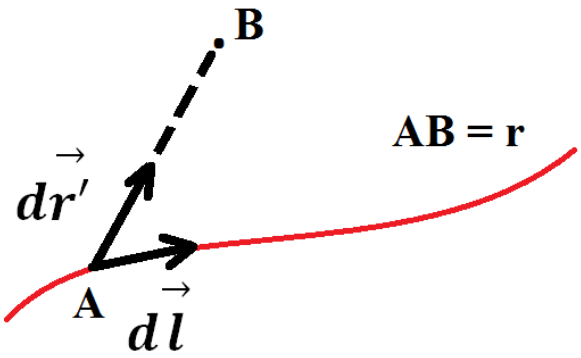

Figure 2.3: Ideal Hertzian dipole (Biot-Savart law illustration)

That current is uniformly distributed along the length. Regardless of the antenna type, its distance or length is significantly less than the wavelength. While this depiction may not be entirely realistic, it effectively illustrates typical linear antennas, which can be segmented into many infinitesimally small sections exhibiting uniform current distribution. By positioning this dipole at the center of the spherical coordinate system, we can define the magnetic field at a

specific point at a certain distance from the dipole. The Biot–Savart law is then applied to determine the magnetic field at point B, generated by the current I flowing through various conductors or wires.

$$d\vec{H}(\vec{r},t) = \frac{\vec{I}(\vec{r}',t)}{4\cdot\pi}\cdot\frac{d\vec{l}\cdot(\vec{r}-\vec{r}')}{|\vec{r}-\vec{r}'|^{3}} \tag{2.66}$$

When connecting two wires to the voltage source, as shown in Figure 2.4, this system does not radiate. At the end of the two wires, we would have a termination, which causes a standing wave. However, because of the voltage source's polarity, the wires' currents would be out-of-phase. That results in destructive interference in the far-field. But if we bend the ends of wires in opposite directions, like in Figure 2.5, we get a dipole antenna. This structure radiates very efficiently because currents in bent antenna arms oscillate in phase. If we establish a z-axis in the direction of the wires and if we presume that the wires are very thin, the formula for current distribution is:

$$I(z) = I_0\cdot\sin\left(\mathrm{k}\cdot\left(\frac{L}{2}-|z|\right)\right) \tag{2.67}$$

If we observe gap where $z = 0$, then equation becomes:

$$I(z) = I_0\cdot\sin\left(\mathrm{k}\cdot\frac{L}{2}\right) \tag{2.68}$$

This is a very good approximation, but it is challenging to compare radiated powers between antennas with different lengths because we are not able to define the correct value I_0.

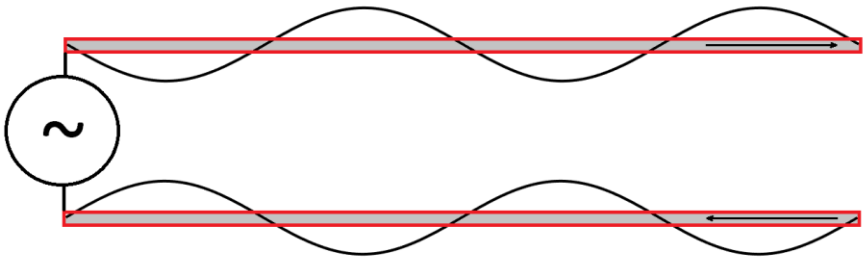

Figure 2.4: Current distribution over transmission line which has no dipole

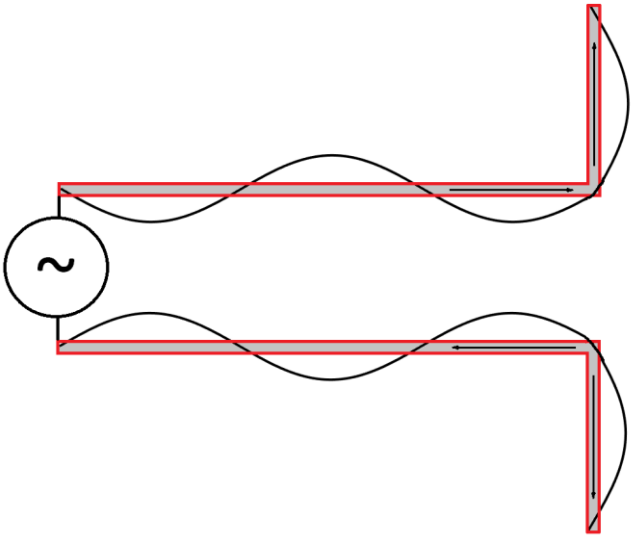

Figure 2.5: Current distribution over the transmission line, which has a dipole

2.5 Antenna classification and characteristics

Before we start investigating nanoantennas, it is necessary to review antenna basics. Of course, we will refer to widely recognized references [53-55]. An antenna is a component that can receive and/or transmit electromagnetic radiation. Its primary function is to couple the freely propagating radiation with strongly localized near fields. Standard antennas operate in the frequency band between 10 kHz and several hundred GHz.

2.5.1 Antenna classification

The fundamental classification of all antennas is based on their angular radiation pattern – omnidirectional and directional antennas.

1A. Omnidirectional antennas are antennas that radiate or receive waves in all directions. Thus, they are usually used in broadcast systems. Well-known omnidirectional antennas include vertically oriented dipole antennas, ground plane antennas, and horizontal loop antennas, as shown in Figure 2.6.

Dipole antenna Loop antenna Monopole ground-plane antenna

Figure 2.6: Omnidirectional antennas

1B. Directional antennas are designed to transmit or receive waves in a particular direction. They offered better directivity and greater gain than other antennas. Examples include horn antennas (conical or pyramidal) and reflector antennas, as shown in Figure 2.7.

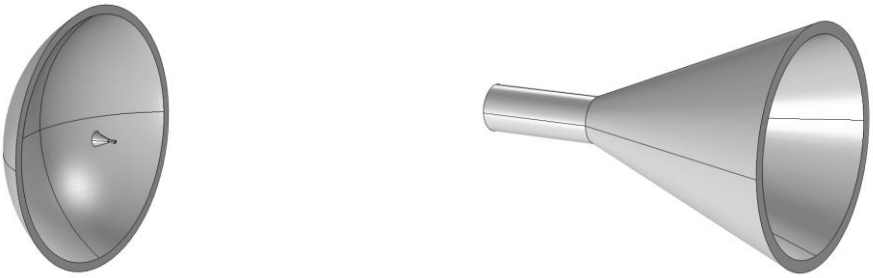

Reflector antenna (horn antenna is feeding). Horn antenna

Figure 2.7: Directional antennas

Other classifications could be done by their spectral radiation pattern.

2A. Resonant antennas (Figure 2.8) are designed to operate over a narrow band of frequencies. Within this limited bandwidth, they demonstrate very good performance in terms of gain and radiation efficiency, but on the other hand, they have low power. One common challenge is creating impedance-matching circuits for such antennas, which can be quite tricky.

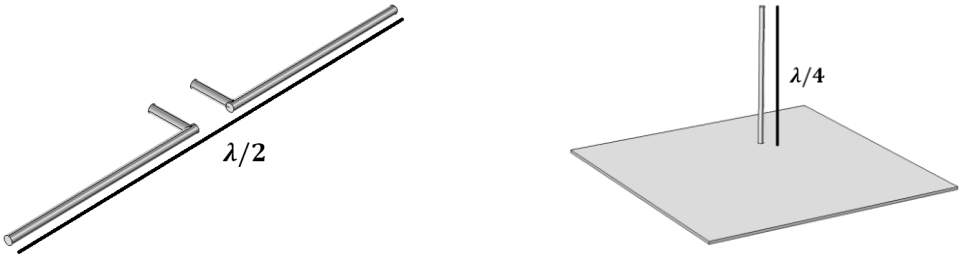

Dipole resonant antenna Monopole ground-plane resonant antenna

Figure 2.8: Resonant antennas

2B. Non-resonant or broadband antennas (Figure 2.9) are antennas which operate over the broadband of frequencies.

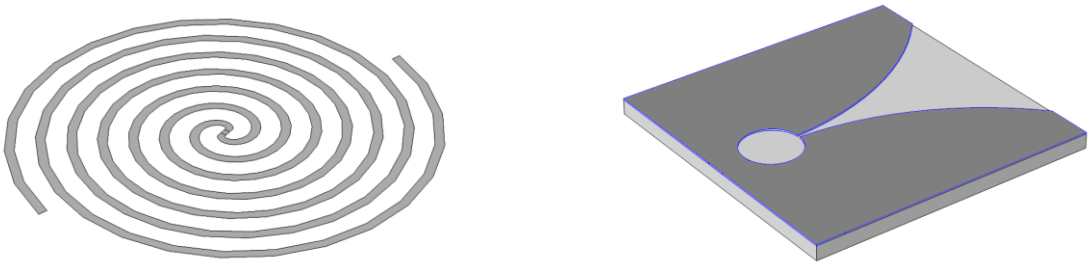

Spiral antenna Vivaldi antenna

Figure 2.9: Broadband antennas

When we analyze all antenna performances, we see no perfect antenna. Thus, antennas must be optimized for certain applications. For instance, broadband antennas are very convenient for covering a wide range of frequencies, but they often have low efficiency. Furthermore, following other literature, antennas can be classified differently. [55]:

• small electrical antennas

• resonant antennas

• broadband antennas

• aperture radiators

This thesis considers resonant antennas (dipole, L-shaped, cross-shaped) and aperture radiators or slot antennas (also with different shapes). For antenna analysis, we need to make certain assumptions.

• Antennas are made from metal, which is a perfect electrical conductor ($\sigma = 0$).

• The penetration depth is negligibly small compared to the conductor diameter. Therefore, we can analyze fields through surface currents.

Regarding directional behavior, it does not matter whether the antenna is used as a transmitting or receiving antenna since the reciprocity principle applies [56].

The Poynting vector is a critical parameter for energy flow description. If we know the electric field and magnetic field vectors, we can calculate the direction of energy flow and its amount. The vector is:

$$\vec{S} = \vec{E} \times \vec{H}^* \tag{2.69}$$

If we analyze time harmonic signals, then the equation is:

$$\vec{S} = \frac{1}{2}(\vec{E} \times \vec{H}^*) \tag{2.70}$$

As we might see, this is a complex number. If we perform time averaging, the imaginary part no longer exists. In that case, the equation is:

$$\vec{S}_{TIME\_AVERAGED} = \frac{1}{2} Re(\vec{E} \times \vec{H}^*) \tag{2.71}$$

2.5.2 Near- and far-field characteristics of antennas

To conduct a thorough antenna analysis, we need to examine near-field and far-field regions. Of course, where the near field ends and the far field begins always depends on wavelength. Most definitions define a transition area between the near and far field. Commonly accepted is the definition for very small Hertzian dipoles, while larger antennas with dimensions greater than $\lambda/2$. can have different criteria. , Overall, we can identify three main regions that surround the antenna:

(a) reactive near-field region,

(b) radiating near-field (Fresnel) region or transition region

(c) far-field (Fraunhofer) region.

There is no strict boundary between their regions, but specific differences exist.

(a) The reactive near field region is the part of the near field region immediately close to the antenna in which fields are reactive or E and H fields are orthogonal and out of phase. These fields must be in phase if we want to observe the existence of propagating and not reactive fields. The outer boundary of this region is at distance *R.*

$$R = 0.62 \cdot \sqrt{\frac{D^3}{\lambda}} \tag{2.72}$$

D here is the largest dimension of the antenna. This equation is valid for most antennas. For very short dipoles or equivalent radiators, it is:

$$R = \frac{\lambda}{2 \cdot \pi} \tag{2.73}$$

(b) Radiating near-field region (or Fresnel region) is the region between the reactive near-field region and the far-field region. In the Fresnel region, radiation fields dominate, and the angular field distribution directly relates to distance from the antenna.

$$0.62 \cdot \sqrt{\frac{D^3}{\lambda}} < R < 2 \cdot \frac{D^2}{\lambda} \tag{2.74}$$

The formula shows that if the maximum dimension is not large enough compared to the wavelength, the Fresnel region will not appear. In any case, we can simplify and say that the near field is the region close to the nanoantenna where the fields are strongly bound to the nanoantenna. In this area, the difference between fields can be huge, but we can say that the fields drop proportionally by $\frac{1}{r^3}$ with distance.

(c) In the far field or so-called Fraunhofer region, only propagating waves exist since the fields are no longer strongly bound to the antenna. In the far-field fields, do not drop by $\frac{1}{r^3}$ but by $\frac{1}{r}$. Due to the far field's higher "stability," we can measure it. On the other hand, for the near field, we primarily use simulations. If we perform analysis in air and do not need angular properties, we can calculate the far field from the near field distribution using the Straton-Chu formula [57].

2.5.3 Characteristic values of antenna

2.5.3.1 Radiation pattern

Since the antenna does not radiate isotropically but is angle-dependent, we can say that the antenna radiation pattern is a function that relates the antenna's radiation properties to space coordinates [54]. Thus, antenna analysis in the polar coordinate system is very important, as in Figure 2.10.

If we perform a 3D analysis, the radiation pattern will represent the radiation property along the surface at a constant radius from the observer's perspective. Along that surface (which is a function of the angular space), we can calculate the field (amplitude field pattern) and power density (amplitude power pattern).

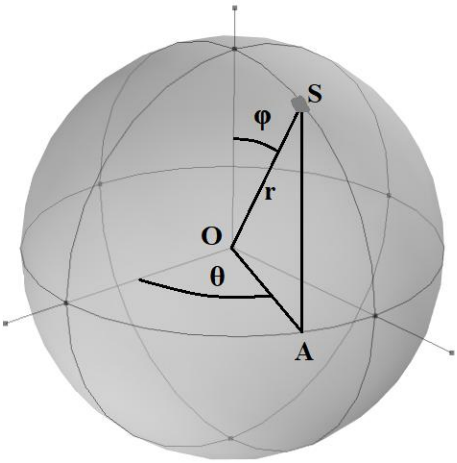

Figure 2.10: Radiation pattern in the spherical coordinate system

Amplitude power pattern is directly related to the square of the field. The average radiated power produced by the antenna would be the integration of a time-averaged Poynting vector over the surface:

$$P_S = \frac{1}{2} \cdot \oiint_{Surface} Re(\vec{E} \times \vec{H}^*) \cdot d\vec{S} \tag{2.75}$$

In RF engineering, the performance of antennas is typically expressed in terms of gain and power patterns. For analyzing antennas, we often use an isotropic source as a reference for comparison with a real antenna—an ideal source that radiates the same way in all directions. Isotropic radiation means that the Poynting vector no longer depends on angles θ and φ. The only relevant component is the radial component r because power will be uniformly distributed over the sphere of radius r. Therefore, the radiated power can be calculated as:

$$P_S = \frac{1}{2} \cdot \oiint_{Surface} \vec{P}_{DENSITY} \cdot d\vec{S} = \frac{1}{2} \cdot \int_{\phi=0}^{2\cdot\pi} \int_{\theta=0}^{\pi} P_{DENSITY}(r) \cdot \sin(\theta) \cdot d\theta \cdot d\phi \tag{2.76}$$

$\vec{P}_{DENSITY}$ is power density. After integration, we get:

$$P_S = 4 \cdot \pi \cdot r^2 \cdot P_{DENSITY}(r) \tag{2.77}$$

$$P_{DENSITY}(r) = \frac{P_S}{4 \cdot \pi \cdot r^2} \tag{2.78}$$

2.5.3.2 Radiation intensity

This term is beneficial because it is a typical far-field parameter. The radiation intensity is the power radiated from an antenna per unit solid angle. A full solid angle is $4 \cdot \pi$..Therefore, if we speak about radiation isotropic sources, we can use this formula for radiation density:

$$P_{rad\_isotropic} = \frac{P_S}{4 \cdot \pi} \tag{2.79}$$

Another way to calculate the radiation intensity of the isotropic source is as follows:

$$P_{rad\_isotropic} = P_{DENSITY}(r) \cdot r^2 \tag{2.80}$$

At the same time, if we want to calculate radiation intensity in a certain direction, the formula is:

$$P_{rad} = P_{rad\_isotropic} \cdot D \tag{2.81}$$

where D is directivity.

2.5.3.3 Antenna efficiency

The radiation efficiency of nanoantennas is the key parameter for energy harvesting. Total antenna efficiency describes the antenna's ability to convert incident EM waves into useful energy, which we can further use for different applications [58]. In this context, we are focusing on total antenna efficiency, and radiation efficiency is one of its two components. Radiation efficiency measures the antenna's ability to "capture" the incident wave and bring it to its terminals. The other component is the rectifier's efficiency in converting the "captured" wave into low-frequency power. Here, we investigate only the first component of total efficiency – radiation efficiency. Electromagnetic theory is sufficient for this investigation because some quantum effects at this nanoparticle size still do not need to be considered. The radiation efficiency of antennas is defined as:

$$\eta_{RADIATION\_EFF} = \frac{P_{RADIATION}}{P_{RADIATION} + P_{LOSS}} \tag{2.82}$$

$P_{RADIATION}$ is radiated power and $P_{RADIATION} + P_{LOSS}$ is overall power that is entered at the terminals. P_{LOSS} describes dissipation in the material. These values we can get from 3D FEM simulations in COMSOL Multiphysics. This physical value we can use for the calculation of total efficiency:

$$\eta_{TOTAL\_EFF} = \frac{\int_0^\infty P(\lambda,T)\cdot \eta_{RADIATION\_EFF}\,(\lambda)\cdot d\lambda}{\int_0^\infty P(\lambda,T)} \tag{2.83}$$

Here $P(\lambda,T)$ represents Planck's law for black body radiation:

$$P(\lambda,T) = \frac{2\cdot\pi\cdot h\cdot c^2}{\lambda^5}\cdot\frac{1}{e^{\frac{h\cdot c}{\lambda\cdot k\cdot T}}-1} \tag{2.84}$$

T – temperature of the black body (or Sun surface if we speak about solar energy harvesting).

h – Planck's constant - $6.626\cdot 10^{-34} J\cdot s$

c – speed of light in vacuum - $3\cdot 10^8\ m/s$

k - Boltzmann constant - $1.38\cdot 10^{-23}\ J/K$

2.5.3.4 Gain

The antenna's gain is a key parameter that combines efficiency and directivity. This concept is important because antennas radiate significantly more power in one direction than an isotropic antenna. Gain is defined as the ratio between the antenna's radiation intensity in a specific direction and the radiation intensity that would be obtained from the antenna, which radiates in all directions (isotropically). We calculate gain as:

$$G(\theta,\phi) = D\cdot\frac{P_S(\theta,\phi)}{P_{input}} \tag{2.85}$$

where P_{input} is input power and $P_S(\theta,\phi)$ is the full radiated power calculated by integrating the Poynting vector from equation 2.75.

2.5.3.5 Antenna impedance and impedance matching

The schematic for analysis is in Figure 2.11. V_{TL} is the voltage on the antenna with an impedance $Z_{ANTENNA}$ produced by the incident wave. Input impedance ($Z_{ANTENNA}$) of the antenna is the impedance on the antenna's terminals. Like in all other cases, this impedance has real and imaginary parts. The imaginary part of impedance ($X_{ANTENNA}$) is reactance, and the real part is the sum of radiation resistance and loss resistance. For optimal power transfer to the antenna's terminals, it is essential to cancel out the reactance, ensuring perfect impedance

matching. Therefore, the impedance of the source and the impedance of the antenna need to have complex conjugated values ($Z_{LOAD}{}' = Z_{ANTENNA}{}^{*}$).

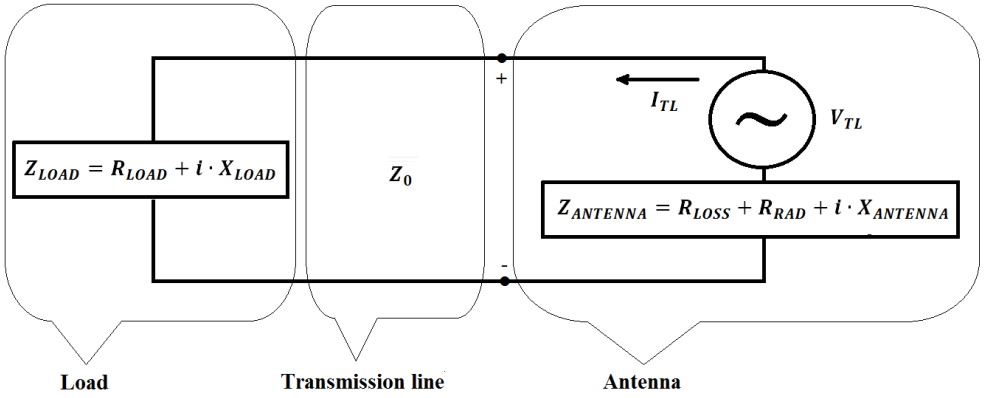

Figure 2.11: Circuit schematics of a load-coupled antenna illuminated by an incident wave.

Actually, Z_{LOAD} is transformed by the transmission line and at terminals + and – is now $Z_{LOAD}{}'$. In RF/Microwave technology, impedance matching is a crucial and straightforward method for designing a network that can transfer energy without significant losses and high reflections. In the microwave frequency range, it is often difficult to measure voltages or currents. For this purpose, we always need a pair of terminals. Very typical examples are RF cables and microstrip lines. If we observe one terminal or conductor as + and the second as -, we can use a simple equation for voltage calculation:

$$V = \int_{+}^{-} \vec{E} \cdot d\vec{l} \tag{2.86}$$

The transverse field between these two terminals has an electrostatic nature. Consequently, no matter what the integration path between the + and – terminals looks like, the result is always the same. On the other hand, around every terminal or conductor, we have magnetic field lines, and based on Ampere's law, we get:

$$I = \oint_{C+} \vec{H} \cdot d\vec{l} \tag{2.87}$$

This formula indicates that the integration contour is any closed path around conductor +. Finally, the characteristic impedance is:

$$Z = \frac{V}{I} \tag{2.88}$$

In the 19th century, Oliver Heaviside first used the term impedance to describe the complex voltage/current in AC circuits, which have active units such as resistors and reactive units such as inductors and capacitors. Later, it was applied to different transmission lines in various forms, such as lumped-element, series impedance, or shunt admittance. In the 1930s, S. A. Schelkunoff extended this concept to EM waves by S. A. Schelkunoff [59].

RF designers, through circuit analysis, always need to define a network that matches arbitrary load impedance. Antennas can be presented as discrete circuit components. Of course, the type of circuit depends on the antenna characteristics. Like in RF engineering, metallic nanostructures have their own optical impedance [60], and optical antenna nanostructures should deliver some portion of EM energy to loads or enhance radiation from themselves [61]. Unfortunately, some basic RF principles can be used but not fully applied in the optical regime. In the optical regime, we do not have available discrete resistors, capacitors, and inductors, and even more importantly, in the optical regime, we have the abovementioned intrinsic resonances (quantum state excitations) and extrinsic resonances (SPRs). Nevertheless, there are published papers on impedance matching in the THz regime. There has been an investigation of impedance matching with plasmonic antennas [62, 63, 64, 65, 66, 67], plasmonic thin films [68], metamaterials [69, 70], and photonic crystals [71]. Impedance matching in the THz regime is in some cases very useful [72, 73]. We need to establish an impedance match on the quantum level to provide good antenna-load matching. That could be some vibrational or spin excitation.

One way to analyze the impedance nature of the antenna is by using a coupled dipole antenna, but with the gap loaded with dielectric/dielectric (Figures 2.12 and 2.13). Based on the load type, we can represent such a structure with a simple circuit. We can observe these structures as capacitors where the electrodes or terminals are gold metallic rods, and the loaded gap is the dielectric between those electrodes.

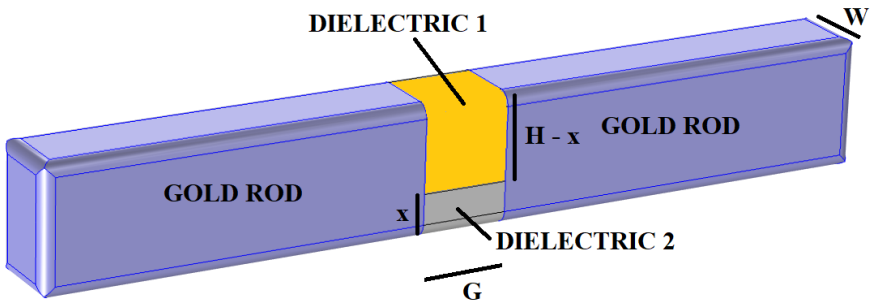

Figure 2.12: Optically coupled antenna loaded with in-parallel dielectric loads

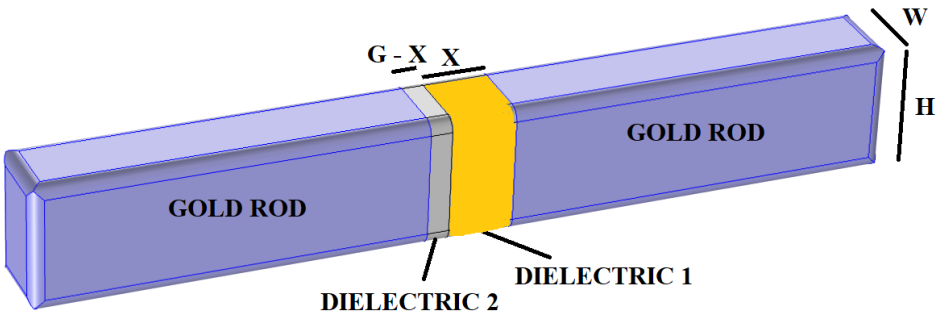

Figure 2.13: Optically coupled antenna loaded with in-series dielectric loads

As we know from basic electrostatics, the capacity of a capacitor is:

$$C = \varepsilon_0 \cdot \varepsilon_r \cdot \frac{S}{G} \tag{2.89}$$

Here, S is the surface of the cross-section (here is approximately $S = W \cdot H$) and G is the distance between rods or the gap length.

If we observe dielectrics in the gap here, the structure from Figure 2.12 corresponds to the parallel connection of capacitors. C_1 is the capacity of a capacitor with dielectric 1, and C_2 is the capacity of a capacitor with dielectric 2.

$$C_{1\_parallel} = \varepsilon_0 \cdot \varepsilon_{r1} \cdot \frac{W \cdot (H - x)}{G} \tag{2.90}$$

$$C_{2\_parallel} = \varepsilon_0 \cdot \varepsilon_{r1} \cdot \frac{W \cdot x}{G} \tag{2.91}$$

The structure from Figure 2.13 corresponds to the series connection of capacitors. C_1 is the capacity of a capacitor with dielectric 1, and C_2 is the capacity of a capacitor with dielectric 2.

$$C_{1\_series} = \varepsilon_0 \cdot \varepsilon_{r1} \cdot \frac{W}{x} \tag{2.92}$$

$$C_{2\_series} = \varepsilon_0 \cdot \varepsilon_{r1} \cdot \frac{W}{G - x} \tag{2.93}$$

Basic circuit theory says that these cases correspond to specific circuit diagrams. Also, all these capacitances are used for impedance calculations. The impedance of a capacitor can be calculated as:

$$X_C = \frac{1}{j \cdot \omega \cdot C} \tag{2.94}$$

The input impedance of a gap-loaded antenna can be calculated using these circuit models, as in Figures 2.14 and 2.15.

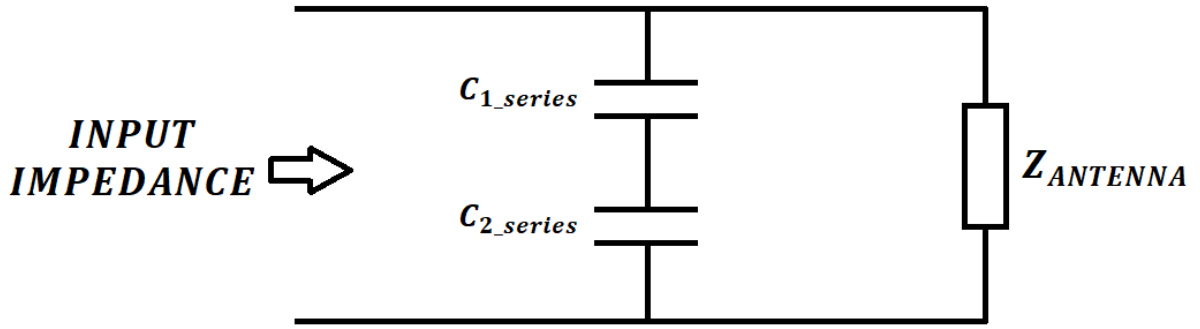

Figure 2.14: Circuit diagram of optically coupled antenna loaded with in-series dielectric loads

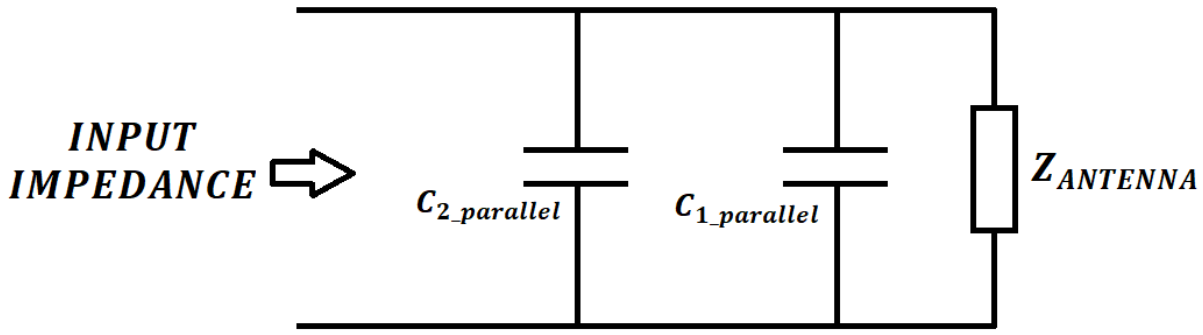

Figure 2.15: Circuit diagram of optical coupled antenna loaded with in-parallel dielectric loads

2.5.3.6 Quality factor

Quality factor describes the quality of the antenna as a resonator. Formula is:

$$Q = \frac{2 \cdot \pi \cdot f_{res} \cdot P_{stored}}{P_{rad} + P_{abs}} \tag{2.95}$$

f_{res} is the resonant frequency, P_{stored} is stored power near the field of the antenna, P_{rad} is radiated power and P_{abs} is absorbed power of the antenna.

2.5.4 Some special characteristics of nanoantennas

While we can learn a lot about nanoantennas from classical antenna theory, there are some main differences to consider. One major difference is that in the optical regime, metals cannot be treated as perfectly thin conductors as they can in RF technology. This is because the electrons in a metal are no longer able to respond to the frequency of incident EM waves. As a result, surface electrons cannot shield incident EM waves perfectly anymore. Now, EM waves can penetrate through the metal and cause some losses, thus heating. Consequently, in optical and IR regimes, we analyze displacement currents and not usual conduction currents [74]. When we investigate the skin effect, we can observe that the penetration depth of metals at optical frequencies is the same order of magnitude as antenna structure size.

2.5.4.1 Skin depth

Skin depth (δ) describes how far the field can penetrate the material. More correctly, it is the depth at which the intensity of the incident wave dropped to 1/e of its initial value. Formula is:

$$\delta = \frac{\lambda}{2 \cdot \pi \cdot k} \tag{2.96}$$

k should not be mixed with wave numbers. k is here an imaginary part of the refractive index. The formula for the dielectric function can be calculated:

$$k = \sqrt{\frac{\sqrt{{\varepsilon_{REAL}}^2 + {\varepsilon_{IMAG}}^2} - \varepsilon_{REAL}}{2}} \tag{2.97}$$

If we speak about gold and silver, there is a new dielectric function value for every wavelength and, therefore, skin depth.

2.5.4.2 Diffraction limit

EM waves cannot be easily used as information carriers in integrated circuits due to the limited potential for integrating components at a small scale. Here, a topic called diffraction limit becomes very relevant. By following the literature, it can be said that light cannot be localized within the dielectric material area much smaller than the wavelength of the EM wave in the material. This is the so-called diffraction limit [10, 11].

The interesting behavior of optical and near-IR nanoantennas is that they operate beyond the diffraction limit. As we will see, one typical rod-coupled gold nanoantenna with a gap size of

20 nm and a rod length of 100nm has a resonant field enhancement at around 804nm. This "bellow diffraction limit" behavior of nanoantennas has been explored in various studies [2, 3, 4, 15, 74, 75].

When a plane wave propagates in the direction of the wave vector $\vec{k}$ and the polarization direction is along the longitudinal rod axis; we will have standing waves that are perpendicular to the direction of propagation of incident light. Consequently, the standing wave will be parallel to the electric field $\vec{E}$.

2.5.4.3 Lightning rod effect

The lightning rod effect is essential in designing and fabricating plasmonic nanoparticles [15, 74]. Surface charges are concentrated at the sharper tips of metallic nanostructures. Due to surface plasmon excitation, an increase in the field occurs. It is important to note that this is not a field caused by the resonant effect.

2.6 Propagating surface plasmons

Surface plasmon polaritons (SPP) are enhanced electromagnetic waves that are highly confined at the interface between a metal and a dielectric. SPPs are excited when the incoming EM field is coupled to the coherent oscillations of the free electrons in the metal, which match the frequency of the incoming EM field. Surface plasmons are perpendicular to the metal surface and exhibit strong exponential decay of the field in both directions. This results in the majority of their energy being concentrated near the interface, where the field intensity is the highest. Surface plasmons can propagate along metal surfaces even several micrometers [1, 76]. However, some conditions need to be fulfilled to even have surface plasmons at the metal-dielectric interface.

If we establish boundary conditions like in Figure 2.16 with an infinitely xy plane, it has already been proven that, in this case, there is no transverse-electric (TE) mode. Only transverse-magnetic (TM) mode with components E_x, E_z, and H_y can exist [1]. It is worth mentioning that SPPs in Figure 2.16 exhibit both EM wave and surface charge behaviors. The generation of surface charges is caused by an electric field normal to the interface or surface (E_z). The electric field, parallel to the interface (E_x), passes through both media and decays exponentially with decay length δ_m in metal and decay length δ_d in dielectric.

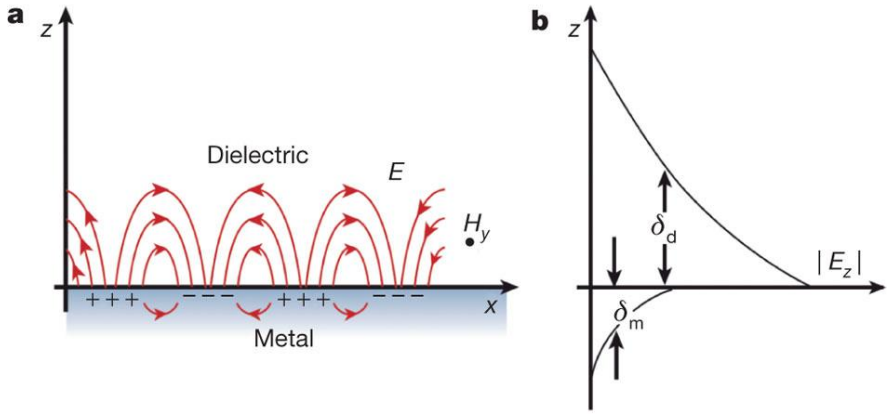

Figure 2.16: SPPs representation, picture taken from [76]

Now we use Helmholtz equations (2.21) and (2.22) with some new conditions taken from Figure 2.16. If we assume homogeneity in the y direction, it will be $\frac{\partial}{\partial y} = 0$ we will express the electric field in the frequency domain as:

$$\vec{E}(\vec{r}) = \vec{E}(x,z) \cdot e^{i(k_x \cdot x + k_z \cdot z)} \tag{2.98}$$

In wave equations (2.21) and (2.22) there was a term k which is a wave vector with initially three components. Parameter k_x is the propagation constant of a traveling wave or component of the wave vector in the direction of propagation and, in most cases, is termed as β. Parameter k_z is or component of the wave vector in z. From wave equation (2.21) and $\nabla^2 = \frac{\partial^2}{\partial x^2} + \frac{\partial^2}{\partial y^2} + \frac{\partial^2}{\partial z^2}$ we get:

$$\frac{\partial^2 \vec{E}(\vec{r})}{\partial x^2} + \frac{\partial^2 \vec{E}(\vec{r})}{\partial z^2} + k^2 \cdot \vec{E}(\vec{r}) = -k_x{}^2 \cdot \vec{E}(\vec{r}) - k_z{}^2 \cdot \vec{E}(\vec{r}) + k_0{}^2 \cdot \varepsilon_r{}^2 \cdot \vec{E}(\vec{r}) = 0 \tag{2.99}$$

This equation can be applied to both the metal and dielectric sides of the interface, ensuring a comprehensive understanding of the behavior of surface plasmons in different materials.

$$k_{x\_dielectric}{}^2 + k_{z\_dielectric}{}^2 = \varepsilon_{dielectric}{}^2 \cdot k_0{}^2 \tag{2.100}$$

$$k_{x\_metal}{}^2 + k_{z\_metal}{}^2 = \varepsilon_{metal}{}^2 \cdot k_0{}^2 \tag{2.101}$$

Electric field and wave vector have the same components in the x direction, so here applies:

$$E_{x\_metal} = E_{x\_dielectric} = E_x \tag{2.102}$$

$$k_{x\_metal} = k_{x\_dielectric} = k_x = k_{SPP} \tag{2.103}$$

If we apply boundary conditions on the metal-dielectric interface, we get:

$$\varepsilon_{metal} \cdot E_{z\_metal} = \varepsilon_{dielectric} \cdot E_{z\_dielectric} \tag{2.104}$$

$$k_{SPP} \cdot E_x + k_{z\_metal} \cdot E_{z\_metal} = 0 \tag{2.105}$$

$$k_{SPP} \cdot E_x + k_{z\_dielectric} \cdot E_{z\_dielectric} = 0 \tag{2.106}$$

From (2.105) and (2.106), we obtain the ratio:

$$\frac{k_{z\_dielectric}}{k_{z\_metal}} = \frac{E_{z\_metal}}{E_{z\_dielectric}} \tag{2.107}$$

If we insert ratio (2.107) into (2.104) we have the most important ratio:

$$\frac{k_{z\_dielectric}}{k_{z\_metal}} = \frac{\varepsilon_{dielectric}}{\varepsilon_{metal}} \tag{2.108}$$

Based on equations (2.108), (2.100), and (2.101) finally, we can get the dispersion relation:

$$k_{SPP} = k_0 \cdot \sqrt{\frac{\varepsilon_{metal} \cdot \varepsilon_{dielectric}}{\varepsilon_{metal} + \varepsilon_{dielectric}}} \tag{2.109}$$

This equation is a dispersion relation for the wave number of surface plasmons (or the propagation constant of surface plasmon polaritons). The other (z) component is different in dielectric and metal areas.

$$k_{z\_dielectric} = k_0 \cdot \sqrt{\frac{\varepsilon_{dielectric}^{\ 2}}{\varepsilon_{metall} + \varepsilon_{dielectric}}} \tag{2.110}$$

$$k_{z\_metal} = k_0 \cdot \sqrt{\frac{\varepsilon_{metal}^{\ 2}}{\varepsilon_{metall} + \varepsilon_{dielectric}}} \tag{2.111}$$

To provide the existence of a surface wave that propagates in the x direction, we need the real value of k_{SPP} and imaginary value of $k_{z\_dielectric}$ or k_{z_metal}. That means that we need:

$$\varepsilon_{metall} + \varepsilon_{dielectric} < 0 \tag{2.112}$$

$$\varepsilon_{metall} \cdot \varepsilon_{dielectric} < 0 \tag{2.113}$$

We can say that there are two modes of surface plasmon waves.

1. When $k_{SPP} > \frac{\omega}{c}$ we have a non-radiative mode
2. When $k_{SPP} < \frac{\omega}{c}$ we have a radiative mode

We can calculate the EM field around the metal-dielectric interface when we know the propagation constant and information about the metal and dielectric. This formula for the propagation constant of SPPs indicates that compared to the light (or photons) surface, plasmon polaritons have shorter wavelengths or higher wave numbers for the same frequency. As it is already well-known, to have surface plasmons, we need a metal and a dielectric with opposite signs. This condition is fulfilled for noble metals in optical and near-IR spectrum. If we check this formula using different examples, we will see that the wave number for surface plasmons is greater than that in free space for the same frequency. The system is in the resonant state when it is fulfilled $\varepsilon_{metal} = -\varepsilon_{dielectric}$. Even if we have different wave vectors, we can stimulate surface plasmon polaritons via evanescent waves using a prism. No matter whether the Otto or Kretchman configuration is used, the idea is the same as stated in Kretchman's work – every roughness of the surface has its own "wave vector," which can cause a change in the wave vector of the surface plasmon by using the evanescent waves. These evanescent waves excite surface plasmons at the interface, along with the wave vector that originates from the glass substrate. With this method, the prism provides the necessary angle at the interface.

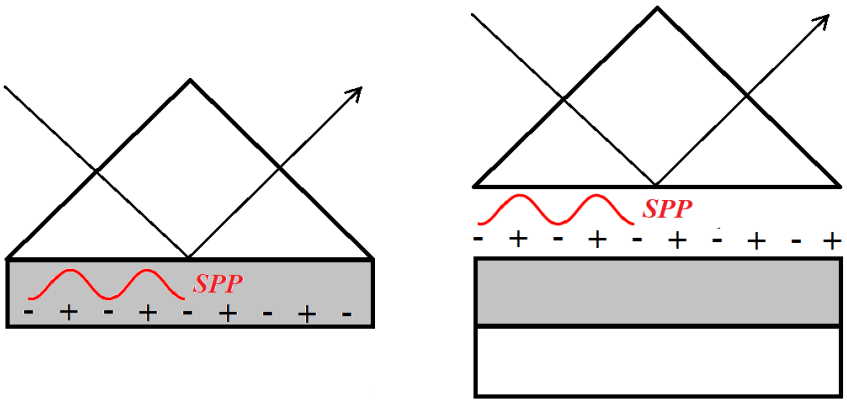

Kretchmann configuration *Otto configuration*

Figure 2.17: Configurations (Kretchmann and Otto) that help in the excitation of propagating SPPs

This approach has two configurations, Kretchmann and Otto, as shown in Figure 2.17. In the Kretchmann configuration, metallic film is applied directly to the prism. In contrast, in the Otto configuration, there is a small gap between the metallic film and the prism [10, 77, 78, 79]. Another option is to utilize periodic Bragg grating (Figure 2.18), which has different modes with wave vectors different from incident light wave vectors [80]. Unfortunately, none of these methods are effective for achieving subwavelength confinement of the light.

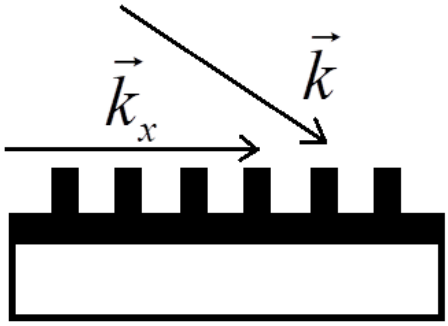

Figure 2.18: Grating configuration for excitation of SPP polaritons

This confinement is the main reason why SPPs are so sensitive to every metallic surface modification, which causes a rise in restoring forces and, therefore, more intensive electron excitement. Figure 2.19 shows a schematic dispersion relation for propagating SPPs.

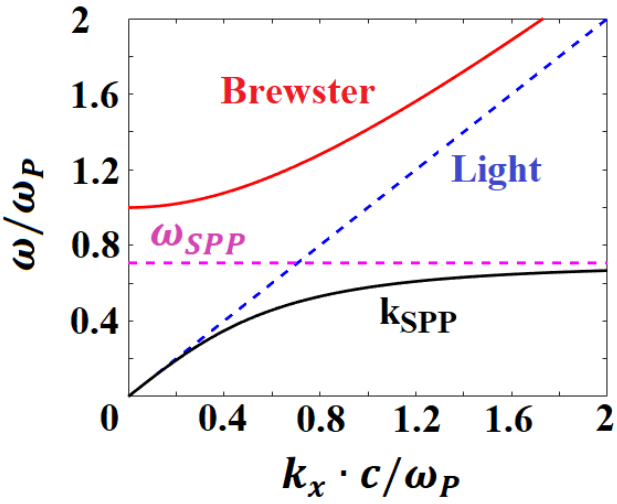

Figure 2.19: Schematic representation of dispersion relation for propagating SPPs. For $\omega < \omega_{SPP}$ we have surface plasmons for $\omega > \omega_{SPP}$ we have the freely propagating Brewster mode, in which the metal corresponds to a dielectric. Blue: vacuum light line.

2.7 Localized surface plasmon resonances (LSPRs)

Unlike SPPs, LSPRs are non-propagating excitations of the conduction electrons in metallic nanoparticles, which are coupled to EM radiation. Every particle consists of molecules. If EM radiation interacts with a particle, the electron orbits within its molecules periodically oscillate with the same frequency as the electric field of the incident radiation, as in Figure 2.20. That oscillation of the electron cloud results in a periodic charge separation within a molecule, called the induced dipole moment. Induced dipole moment acts like a new light source, resulting in scattered light, which is mostly emitted at the same frequency as the incident light. Two previously mentioned theories describe light scattering - Rayleigh scattering (Lord Rayleigh) and Mie scattering (Gustav Mie). Mie scattering theory is more applicable since Rayleigh scattering threats are just small and non-absorbing particles. LSPRs can be excited directly by an incoming electromagnetic field that matches the energy of an oscillation. Therefore, the energy of LSPRs is determined by the type of material (typically noble metals), the nanoparticle's size, shape, and the refractive index of the surrounding environment. Of course, those parameters don't have the same influence on resonant behavior. The abovementioned non-propagating excitations cause huge field enhancement near and inside metal. Metallic NPs with sizes smaller than the wavelength of light show localized surface plasmon resonances (LSPR). This field enhancement is used in surface-enhanced Raman scattering (SERS), [81] solar energy harvesting, and molecule emission [82].

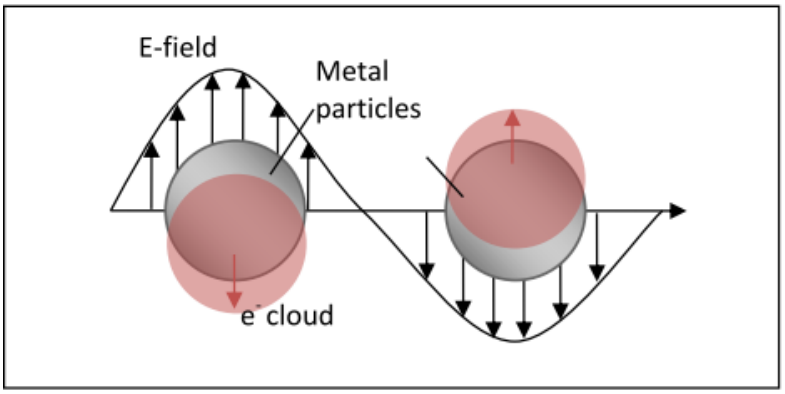

Figure 2.20: Illustration of conduction electron charge displacement cloud relative to the nuclei

Scientists face significant challenges in understanding the resonant behavior of metallic nanoparticles, whether they are talking about SPPs or LSRPs. By using very rough approximation, some standard classical shapes (sphere, ellipsoid) could be solved with quasi-static approximation, where we assumed that the EM field was uniform across the nanoparticle, as we already show But, since this approximation is very rough, we should utilize more advanced techniques for finding these solutions. Some of these methods include the T-matrix method, finite difference time domain (FDTD) method, and finite element method (FEM).

2.8 Material choice

We have previously discussed the influence of the material's dielectric function on resonance behavior. It has been demonstrated that antennas with the same geometry have different resonance peak positions if they are made from various materials. By choosing the proper metal and surrounding medium, we can cover a significant portion of the spectrum [83–86].

3 Numerical simulation methods

3.1 Scattering models

3.1.1 Size Dependence of Plasmon Absorption: Mie's Theory

In 1908, Gustav Mie provided the first explanation of surface plasmon resonances. He solved Maxwell's equations for the absorption and scattering of EM radiation by small spherical nanoparticles [87, 88]. A deeper mathematical discussion is already published [89, 90]. Gustav Mie defined the total extinction coefficient of small metallic particles as a sum of all-electric and magnetic multipole oscillations contributing to the electromagnetic field's absorption and scattering. When analyzing gold nanoparticles that have a size smaller than 25nm, we introduce dipole approximation, which means that only the dipole term contributes to the absorption [91]. Consequently, all absorption spectrum changes are related to the so-called intrinsic size effect [92]. In such a dipole approximation, plasmon absorption does not depend on the particle size. It is experimentally proven that plasmon bandwidth increases with decreasing nanoparticle size. Therefore, we can say that in the intrinsic region (nanoparticle size smaller than 25nm for gold), the nanoparticle's and plasmon bandwidth's radius are inversely proportional [91].

For the gold nanoparticles larger than 25 nm, the extinction coefficient clearly depends on nanoparticle size. The nanoparticle's and plasmon bandwidth's radius in this so-called extrinsic region are directly proportional. In this case, we have an extrinsic size effect where Mie theory applies. When discussing the maximum absorption of surface plasmon resonances, the extrinsic size region is much easier to analyze than the intrinsic size region. In the extrinsic size region, the resonant peak shifts to the lower energy band (or higher wavelength) as nanoparticle size increases. It is also often used the term "red-shift" (in the case of decreasing nanoparticle size, we would have "blue-shift" of the resonant peak). However, in regions of intrinsic size, the situation is more complex. It is experimentally proven [92, 93] that if we decrease the size of the nanoparticle in the intrinsic size region, we can observe both red-shifted and blue-shifted of the resonant peak. Mie's theory is based on the fact that electron orbitals within a molecule can oscillate with the frequency of an incident wave. That oscillation causes the separation of charges and the creation of dipole moments. Induced dipole moment is the new source of light

that scatters the light with mainly the same frequency as the incident light. Scattering can be described by Rayleigh's and Mie's theories. Rayleigh's theory can be applied only to small, non-absorbing particles. On the other hand, Mie's theory can be applied to spheres and ellipsoids [87]. To proceed, we first need to define scattering coefficients, a_i and b_i. Also, some other values should be introduced.

$$m = \frac{n_{metal}}{n_{medium}} \tag{3.1}$$

n_{metal} is the complex refractive index of metal, and n_{medium} is the real refractive index of the medium.

$x = k \cdot r$ where k is the intensity of the wave vector and r is the radius of the nanoparticle.

ψ_i and ξ_i are Riccati-Bessel functions.

$$a_i = \frac{m \cdot \psi_i(m \cdot x) \cdot \psi_i'(x) - \psi_i(x) \cdot \psi_i{}'(m \cdot x)}{m \cdot \psi_i(m \cdot x) \cdot \xi_i'(x) - \xi_i(x) \cdot \psi_i{}'(m \cdot x)} \tag{3.2}$$

$$b_i = \frac{\psi_i(m \cdot x) \cdot \psi_i'(x) - m \cdot \psi_i(x) \cdot \psi_i{}'(m \cdot x)}{\psi_i(m \cdot x) \cdot \xi_i'(x) - m \cdot \xi_i(x) \cdot \psi_i{}'(m \cdot x)} \tag{3.3}$$

As can be seen, these scattering coefficients are zero when m converges to 1. This is expected since, in that case, metal and medium are almost the same materials. Now, scattering and extinction cross-sections can be calculated.

$$Q_{scattering} = \frac{2\pi}{k^2} \cdot \sum_{i=1}^{i=\infty} (2 \cdot i + 1) \cdot (|a_i|^2 + |b_i|^2) \tag{3.4}$$

$$Q_{extinction} = \frac{2\pi}{k^2} \cdot \sum_{i=1}^{i=\infty} (2 \cdot i + 1) \cdot Re(a_i + b_i) \tag{3.5}$$

3.1.2 Scattering of metallic nanostructures - Rayleigh scattering

In this type of scattering, we observe very small nanoparticles that fulfill conditions $\frac{n_{metal}}{n_{medium}} \cdot k \cdot r << 1$ and $k \cdot r << 1$ [87]. By using these values in (3.4) and (3.5) and by solving Riccati-Bessel functions from (2.67) and (2.68), we get:

$$Q_{scattering} \sim \frac{{V_{geom}}^2}{\lambda^4} \tag{3.6}$$

$$Q_{absorption} \sim \frac{V_{geom}}{\lambda} \tag{3.7}$$

Also, we get dependent on essential terms:

$$Q_{scattering} \sim \left|\frac{m^2 - 1}{m^2 + 2}\right|^2 \tag{3.8}$$

$$Q_{absorption} \sim \frac{m^2 - 1}{m^2 + 2} \tag{3.9}$$

Now, it is easy to conclude that we will have bigger scattering on lower wavelengths. Moreover, for smaller particles, absorption dominates in comparison to scattering.

3.1.3 Quasi-static approximation or Rayleigh approximation

This approximation can be applied when the nanoparticle is much smaller than the operating wavelength. In the context of the optical spectrum, this means applying the approximation to nanoparticles that are much smaller than 400 nm. This condition is essential because, for small nanoparticles, it can be assumed that there is no change in the phase of the EM wave. Consequently, the EM wave is homogeneous within the nanoparticle. In quasi-static approximation, polarizability can be defined for spheres and ellipsoids. When an electric field is applied to the material, polarizability describes the tendency of the material to develop an electric dipole moment in response to that applied field. dipole moment corresponding to that applied electric field. As we know, the equation for electrostatic potential is:

$$\vec{E}(r) = -\vec{\nabla}\Phi(r) \tag{3.10}$$

Also, here is an essential Laplace equation:

$$\Delta\Phi = 0 \tag{3.11}$$

This Laplace equation shows that a small sphere in an electrostatic field can be approximated by an ideal dipole [87].

First, by knowing the relation between refractive and dielectric function, we get:

$$\frac{m^2 - 1}{m^2 + 1} = \frac{\varepsilon_{metal}(\omega) - \varepsilon_{medium}}{\varepsilon_{metal}(\omega) + 2 \cdot \varepsilon_{medium}} \tag{3.12}$$

Also, we can define polarizability for the spherical shape of nanoparticle:

$$\alpha_{sphere}(\omega) = 4 \cdot \pi \cdot \varepsilon_0 \cdot r^3 \cdot \frac{\varepsilon_{metal}(\omega) - \varepsilon_{medium}(\omega)}{\varepsilon_{metal}(\omega) + 2 \cdot \varepsilon_{medium}(\omega)} \tag{3.13}$$

This value can be applied to calculating the absorption and scattering of a given nanoparticle. The system is in the resonant state when it is fulfilled:

$$|\varepsilon_{metal}(\omega) + 2 \cdot \varepsilon_{medium}(\omega)| = 0 \tag{3.14}$$

Finally, (3.4) and (3.5) become:

$$Q_{scattering}(\omega) = \frac{k^4}{6 \cdot \pi \cdot \varepsilon_0{}^2} \cdot \left|\alpha_{sphere}(\omega)\right|^2 \tag{3.15}$$

$$Q_{absorption}(\omega) = -\frac{k}{\varepsilon_0} \cdot Imag(\alpha_{sphere}(\omega) \tag{3.16}$$

3.1.3.1 Ellipsoid

In (3.13), we have shown polarizability for spherical nanoparticles, but as we know from geometry, the sphere is only a special case of ellipsoid. Every ellipsoid has three semi-axes, but we will presume that two smaller ones are the same. Thus, we have semi-axes a, $b = a$ and c.The polarizability is now given by:

$$\alpha = V_{geom} \cdot \varepsilon_0 \cdot \frac{\varepsilon_{metal} - \varepsilon_{medium}}{\varepsilon_{medium} + L_{factor} \cdot (\varepsilon_{metal} - \varepsilon_{medium})} \tag{3.17}$$

V_{geom} – volume of ellipsoid nanoparticle

L_{factor} – geometrical factor

$$L_{factor} = \frac{g(e)}{2 \cdot e^2} \cdot \left[\frac{\pi}{2} - \arctan\left(g(e)\right)\right] - \frac{g^{\,2}(e)}{2} \tag{3.18}$$

with $g(e) = \sqrt{\frac{1-e_{factor}{}^2}{e_{factor}{}^2}}$ and $e_{factor} = 1 - \frac{c^2}{a^2}$

3.1.4 Shape-Dependence of Plasmon Absorption – Gans Theory and Discrete Dipole Approximation

Besides size, nanoparticle shape is a relevant factor for SP resonances [94]. This concept can be explained by analyzing 3-D objects where electrons can oscillate with different amplitudes along the three axes of that object (if we speak about anisotropic metallic NPs). Consequently, these different oscillations can lead to the splitting of the plasmon band into two or more bands. This behavior is apparent when we analyze gold nanorods but with bigger widths. In that case, we can see the splitting of plasmon absorption into two bands. The first band (higher energy) corresponds to the oscillation of free electrons perpendicular to the long axis of the rod. The second band (lower energy) corresponds to the oscillation of free electrons along the long axis of the rod [95]. This first band (or transverse mode) has a resonant frequency at around 520 nm, approximately the plasmon band of nanosphere particles. The second band (or longitudinal band) is red-shifted and depends not only on the length of the particles but also on the nanoparticle's aspect ratio (length/width). Gans theory, proposed in 1912, suggests that we can calculate the optical absorption spectrum of randomly oriented gold nanoparticles with a specific aspect ratio by using Mie theory but within the framework of DDA, as real nanoparticles are more similar to cylindrical shape [96].

A common approach for solving the Maxwell equation for anisotropic nanoparticles is discrete dipole approximation (DDA). In this model, the nanoparticle is treated as a finite array of polarizable points at specific locations. Each of the points is the polarizability of a discrete volume. By applying the EM field, dipole moments related to the electric field in that local area are assigned to those points. Since those dipoles interact with each other via an electric field, the other name for this model is coupled dipole approximation. If we observe only one point, a local field that causes certain dipole moments consists of two parts. The first part is an incident field, and the second part is a field caused by radiation from all other dipole moments. Therefore, DDA is an iterative method. Once the dipole moment of all points is solved, we can calculate LSPR (absorption, scattering, and extinction cross-section) for each wavelength [97].

When investigating spherical nanoparticles, we can obtain all three important spectra (extinction, absorption, and scattering) using Mie's theory. In contrast, the discrete dipole approximation, on the other hand, is a very efficient tool for all other shapes. It will be shown that we have only one surface plasmon resonance in a sphere. In cases of other shapes cases, such as rods, cubes, and pyramids, it is possible to observe two or even more peaks. This occurs when we have more distinct symmetries for dipolar resonance [98].

Additionally, an important behavior that might be noticed is that when we compare the ellipsoid and sphere with the same volume, we can see a red-shifted resonant peak of the ellipsoid compared to that of the sphere. If we make the ellipsoid sharper and sharper, the peak shifts more to the red. This phenomenon can be attributed to the surface charges accumulating at the sharp tips of the ellipsoid, which causes an increase in charge separation. Therefore, it reduces the restoring force for electron oscillation; consequently, the resonant peak shifts to a lower energy or higher wavelength. One fascinating behavior can be seen in the case of, for example, a triangular plate. This structure has sharp corners but also possesses a high level of symmetry. As a result, we have peaks shifted to lower energy, but at the same time, there is an intense SPR band. The conclusion is that even though sharp corners increase the abovementioned charge separation, symmetry is the factor that determines such an intense dipole resonance [9]. It is found that the resonance peak also influences the aspect ratio [99, 100]. Therefore, we can summarize the influence of the nanoparticle shape on resonance behavior.

• With increased particle sharpness on corners and its anisotropy, we observe the red-shifting of resonant peaks.

• surface plasmon resonance intensity is higher with an increase in particle symmetry.

• Particle geometry explains how particles can be polarized to reach more resonant peaks.

3.1.5 Effect of interparticle coupling

Significant impact on surface plasmon oscillation involves interparticle electronic coupling. If we set the radius of two spherical gold nanoparticles at R and the distance between particle centers at D, it is proven theoretically and experimentally that if $d \leq 5r$, the electromagnetic coupling becomes evident. As a result, the extinction spectra become more complex, depending

on particle shape, size, and the surrounding medium. The splitting of single NP resonance [101] and the red-shifting of plasmon resonance for even 300 nm [102] were observed.

3.2 Optical properties of the metals - summary

When researchers talk about light-matter interaction, they consider the coupling between the single quantum emitters (fluorescent molecules, quantum dots) and the radiation field mode [12]. These emitters can behave like electric dipoles due to their dimensions, which are very small compared to the wavelength of light. Therefore, the applied field can be considered uniform across the particle [13]. At the nanoscale, the transition between emitters and the radiation field has greatly benefited from plasmonics, exploiting the unique optical properties of metallic nanostructures to confine light at the nanometric regime [14]. One way to enhance the coupling between the emitter and the radiation field mode is by decreasing the mode volume of the confined radiation. Another method is to reduce the effective mode volume (V_{eff}) of the confined radiation using plasmonic nanostructures for light confinement to dimensions well below the diffraction limit [103, 104].

Let's investigate the material properties of some dielectrics. It is important to note that the real part of the dielectric function represents a material's capacity to be polarized, while the imaginary part is related to the material's absorption capability. Therefore, researchers in the microwave industry must choose materials very carefully. The real part of the dielectric function will directly influence the reflection parameter S_{11}. The imaginary part will be strongly related to material heating during the process. Suppose we observe the formula for the imaginary part of the dielectric function; we can see that when $\boldsymbol{\omega}$ is close to $\boldsymbol{\omega_0}$, absorption is at a maximum. At the same time, the real part of the dielectric function decreases. This is known as anomalous dispersion [105]. Macroscopic polarization results from vibrations caused by the penetration of an electromagnetic field through the material. In future analyses, we will consider magnetic permeability as 1 since no magnetization is generated in the optical/IR regime. Plasma oscillation can be explained as a rapid oscillation of electron density in conducting media [1]. In the optical and near-IR spectrum, free electrons in noble metals lead to surface and volume carrier oscillations, known as plasmon polaritons or plasmons. These oscillations have specific resonant frequencies. Therefore, it is crucial to know the frequency-dependent dielectric function of the metal. Gold (Au) and silver (Ag), two metals often used in

plasmonic engineering, will be summarized briefly. Based on the literature, we will show the real and imaginary parts of the dielectric function for both metals [51].

3.3 Perfectly matched layer (PML)

No matter which simulation method we use, handling the edges of the simulation volume is never easy. Most of the techniques that could be applied cause unacceptable reflection. In some simulation methods like FEM or FDTD, the volume we simulate is surrounded by open edge areas, so-called "Perfectly Matched Layers" (PMLs) [106], which were first introduced by Berenger in 1994. PML acts like an open space and absorbs waves as perfectly as possible. This is done anisotropically so that only wave components directed normally to the PML are absorbed. As is well known, with standard computer simulation capabilities, it is only possible to simulate a limited volume. Therefore, PML, which acts like an open space, is very helpful because all unwanted reflections for all frequencies and angles are avoided. PML is based on impedance matching. Of course, real PML does not exist since it can only absorb waves without reflection at some boundary region. Also, it is challenging to define a PML that will be optimized for all arbitrary plane waves with different incident angles, polarizations, and wavelengths. PML consists of several layers that extend the volume surrounding the simulation volume. These layers have increasing absorption so that all fields can decay exponentially. Here is the so-called PML transformation. In already published work, the PML transformation is used to replace the spatial derivatives [107]. With this approach, oscillating waves can be converted into exponentially decaying waves. Two things should be taken care of. First, the perfectly absorbing edge must be far enough from the structure under investigation to avoid near-field influence. Furthermore, the thicker PML increases the probability that all incident power will be absorbed.

3.4 Finite element method (FEM)

The finite element method (FEM) is used for solving partial differential equations (PDEs). By this method, it is possible to define PDEs as superpositions of test functions, which are functions not equal to zero for only certain elements. The test function always "tests" the weak form of the PDE, and it must be sufficiently smooth. By weighting these functions, we can find

a solution. Essentially, by using the FEM in the frequency domain, it is possible to solve Maxwell's equations [108].

The first assumption is that all sources and fields have the same harmonic time dependence. Furthermore, there are no longer derivatives in the frequency domain with respect to time.

The finite element method's simulation body consists of tetrahedra and hexahedra. By tuning the mesh density, we can achieve very high resolution, especially when dealing with irregular structures.

As is already known, Maxwell's equations describe the electromagnetic response in detail. It has already shown how Faraday's and Ampère's laws and their curl equations based on Maxwell's equations can describe wave propagation. The problem appears when we want to use computer simulation to solve Maxwell's equations in some random, non-homogeneous structure. There are several numerical techniques for solving Maxwell's equations, which can be classified in the first step as solutions based on PDE or differential formulations and integral formulations. Furthermore, the solutions can be classified as solutions in the time domain or frequency domain for both formulations. Typical techniques in the integral form are the method of moments (MoM) and the boundary element method (BEM). In PDE form, typical techniques are the finite element method (FEM), the finite difference time domain method (FDTD), and the transmission line matrix method. Two widely used techniques are the finite element method (FEM [109]) and the finite difference time domain method (FDTD [110]). With the FEM, it is possible to solve PDEs. In the first step, the structure is divided into smaller parts, so-called finite elements. This can be done by meshing the geometry, which represents space discretization. Solving all these discrete points means solving the system of algebraic equations. In the FDTD method, the simulation region is also discretized by the mesh, but here, EM fields are calculated in every mesh cell, and the results of those calculations are repeatedly time-stepped. As mentioned, both FEM and FDTD techniques use finite element discretization by meshing to solve continuous equations, which are then discretized for computer calculation. Therefore, if it is assumed that there is a function F and a certain position, then the first derivative could be calculated as:

$$F'(x_0) \approx \frac{F(x_0 + \Delta x) - F(x_0 - \Delta x)}{2\Delta x} \tag{3.19}$$

This approximation represents the difference between functions at points $x_0 + \Delta x$ and $x_0 - \Delta x$. Another way to calculate this is the Taylor-series expansion of $f(x_0 \pm \Delta x)$ around x_0 [110]. The finite element method we always use whenever we need no time-dependent solution or purely harmonic time-dependence in a linear medium so that there is only a single frequency to consider. As mentioned before, the time-harmonic form of Maxwell's equations is used to describe electromagnetic waves. We showed a simplified version of the wave equation, as shown in (2.14) and (2.21) for the electric field and in (2.22) for the magnetic field in the thesis. On the tangential component of $\nabla \times \vec{E}(\vec{r}, t)$ is applied to the PEC boundary condition and the continuity. If we have two joint materials with different properties, continuity conditions between them mean continuity between tangential components of $\vec{E}$ and $\vec{H}$ and between normal components of $\vec{j}$ and $\vec{B}$ [108]. The core of the FEM method is that we can approximate the abovementioned Helmholtz equations with equation (3.19) by using the second order of that equation. As a result, we get a system of linear equations $A \cdot x = B$ which can be solved by matrix calculation. To find field vector x, we need to find the inverse matrix of A, which is the critical point regarding the robustness and complexity of the simulation.

3.5 COMSOL Multiphysics

COMSOL Multiphysics is a numerical software package that solves various discretized problems using direct or iterative solvers [111]. Especially for massive objects and problems, direct linear solvers are always better avoided because of their huge RAM consumption and speed. All direct solvers and iterative solvers have the same task – to solve matrix $A \cdot x = B$. Direct solvers use LU factorization on matrix A to compute the solution x. "MUMPS" solver (or multifrontal massively parallel sparse direct solver) uses some preordering algorithms to minimize the fill-in of that matrix. Two other direct solvers, PARDISO and SPOOLES, are also based on LU decomposition. The dense matrix solver deals with general systems of the form $A \cdot x = B$.

On the other hand, the iterative equation solvers approach the final solution step by step. At some point, the error is below a predefined threshold, and the simulation stops. COMSOL Multiphysics offers different iterative solvers, such as GMRES ("generalized minimum residual"), BiCGStab ("biconjugate gradient stabilized"), FGMRES ("flexible generalized minimum residual"), Conjugate gradients, and TFQMR ("transpose-free quasi-minimal residual"). For all these iterative solvers, the proper preconditioner has to be chosen [112].

Which solver will be used is also related to the simulation study steps. Stationary studies and study steps are used for stationary solvers. Time-dependent studies and study steps are used for the time-dependent solver, time discrete solver, and frequency-to-time FFT (fast Fourier transform) solver. Our FEM simulations are the most important frequency domain studies and study steps that cover frequency domain solver, frequency domain perturbation solver, and time to frequency FFT solver. In our work, we used a frequency domain solver. The simulation volume in this thesis has a spherical shape since, in COMSOL, it is easier to realize a spherical than rectangular volume shape. Moreover, a spherical shape has less volume, which helps in simulation speed and memory consumption.

Mesh is one of the most essential simulation settings. There is a huge difference between the size of the nanoparticle and the size of the simulation volume. Therefore, using some transition area, like a rectangular box around metallic nanoparticles is always a good idea. The mesh size of the nanoparticles in our work is 6nm, the mesh size of the rectangular box is 10nm, the mesh size of the ITO layer is 15 nm, and the mesh size of the rest of the structure is $\lambda/5$. The PML layer, which surrounds all structures, is divided into five layers.

COMSOL is a state-of-the-art and widely used simulation tool for scattering formulation because it calculates separately scattered fields from total fields in overall volume space.

4 Optical antennas

As mentioned, optical antennas have been a completely new concept in the last several years [2, 3, 4, 5, 6, 7, 75]. They are devices designed to capture propagating EM waves and confine and enhance them. Therefore, optical antennas give us highly localized energy as a counterpart of classical antennae. Their usability increases because of the miniaturization of electronic circuits because of the spectral range of operating work. Researchers also developed sub-wavelength resonant antennas, so we can say antennas cover almost the entire electromagnetic spectrum. Therefore, they could be applied in sensing, energy harvesting, imaging...

From the fabrication point of view, electron-beam lithography is a widely used nanofabrication technique for these antennas. Over the years, this technique has improved since resolution has improved.

One of the challenges all scientists face when we talk about optical antennas is scaling. This is because optical antennas are different from the standard microwave or RF antenna scaling behavior. As discussed in the previous chapter, metal exhibits plasma behavior when nano-sized metal interacts with EM radiation. This is why designing optical antennas and finding good scaling laws is difficult. Further, as is very common, metals are described as perfect conductors in RF theory. In the optical regime, the dielectric function of the metal becomes crucial. The reason for this is loss in metal at high operating frequencies. Researchers therefore use many methods for optical antenna investigation and modeling (FEM method, FDTD method, method of moments, boundary method...). All these methods give us the possibility to predict antenna resonant behavior. But anyway, when we describe optical antennas, we can start from some valid postulates for their RF and microwave counterparts.

The key parameter of nanoantennas is radiation efficiency [58, 61]. This parameter shows the ability of the antenna to convert incoming light to useful energy. Researchers try to use nanoantennas to overcome the problem of the low efficiency of standard silicon-based solar cells through light trapping. This topic will be discussed later.

All simulation studies are carried out using the Finite Element Method (FEM) [113] via the commercial software package COMSOL [111]. A maximum mesh element size of 6 nm for all ROAs in this thesis. Except for ellipsoid ROAs, all other structures are comprised of rod-like antenna arms as rectangular geometric blocks with rounded corners to avoid electromagnetic field singularities. In the remaining area surrounding the nanostructure, the maximum mesh element size is 80 nm. The dielectric constants for gold are taken from [51]. The simulation

domain has a spherical shape with a radius of 600 nm. All ROA models are surrounded by a sufficient number of perfectly matched layers (PMLs) in the x, y, and z directions. The numerical models include the ROA supporting layers, such as glass and 50 nm thick ITO (indium tin oxide). The optical response, such as the absolute scattering and absorption cross-section as a function of varying arm length, is calculated in the wavelength range from 500 nm to 1000/1200 nm. Furthermore, the 3-D Maxwell solution of our model gives the quantities of the current distribution with its vector representation over the entire volume of the ROA as a function of wavelength. The designed nanoantennas are illuminated by an electromagnetic plane wave propagating from the substrate side with linear polarization properties as indicated in the following. In all simulation results in this paper, absorption, and scattering cross-sections are calculated according to classical antenna theory [54].

4.1 Ellipsoid-shaped antennas

The influence of the particle shape on resonance behaviour is crucial for our investigation. In many cases, it has been proved that for fixed particle volume, we can tune the antennas and tune the antenna resonance just with the antenna shape modification. In Figure 4.1 is one example of that shape modification.

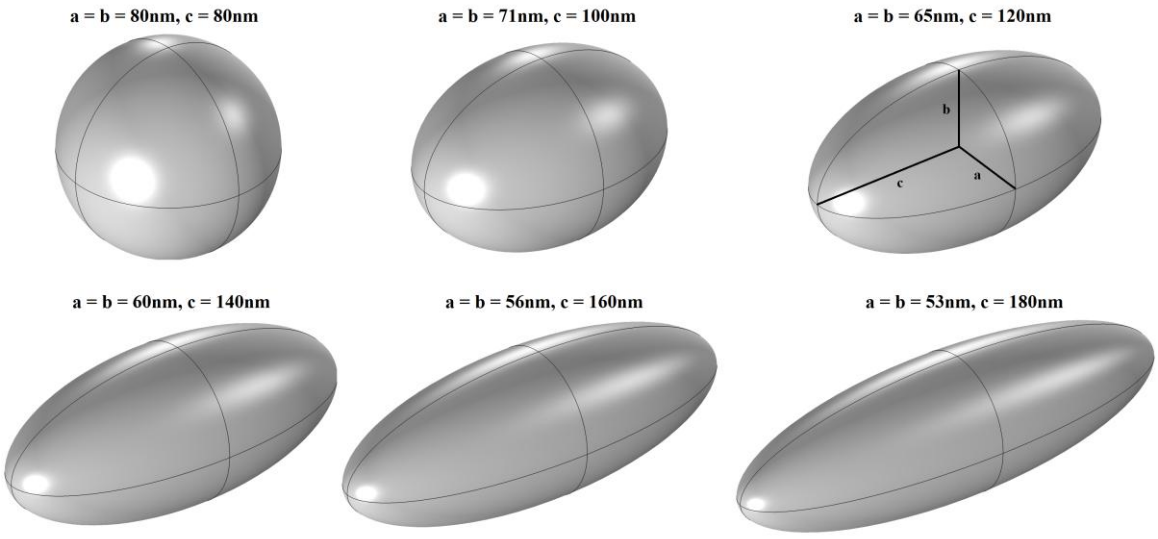

Figure 4.1: Representation of particle shape changing from sphere to ellipsoid by keeping the volume constant. Smaller semi-axes a and b are always equal in all simulation steps.

A maximum mesh element size of 6 nm is used for the rod-shaped, L-shaped, and cross-shaped ROAs, which are comprised of rod-like antenna arms as rectangular geometric blocks with rounded corners to avoid electromagnetic field singularities. Also, the same maximum mesh element size is used for ellipsoid nanoparticles and the meshing of slots in the slot antennas chapter. In the remaining area surrounding the nanostructure, the maximum mesh element size is 80 nm. The simulation area has a spherical shape with a radius of 600 nm. All ROA models are surrounded by a sufficient number of perfectly matched layers (PMLs). The numerical models cover the ROA supporting layers, such as glass and 30 nm thick ITO (indium tin oxide), using the appropriate dielectric function, respectively. For all rod-shaped, L-shaped, and cross-shaped ROAs geometries, we keep the height (H = 30 nm) and the width (W = 20 nm) constant. We calculate the optical response function, such as the absolute scattering and absorption cross section, as a function of varying arm length in the wavelength range from 500 nm to 1000 nm. Our parameters are chosen to be as close as possible to our experimental capabilities [114, 115, 116]. Furthermore, the 3-D Maxwell solution of our model gives the quantities of the current distribution with its vector representation over the entire volume of the ROA as a function of wavelength. The composite is illuminated by an electromagnetic plane wave propagating from the substrate side with linear polarization properties, as indicated in the following Figure 4.2. We start from a gold sphere with a radius of 80 nm. This sphere we modify to an ellipsoid, which has the same volume as a given sphere. The results are in Figure 4.2. From this first simulation set, it is clear how particle shape tuning in the direction of polarization strongly influences resonance behavior even if particle volume is constant. Significant red shifting with increasing the axis in the direction of light polarization direction is noticeable. We will use this nanoantenna behavior in solar energy harvesting.

We can recognize two distinct modes, longitudinal and transversal, for these two polarizations and their vector representations of the current density. It is necessary to pay attention to the fact that in Figure 4.3, the color scaling for these two resonances is not the same. The transversal high-frequency mode gives rise to the ROA resonance at 568 nm, whereas the longitudinal low-frequency mode gives rise to the ROA resonance at 708 nm. Therefore, we can say that this nanoparticle shows bimodal behavior under proper polarization conditions. From Figure 4.2, it is clear that both resonances are noticeable for the scattering events.

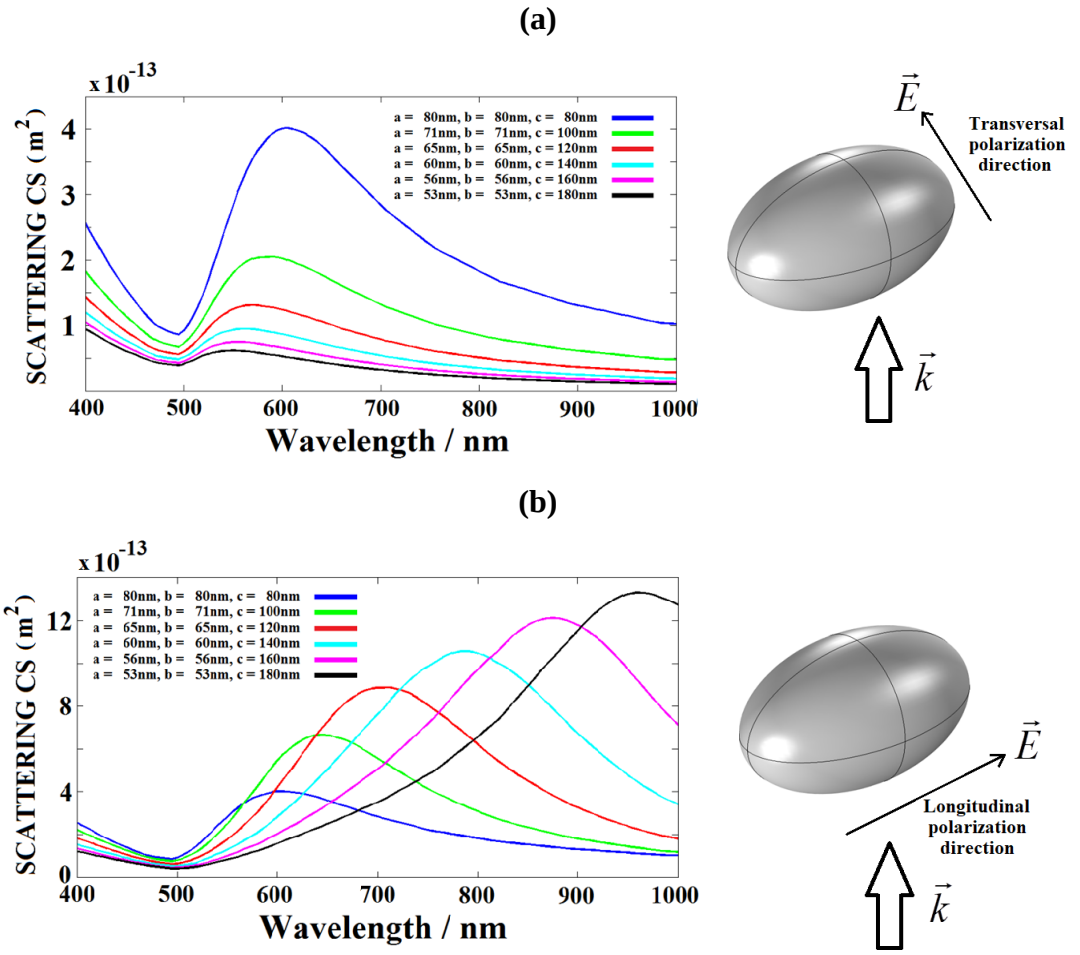

Figure 4.2: Far field optical properties of single ellipsoid-shaped ROAs with increasing one semi-axis and decreasing second semi-axis to keep the volume constant in all simulation steps. a) polarization direction is parallel to the longitudinal axis of ROA; b) polarization direction is parallel to the transversal axis of ROA. The scattering cross section is calculated according to classical antenna theory.

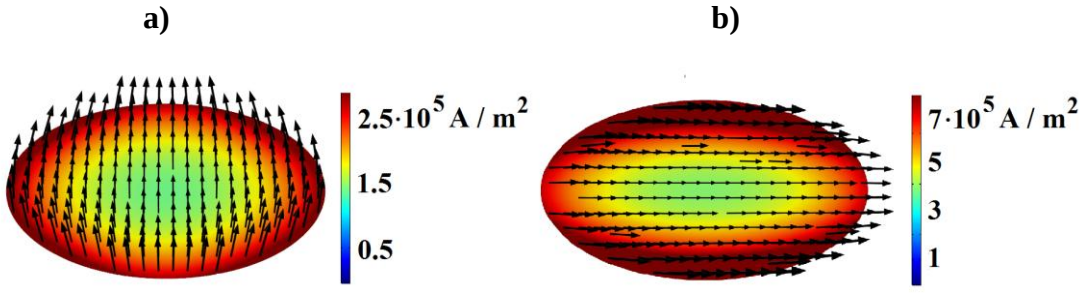

Figure 4.3. The current density of two resonances of ellipsoid optical antenna. Semi-axes are lengths a = 65 nm, b = 65 nm, and c = 120 nm. The color bar is J (current density) with the vector representation of the current modes. a) ROA resonance 568 nm transversal polarization; b) ROA resonance 708 nm for longitudinal polarization

4.2 Rod-shaped single and coupled rod-shaped nanoantennas (dipole antennas)

4.2.1 Rod-shaped single nanoantennas

The next step in our investigation is numerical simulations of rod-shaped ROAs with a small width compared to the rod length. Those particles have a small aspect ratio.

Dipole-coupled optical antennas are among the most common nanostructures designed to produce so-called hot spots. In these spots, the EM field is enhanced by two or even three orders of magnitude. Three geometrical parameters influence the field enhancement: rod length, gap width, and aspect ratio. Non-geometrical parameters, of course, include antenna material and surrounding medium. Coupled antennas can confine the field to a volume below the diffraction limit, defined by the gap dimensions. These structures could operate in the visible and near-IR [1]. In our investigation, we mainly focus on the length of the rod. Both types—single rod antennas and coupled antennas—show monomodal behavior. In the case of the dipole antennas, our examination also addresses gap size. Figure 4.4 shows a dipole rod-shaped antenna taken from the literature. As can be seen, the main dimensions of those coupled ROAs are length (L), width (W), height (H), and gap (G). Each of these values has a specific influence on final ROA performance, including resonant wavelength or frequency, the amount of scattered and absorbed light, field enhancement, and curve shape (width of the half bandwidth, for example). Moreover, in all these performances, the polarization direction also exerts a strong influence.

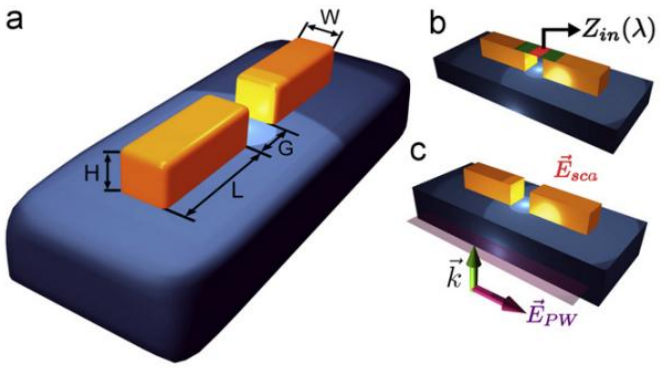

Figure 4.4: Representation of dipole antennas placed on the dielectric substrate, taken from [58]

Furthermore, Figure 4.5 a) shows a simplified configuration of the single rod ROA drawn in COMSOL Multiphysics. In our investigation through this thesis, all physical dimensions for simulations are chosen to follow electron-beam lithography abilities. As shown, the polarization direction is along the longitudinal direction of the antenna.

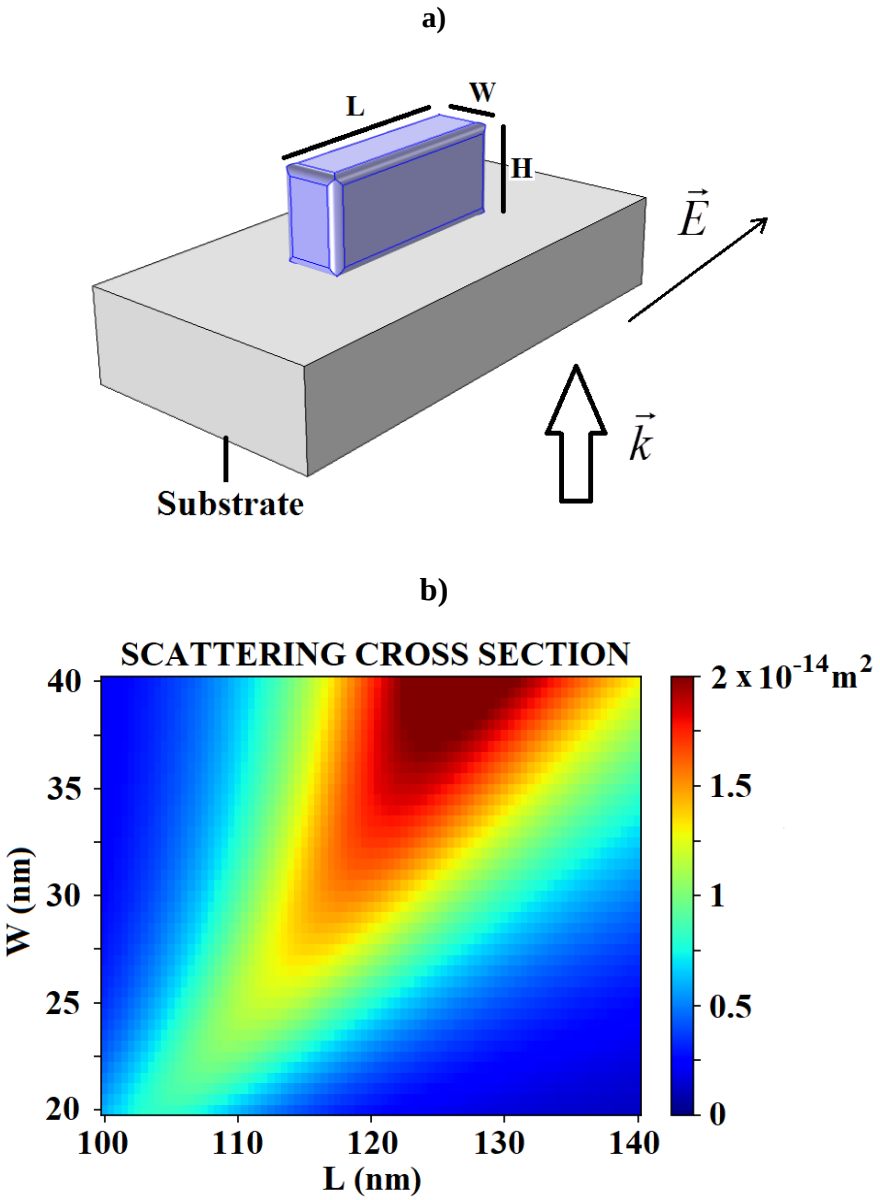

Figure 4.5: a) Representation of single rod antenna placed on the ITO/glass substrate. The picture is drawn in COMSOL Multiphysics. b) Plasmonic heat map. Here are calculated scattering cross sections for different combinations of L and W for the single rod-shaped ROA on a constant wavelength of 810nm and constant height of 30 nm.

Figure 4.5 b) shows a plasmonic heat map. In this way, it is much easier to see which combination of L and W gives the maximum at scattered light at constant height, dielectric

properties, and wished wavelength. Results show that for every value of antenna width (W), there is some value of antenna length (L) for which ROA gives the maximum of the scattered light on the wavelength 810nm and constant height 30 nm. For example, for the width W=20 nm, the best value of antenna length is somewhere between 100 nm and 110 nm; for the width W=30 nm, the best value of antenna length is between 115 nm and 120 nm, etc. In our investigation of the single rod, we choose a width of W=20 nm. The polarization direction in all simulation steps will be parallel to the longitudinal axis of the rod. Height is 30nm, and length varies from 50 to 100 nm.

As shown in Figure 4.6, there is a red shifting of the resonant wavelength while rod length increases. These results are, of course, in accordance with the antenna theory [54]. This behavior is also noticeable in the case of coupled rod-shaped antennas, which will be shown later. According to the Mie theory, particle volume increment results in a higher amount of scattered and absorbed light on a particular wavelength. If we compare the length of the nanoparticle and resonance peak position, we will notice linear dependency, which can be expressed as a formula. Figure 4.7 shows the spectral position of resonance as a function of the antenna length.

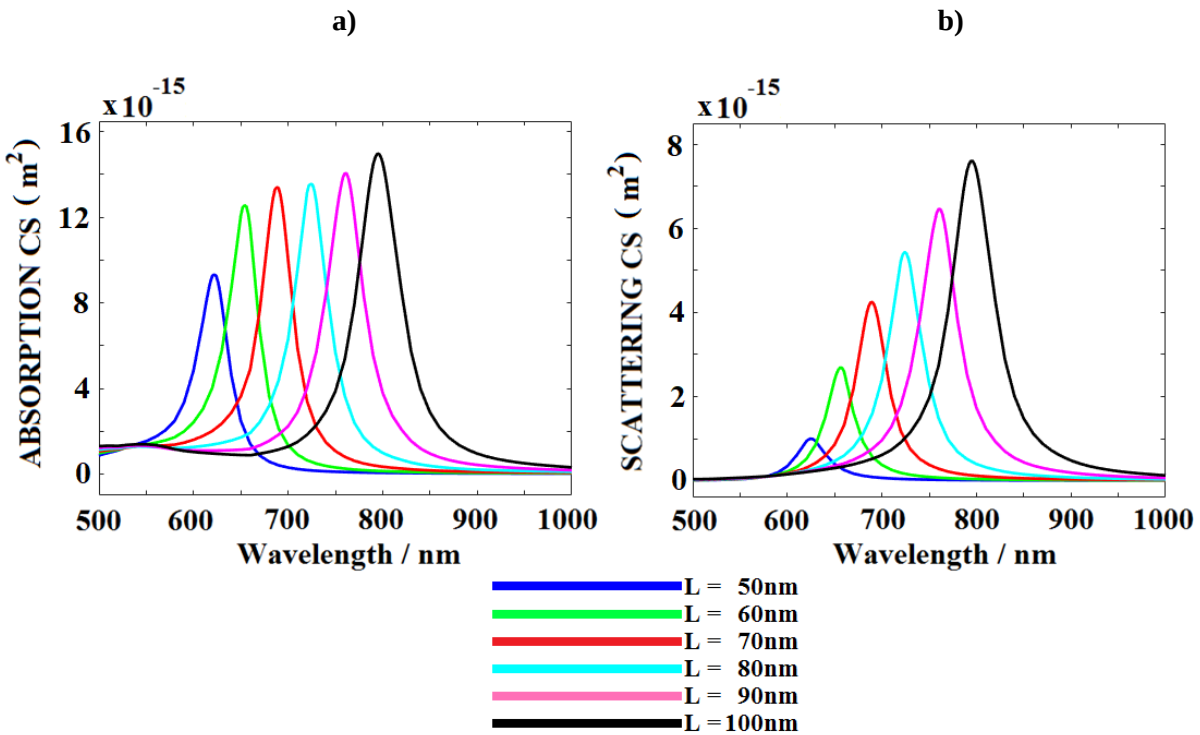

Figure 4.6: Far-field optical properties of rod-shaped ROAs with the increasing the length in all simulation steps. a) Absolute absorption cross-section; b) absolute scattering cross-section.

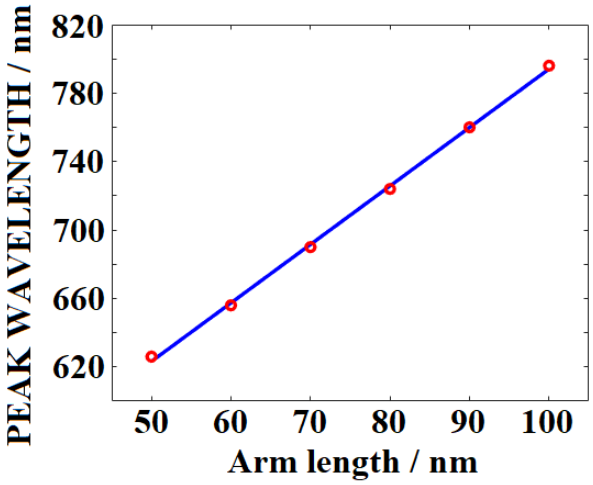

Figure 4.7: Linear dependency between arm length and resonant wavelength

From the results in Figure 4.7, we can derive an analytical formula for describing the ratio between arm length and resonance wavelength. Of course, this formula can be applied only for this specific substrate and other geometrical parameters, W=20 nm and H=30 nm.

$$\lambda_{RESONANT} = 3.42 \cdot L[nm] + 452\ nm \tag{4.1}$$

Polarization sensitivity will not be deeply investigated here because it is a much more interesting topic for bimodal and triple-modal structures. It is worth noting that varying polarization orientation has an impact, especially on scattering and absorption intensity. Figure 4.8 presents a top view of a single rod-shaped ROA with polarization direction.

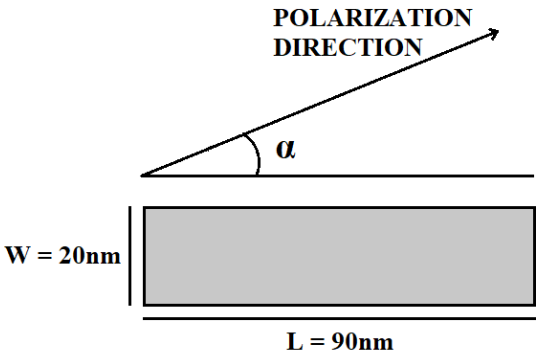

Figure 4.8: Representation of polarization angle for single rod-shaped ROA

In all simulation steps, the geometrical parameters of the antenna are the same. The plane wave comes from the bottom side of the structure, as shown in Figure 4.5. Figure 4.9 does not present

results for the polarization angle of 90^0 because, for transversal mode, spectral response is insignificant in comparison to the other polarization angles to be visible. If we observe the results in Figure 4.9, the highest scattering and absorption cross sections observed a polarization angle 0^0, and the lowest is for a polarization angle of 75^0.

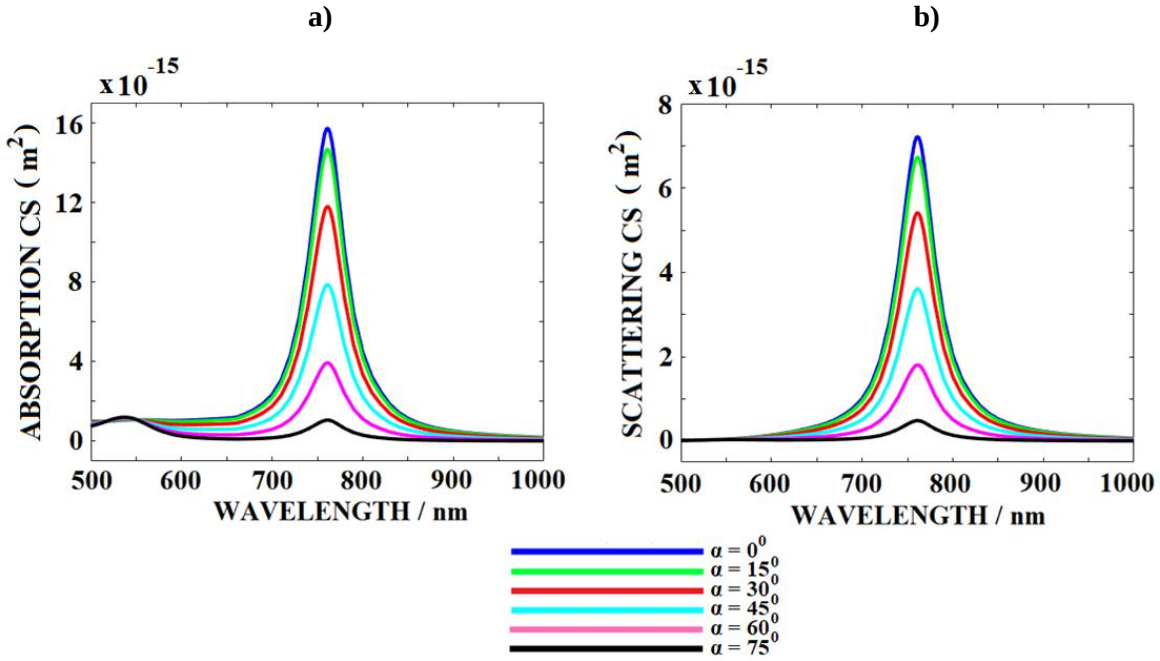

Figure 4.9: Farfield optical properties of single rod-shaped ROA of length L=80nm with changing of polarization angle in all simulation steps. a) Absolute absorption cross-section; b) absolute scattering cross-section.

In Figure 4.10, far-field properties for the transversal mode are shown.

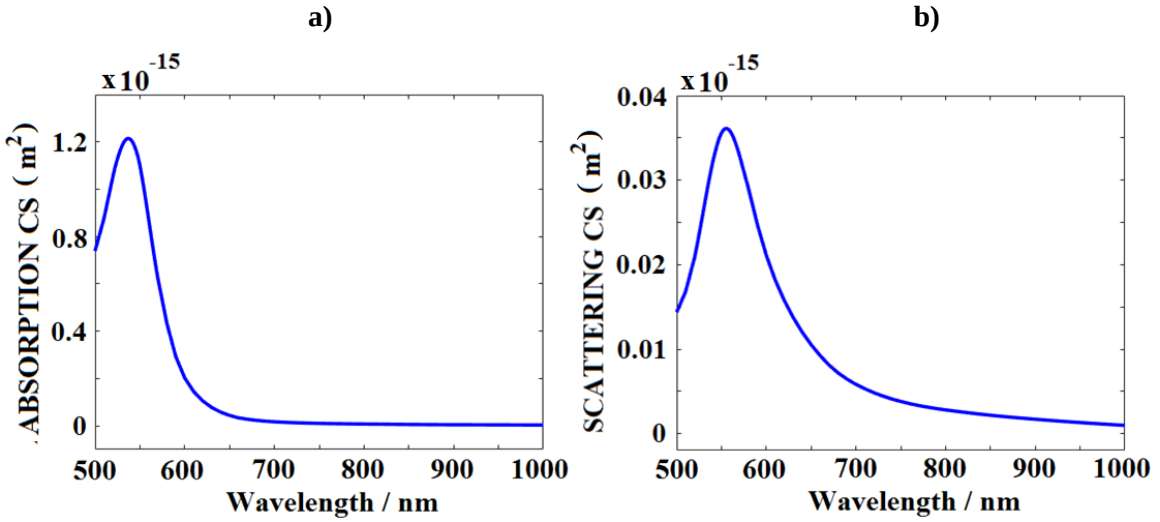

Figure 4.10: Far-field optical properties of rod-shaped ROA with polarization angle of 90^0 (transversal mode). a) Absolute absorption cross-section; b) absolute scattering cross-section.

In Figure 4.11, current density and field lines for both modes, longitudinal and transversal, are shown. As can be seen, color scaling bars are quite different for those two cases since the current density is much higher for the longitudinal mode.

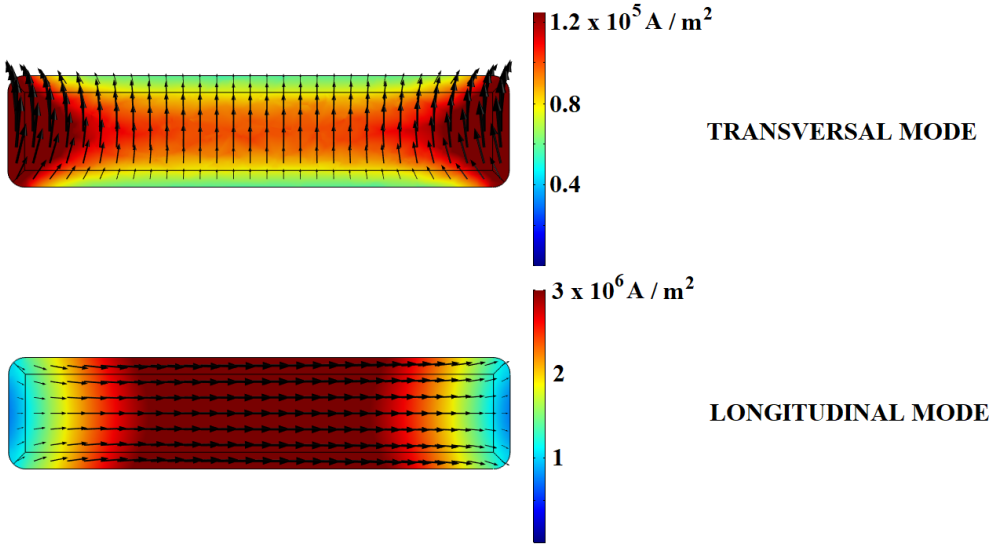

Figure 4.11: Current densities of longitudinal and transversal modes. Arm length is L = 90 nm. The color bar is J (current density) with the vector representation of the current modes: a) ROA transversal resonant wavelength is 555 nm, and b) ROA longitudinal resonant wavelength is 761 nm.

Even here, the transversal mode can be observed; this simple single rod-shaped ROA is considered a monomodal antenna since it has only one longitudinal mode. This transversal mode is possible to excite only if the polarization direction is set exactly to 90^0.

4.2.2 Coupled rod-shaped nanoantennas

The second part of the rod-shaped ROA investigation is dipole antenna–coupled rod-shaped ROA, as in Figure 4.12. Simply said, this nanostructure consists of two metallic rods deposited on a dielectric. The distance between them is the so-called gap width. Gap width (or, more precisely, gap volume) is a crucial parameter for providing field enhancement, which can be used in different applications. This will be explained more in the chapter with bimodal coupled ROAs.

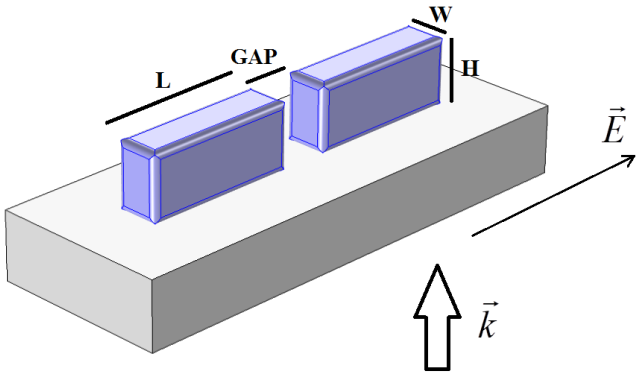

Figure 4.12: Representation of dipole coupled rod-shaped antenna placed on the dielectric substrate.

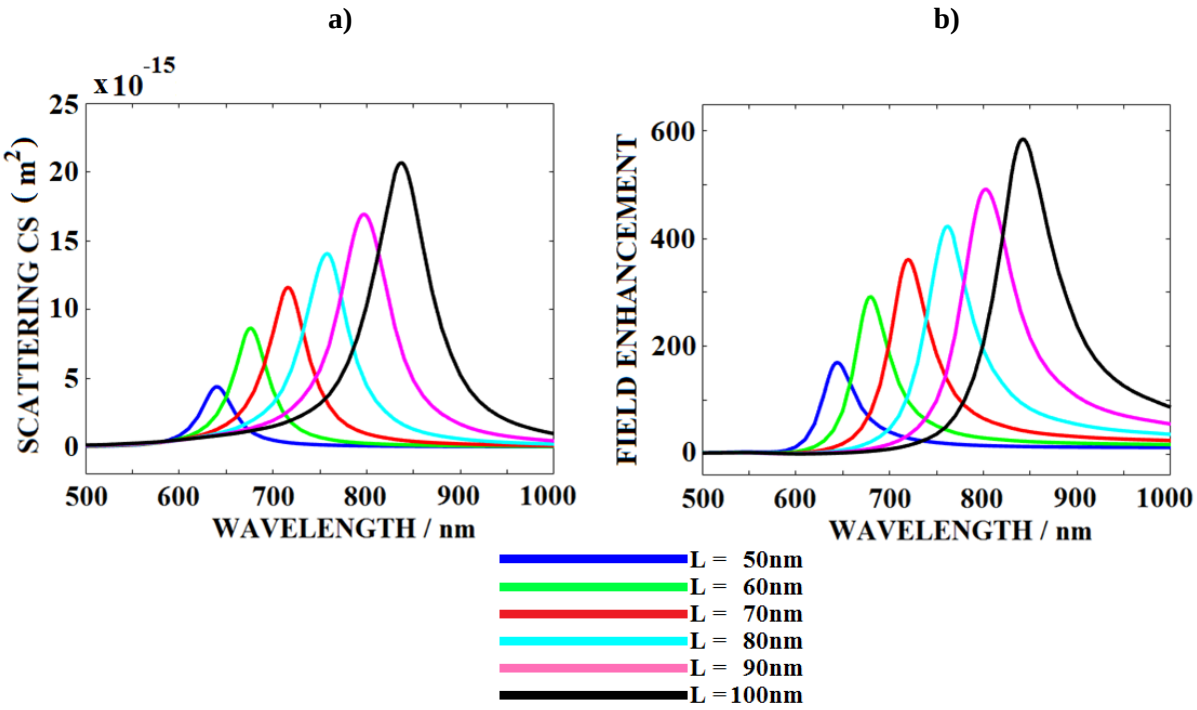

Figure 4.13: Far-field (scattering cross section) and near field (field enhancement in the gap) properties of rod-shaped coupled antennas from Figure 4.12 with increasing rod length. a) Absolute scattering cross-section; b) field enhancement. Here, field enhancement is $|E_{TOT}|^2/|E_{IN}|^2$.

In this thesis, whenever we analyze near-field properties of coupled ROAs, we will always calculate field enhancement in the center of gap volume. More precisely, that point of calculation will be at the center of the gap width and in the middle of the antenna height. Besides all the information given in the investigation of a single rod-shaped antenna, in Figure 4.13, it is noticeable that for longer antennas, the field intensity in the gap increases. This is because for longer rods, the gap width has a smaller effective length, and that causes stronger

coupling between rods. This leads us to investigate how field enhancement in the gap is influenced by width variation if we keep the rod length constant.

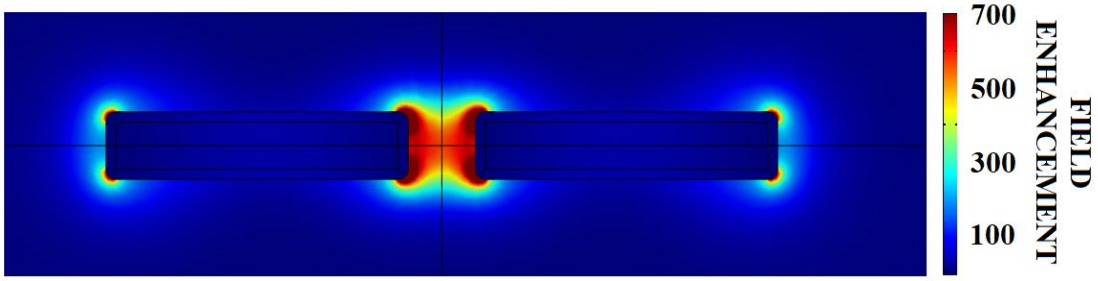

Figure 4.14. Near field distribution of the field intensity enhancement. The arm length is 90 nm, and the resonance wavelength is 804 nm. The field distribution is plotted in the middle of the antenna height. Color bar or field enhancement means $|E_{TOT}|^2/|E_{IN}|^2$.

In Figure 4.14, a plane is presented, which is the top view of the antenna. The plane is cut in the middle of the antenna height and represents field enhancement in comparison to the field intensity of the incident wave.

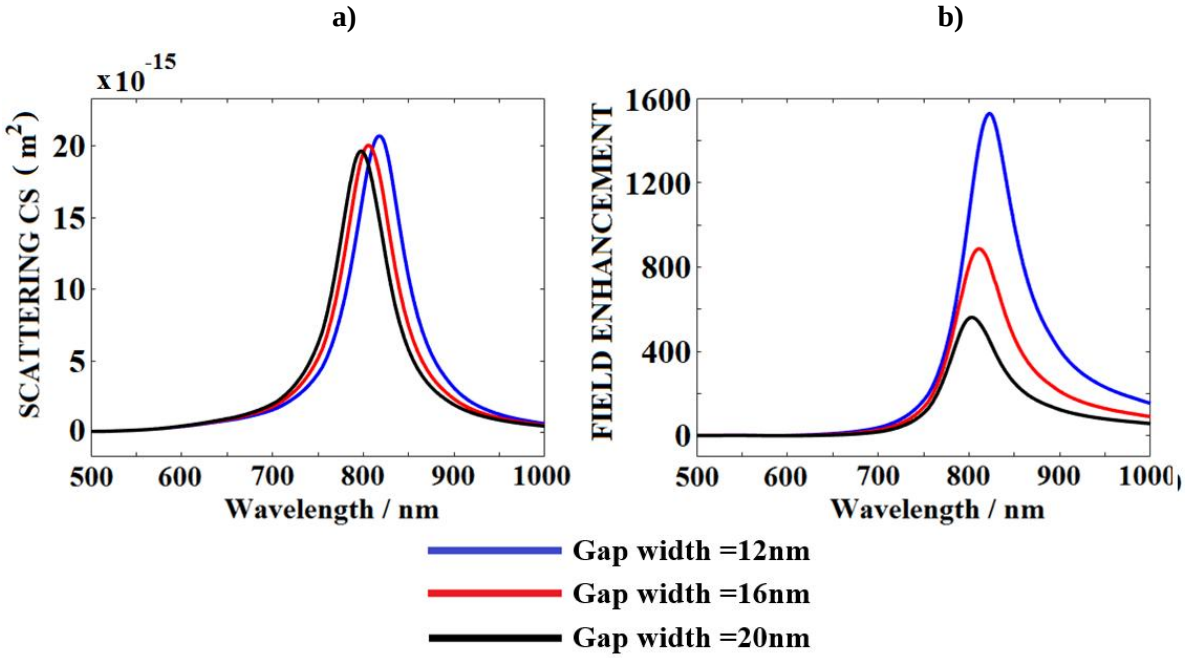

Figure 4.15: Far-field (scattering cross section) and near-field (field enhancement in the gap) properties of rod-shaped coupled antennas with gap width variation. a) Absolute scattering cross-section; b) field enhancement. The length of the rod is L = 90 nm. Here field enhancement is $|E_{TOT}|^2/|E_{IN}|^2$.

Dipole-coupled antennas (like every other coupled antenna) confine the field in a volume well below the diffraction limit. In this case, volume is defined by gap width. As we already know, a dipole rod-shaped antenna is a monomode. It was also presented that gap width greatly influences field enhancement. This is supported by Figure 4.15, which shows far-field and near-field results (scattering and field enhancement in the gap, respectively).
Table 4.1 shows relevant data.

Table 4.1: Far-field (scattering cross section) and near-field (field enhancement in the gap) resonant wavelengths and for different gap widths of coupled rod ROAs. The length of the rod is L = 90 nm

Gap width / nm	**Resonant wavelength / nm Far-field**	**Resonant wavelength / nm Near-field**
12	818	823
16	806	811
20	798	803

If we analyze data from Table 4.1, the first obvious conclusion is that there is a spectral between near-field and far-field resonant wavelengths for all gap widths. In all three cases, that shifting is 5nm. This is in agreement with many papers that have done an analytical analysis of that shifting with a Lorentzian model.
Another conclusion is that the spectral blue-shifting of the resonance with gap width increases the spectral blue-shifting of the resonance with an increase in gap width. The explanation is based on the analysis of the capacitance of the gap and corresponding resonant frequency. As we know, the resonant frequency is inversely proportional to the inductance and capacitance of the element so that we can write $f_{RES} \sim \frac{1}{\sqrt{L \cdot C}}$. From formula (2.89), we can see that increasing the gap width will most likely decrease resonant frequency and, therefore, increase resonant wavelength. This is an explanation of spectral shifting influenced by gap width changes.

4.3 Discussion

This section will present a discussion of the obtained results with literature that is directly related to the L-shaped and cross-shaped ROAs .

The work [25] describes in detail the theoretical and experimental study of the particle plasmon resonances of L-shaped gold nanoparticles. Here, the higher-order mode is analyzed. For very small L-shaped nanoparticles, resonant behavior mostly depends on the particle width. In this work, L-shaped ROAs are symmetric (arm lengths are the same). In this investigation is first time explained polarization sensitivity of these structures. The polarization direction in this work is rotated by 45 deg for the arm directions. Like in this thesis is shown, this paper proves how two resonances can be excited simultaneously. Moreover, here is a presented comparison analysis between L-shaped ROA and single rod-shaped ROA plasmonic behavior.

In work [26], a Quarter-Waveplate composed of four gold L-shaped ROAs is presented. The polarization of these antennas is also analyzed, and the investigation is performed using the FDTD method. This nano waveplate can convert linear polarization to circular polarization and vice versa. It is compared for different arm lengths.

In [27], polarization conversion is analyzed through two mechanisms: Structural asymmetry and plasmon hybridization through strong coupling. For this investigation, an L-shaped nanoparticle consisting of two metallic nanorods is used. For simulations, the Green Dyadic Method is used. The case with different arm lengths is also analyzed here.

In [28], metamaterial is analyzed based on graphene. It has two parts: a rod-shaped graphene strip and an L-shaped graphene block. The intention is to generate the plasmon-induced transparency (PIT) effect.

[29] presents a nanopolarization converter made of L-shaped slots in gold film. It is analyzed in high-order and low-order magnetic plasmon resonance mode with the FDTD method. Here, it is explained in detail how we can excite a particular mode with a certain polarization angle.

A very interesting work in [30] is theoretically and experimentally investigated polarization-independent and dual-band infrared perfect metamaterial absorbers. It is made of three layers. The bottom layer is a gold film, the middle layer is a dielectric spacer, and the top layer is an L-shaped gold nanoparticle. Due to two resonant modes, this structure has two absorption peaks. It is shown that this structure has very good absorption stability for different azimuth and incident angles for both TE and TM polarization. Therefore, it is very useful in infrared spectroscopy and imaging. Used method for analysis is the finite element method and CST Studio software. Moreover, this work analyzes the absorber with a single L-shaped, but also with double L-shaped nanoparticle on the top of the dielectric spacer.

In [31] can be found the analysis of L-shaped nanoparticle with the same and with different arm lengths. Also, it is performed comparison between L-shaped and pure rod-shaped ROAs.

Work [32] describes how arrays of L-shaped nanoparticles can be used for ultra-thin wave plates in two regimes: strong inter-particle coupling and weak inter-particle coupling. As usual, two different modes, symmetric and antisymmetric, are analyzed.

Real application is investigated in [33]. Super-resolution imaging with quantum dots is a method to probe plasmonic near-fields, but there is always some emission intensity and radiation pattern distortion. The interaction between the quantum dot and ‘L-shaped’ ROA leads to the mislocalization of 100 nm and mispolarization of 30° of the quantum dots compared to the initial emission. The task of L-shaped nanoantennas is to provide polarization-dependent changes.

In [34], coupling in orthogonal L-shaped dimer gold nanoantennas is investigated, where tuning antenna length or gap size can excite both bonding and antibonding resonances.

[35] explains how to design an ultra-thin optical vortex phase plate with an L-shaped nanoantenna array. Thanks to the polarization sensitivity of L-shaped ROAs, this structure is suitable for both linear and circular polarizations.

[36] provides numerical analysis of bimodal asymmetric L-shaped ROAs, both coupled and single versions. It also shows detailed mode analysis and reconstruction and compares their behavior with single rod-shaped ROAs.

If we have two metallic rods and some gap between them, the phase in the feed gap of this "dipole antenna" shows a transition from in-phase to out-of-phase response when its length varies across the resonance length. In [37], is used this behavior for making a cross-shaped antenna that consists of four rods that share one gap. This can be described as two perpendicular dipole antennas with the same feed gap. This cross-shaped antenna is asymmetric, so the lengths of these dipole antennas are not the same. Therefore, building two field enhancements in the gap is possible but a phase difference of 90°. Thus, cross-polarization is built.

[38] is experimental work related to the [37].

Work [39] is very similar to the [37] conceptually, but the shape of the antenna is different. Here, instead of two dipoles consisting of rods, we have two dipoles consisting of bowtie nanoparticles. This paper investigates the cross-shaped antenna array numerically and experimentally and its nanofocusing in the near-IR spectrum.

In [40], detailed analysis of bimodal cross-shaped ROAs, both single and coupled versions, is shown. For the first time, it is also presented how a cross-shaped ROA can show triple-modal behavior under some geometrical and polarization circumstances.

In [41] author gave numerical analysis of the array of coupled bowtie-shaped ROAs. This structure is monomode, and the gap width is 5nm.

The best comparison with our proposed design can be found in [42]. It analyzes coupled bowtie-shaped ROA, with a gap width of 2nm. This work covers single, double, and triple bowtie coupled structures. In this thesis comparison with this work is in Table 1.

4.4 Bimodal single L-shaped antennas

As mentioned before, nanoparticle shape is the main variable determining the particle plasmon resonance frequency for the already chosen nanoparticle material and environment. That means that by shape modification, we are able to control resonance properties since, for some applications, it is necessary to reach resonance at a certain wavelength or wavelengths. However, the particle plasmon frequency as a function of geometrical effects is qualitatively known and has arrived at a quantitative and shape-independent level by introducing the so-called plasmon length, the length scale over which the free electron oscillation takes place [9]. This intrinsic size parameter called plasmon length is found to be an important resonance design toolbox for arbitrarily shaped different nanoparticle plasmon.

In the emerging field of resonant optical antennas (ROAs) [2], the scaling laws for their antenna resonance frequency have been motivated by the RF-antenna community language and tools [117]. These nanostructures can be simulated by numerical methods by using sophisticated 3-D Maxwell solvers [111, 118]. Expanding the ROA architecture towards L-shaped configurations opens pathways for polarization-sensitive plasmon resonance frequencies with fundamental dipolar mode and the so-called three-pole resonance, which originates from the symmetric current mode running along the antenna arm of the asymmetric L-shape.

L-shaped resonant optical antennas are well-known low-symmetry plasmonic nanostructures showing two tunable resonances in the optical and near-infrared wavelength regions. The plasmon length of these asymmetric L-shaped ROAs can be used as plasmon resonance building blocks to design polarization-sensitive devices. As will be seen, these structures are very polarization-sensitive.

Section 4.3 analyzes literature already published regarding L-shaped nanoantennas.

This thesis will introduce novel designs of ROAs based on asymmetric L-shapes with plasmon length tuning and high-electric field enhancement. These L-shaped ROAs exhibit two resonances or a bimodal longitudinal antenna resonance behavior. It will also be shown that it is possible to control the excitation of these two resonances individually while changing the linear polarization angle. The asymmetric L-shaped single ROAs resonances can be interpreted conceptually as tuning the plasmon length accordingly by "fusing" rod-like single particles. This analysis opens a design route for multiple plasmon resonances that match the conditions for future nano-optical active circuits.

Figure 4.16 shows the reported asymmetric L-shaped nanoantennas design in top and 3D views. In this study, the height (H) and the width (W) are kept constant at 30 nm and 20 nm, respectively. Lithographic techniques were reported in [114, 115, 116] for the fabrication of these antennas. The nanoantenna arm length varies from 20 nm to 80 nm in steps of 20 nm.

Firstly, we present the simulated structures and explain the strategy to identify the plasmon length for size-evolving asymmetric L-shaped ROAs. Then, we interpret those findings with plasmon length tuning as a toolbox for bimodal plasmon resonance ROAs.

We start our simulations by studying the two principle configurations as indicated in Figure 4.16 a).

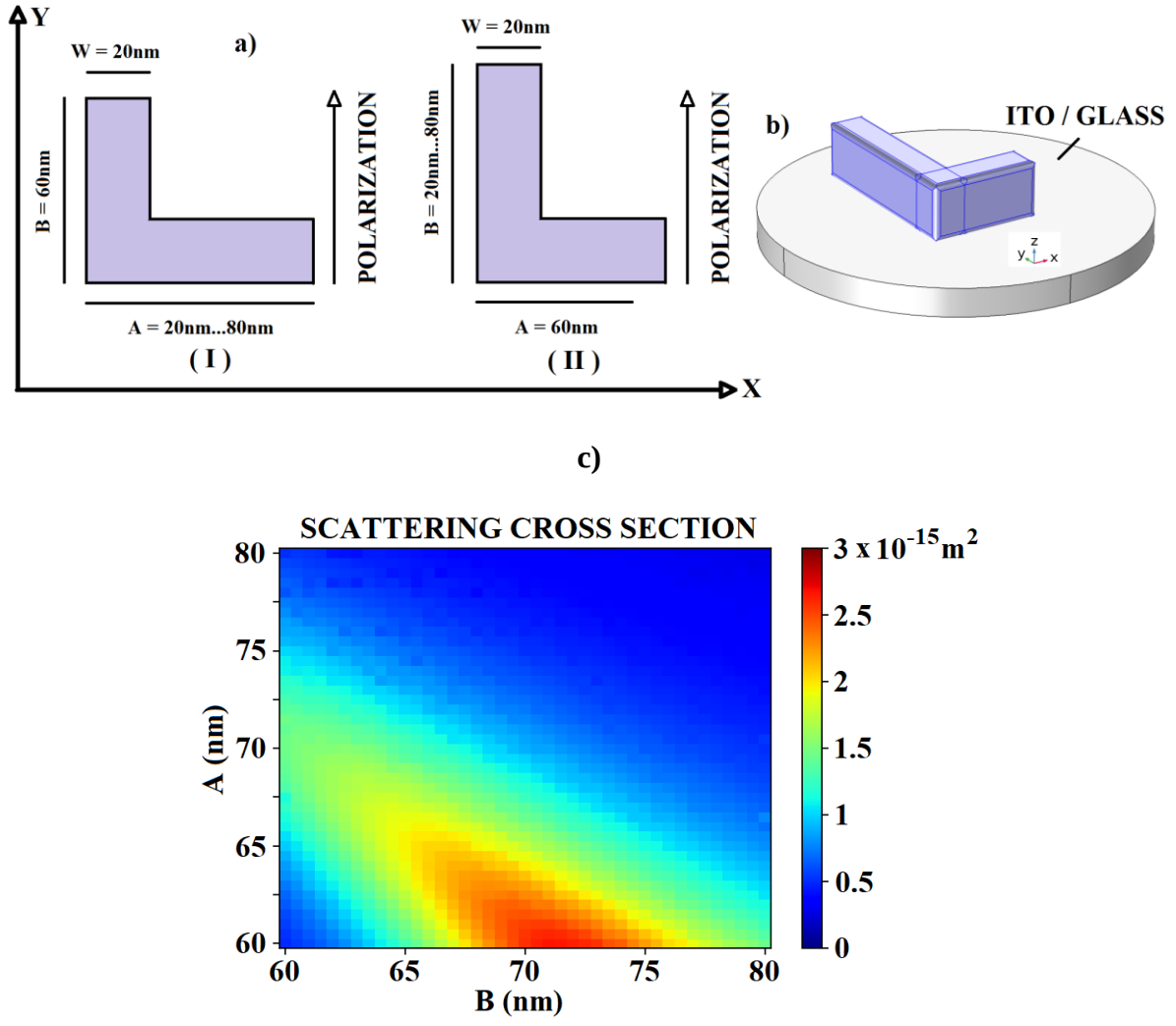

Figure 4.16: a) Top view of a single L-shaped ROA (x-y plane) with the antenna arms termed A and B in two configuration (I, II) for the linearly polarized plane wave excitation; b) 3D scheme of gold L-shaped ROA on glass; c) plasmonic heat map for scattering cross section of single L-shaped antenna for constant height and width on the wavelength 810nm.

As a first step in this investigation, we will choose ranges between 60nm and 80nm for dimensions A and B. Polarization orientation is in the direction of arm B or parallel to the y-axis, as indicated in Figure 4.16 a). The plasmonic heat map indicates that the highest scattering cross section on 810nm is where A is 60 nm and B is around 70-75 nm. At the same time, if we observe a scattering cross-section in the area where B is 60nm and A is around 70 -75 nm, it is obvious that the scattering cross-section is significantly higher when B is longer than A. Therefore, it can be concluded that the scattering cross section is higher if the polarization direction is parallel to the longer arm and not the shorter arm.

After this basic conclusion, further investigation will be performed by changing A or B. Asymmetric L-shaped ROA arms (here termed: A, B) are co-aligned with the Cartesian coordinate axes (x, y). The linear excitation polarization of the electromagnetic plane wave is set parallel to the y-axis. For each wavelength, as is indicated above in Figure 4.16 a), one of the ROA arm's lengths is increased from 20 nm up to 80 nm individually in steps of 20 nm while the corresponding other ROA arm is held constant at 60 nm. By this method, we generate a set of four ROAs with two orthogonal configurations of rod-like antennas (here termed: I, ROA starting geometry being parallel to the linearly polarized wave and II, ROA starting geometry being perpendicular to the linearly polarized wave) for the linearly polarized plane wave excitation. Thus, we evolve the typical antenna parameter L/λ (length/wavelength) as a figure-of-merit to derive the ROA resonance scaling and investigate the associated ROA current mode development. For the pure nanorod-like ROA with A = 20 nm, we observe a monomodal longitudinal ROA antenna mode in the absorption as well as in the scattering spectra that origins from the ROA with B=60 nm thus having the particle plasmon resonance property of a gold nanorod with an aspect ratio B / A = 3 that follows literature data [87].

This particular ROA geometry with its associated particle plasmon resonance is a good example of the relevance of a plasmon length, as the longitudinal current mode here shows that its oscillation is pinned to the physical dimension with well-defined nodes at the nanorod's ends. Increasing the ROAs arm length A and thus breaking the symmetry of the nanorod system leads to a development into a bimodal ROA resonance behaviour (Figure 4.17).

When we increase just the length of one ROA arm, it is easy to observe two new ROA resonances that shift both to the low energy side of the spectral bandwidth but with increasing wavelength separation between the bimodal resonance wavelengths. We now switch to the simulation of the ROA for the configuration **II** in Figure 4.16.

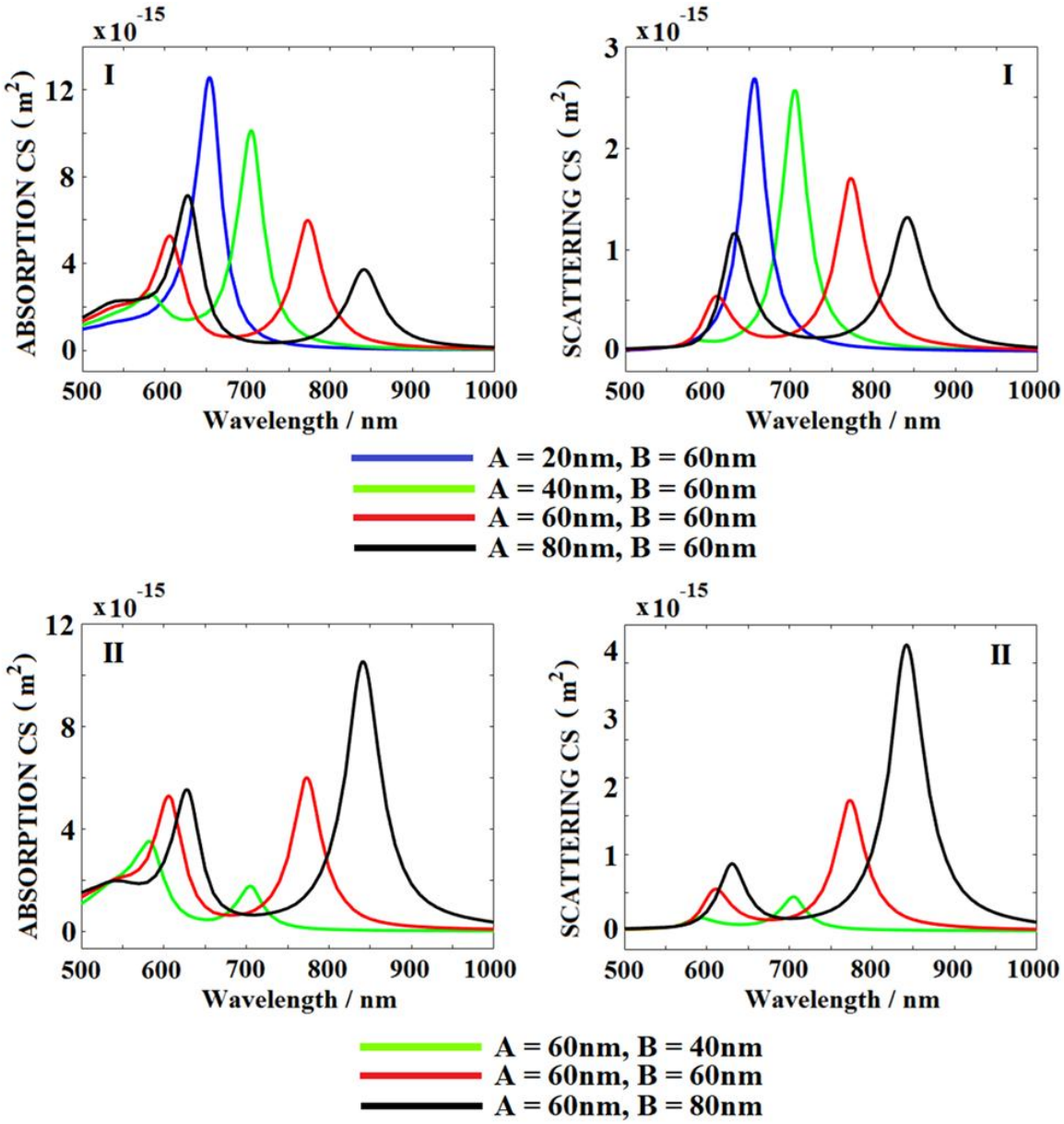

Figure 4.17: Far field optical properties of single L-shaped ROAs with increasing arm length, respectively. I) absolute absorption and scattering section of ROA for configuration I from Figure 4.16; II) absolute absorption and scattering section of ROA for configuration II from Figure 4.16.

The simulation set starts from the rod-like ROA (B=20 nm), while the polarization direction is set in the transversal direction of the rod. In that case, a resonance peak in the absorption spectrum at 540 nm is observed that can be interpreted as the transversal particle plasmon resonance. This is already supported by Figures 4.3 and 4.11 for other nanoparticle shapes, elliptical-shaped and rod-shaped, respectively. Thus, it is not necessary to plot that figure here again. By lowering the symmetry of the ROA from configuration **II** while increasing just the antenna arm length B from 20 nm to 80 nm, we observe a bimodal ROA resonance property

for both the absorption and scattering spectra, developing its frequency shifting and increasing wavelength separation between the two ROA resonances, similar to the case of the ROA **I**. What can also be seen is that this development starts with the transversal particle plasmon mode, and it develops into two longitudinal ROA modes with a high-frequency resonance component and a low-frequency resonance counterpart.

Finally, if we compare the black curves of scattering cross sections for configurations **I** and **II** from Figure 4.17, it is clear that scattering cross sections are higher for A=60 nm; B=80 nm than for A=80 nm; B=60 nm. This is the same conclusion as from the plasmonic heat map in Figure 4.16 c). The previous analysis is also supported by Figure 4.18, which is the current mode representation of the asymmetric L-shaped ROAs for arm's lengths A=80 nm and B = 60 nm.

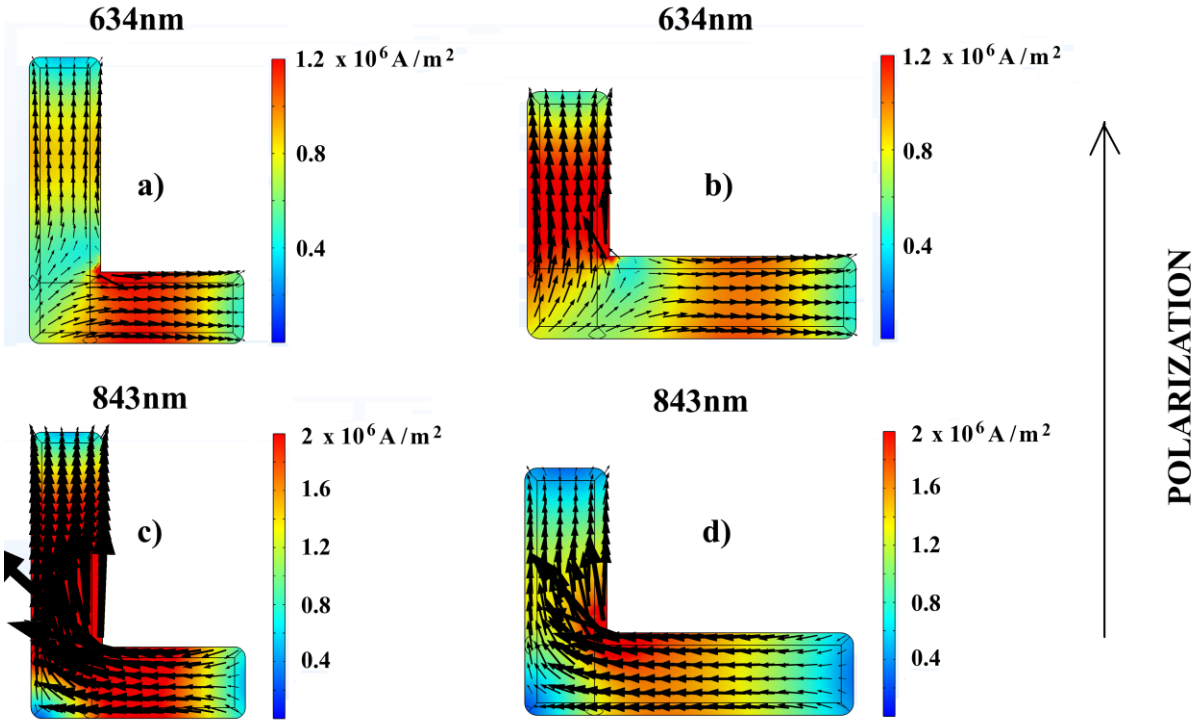

Figure 4.18: Current density of the bimodal ROA resonances. Arm lengths are A = 80 nm and B = 60 nm. The color bar is J (current density) with the vector representation of the current modes for ROA configuration from Figure 3.16. a) and c) ROA resonance wavelengths are 634 nm and 843 nm for polarization direction along the x-axis; b) and d) ROA resonance wavelengths are 634 nm and 843 nm for polarization direction along the y-axis

It shows the current density of the bimodal ROA high-energy and low-energy resonances for the two polarization directions at the two wavelengths of $\lambda = 634$ nm and $\lambda = 843$ nm, respectively. For both polarization directions, we can observe from their vector representation of the current density two distinct modes linked to the bimodal resonances of the L-shaped ROA. The signatures of both polarization directions exhibit the same qualitative current mode pattern. The low-frequency ROA eigenmode can be assigned to a slightly perturbed – bent – longitudinal current mode, giving rise to the ROA resonance at 843 nm, while the high-frequency ROA resonance at 634 nm has a current mode signature of an out-of-phase longitudinal resonance oscillating along each individual ROA antenna arm A and B.

In these plots, it can be seen that despite the polarization orientation mismatch of the asymmetric L-shaped ROA with respect to the linearly polarized excitation plane wave, the highest current density amplitude is exclusively located at the shorter ROA arm of the L-shaped antenna, giving rise to the 634 nm ROA resonance.

The fundamental analysis of ROA performance is correlated with the study of their specific polarization dependence as a function of frequency. By varying the polarization orientation as indicated in Figure 4.19, the optical far-field response function, such as the absorption cross-section and the scattering cross-section, can be finely tuned to be maximized at the high-frequency ROA resonance or at the low-frequency ROA resonance. The asymmetric L-shaped ROA shows a wavelength-dependent polarization property designed for bimodal wavelength behavior. As can be concluded from Figure 4.19, for the linear excitation polarization oriented 90° with respect to the Cartesian coordinate system, both bimodal ROA resonances can be excited for the absorption as well as for the linear scattering events. By hitting the internal symmetry main axis of the asymmetric L-shaped ROA, which is close to the 30°or 120°, polarization with respect to the x-axis, either the high-frequency ROA mode or the low-frequency ROA mode can be selectively addressed.

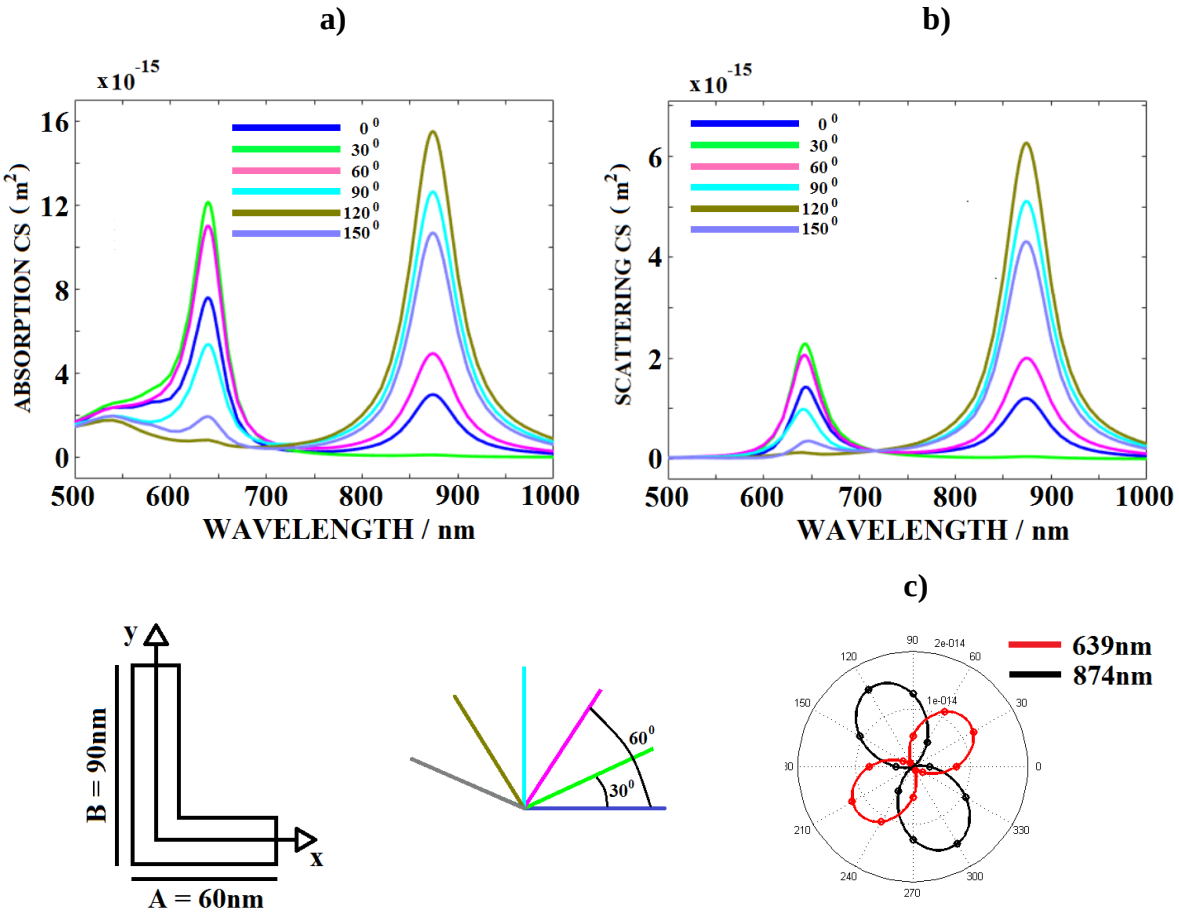

Figure 4.19: Electromagnetic plane wave excitation dependence of the scattering and absorption cross-section as a function of linear polarization change for an asymmetric L-shaped ROA with arm length A = 60 nm and B = 90 nm; a) absorption cross-section with a set of varying linearly polarized plane waves; b) scattering cross section with a set of varying linearly polarized plane waves; c) absorption polar diagram of the two asymmetric L-shaped ROA longitudinal resonances for wavelengths 639 nm and 874 nm.

After checking these values of polarization angles on several L-shaped antennas, we can say that these specific light polarization states match the effective dipole orientation angles α of the two resonances for the asymmetric L-shaped ROA which the analytical relations can approximate:

$$\alpha_{HIGH\_FREQUENCY} = arctg\left[\frac{A-\frac{W}{2}}{B-\frac{W}{2}}\right] \tag{4.2}$$

$$\alpha_{LOW\_FREQUENCY} = \frac{\pi}{2} + arctg\left[\frac{A-\frac{W}{2}}{B-\frac{W}{2}}\right] \tag{4.3}$$

Assuming an analytically single current mode for those resonances. Therefore, we neglect the influence of the finite width of the ROA arms. These equations (4.2) and (4.3) are derived from the geometry sketched in Figure 4.20. When the polarization orientation angle is $\alpha_{,HIGH\_FREQUENCY}$ the electric field is polarized along the blue line in Figure 4.20, while it is polarized along the green line for a polarization orientation angle $\alpha_{LOW\_FREQUENCY}$.

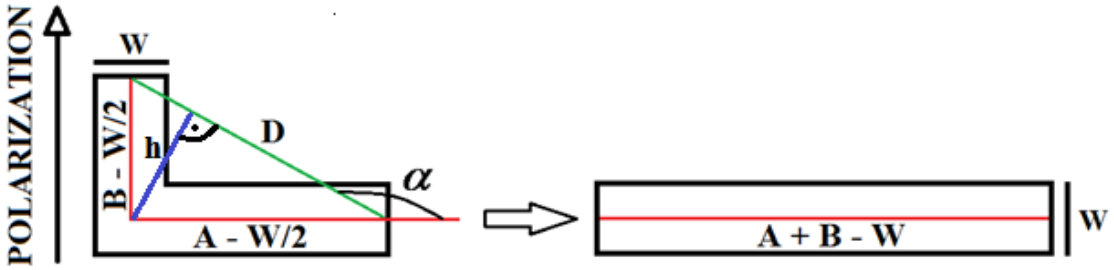

Figure 4.20: Representation of the rod-like antenna and L-shaped antenna with the same effective length (or the same volume).

For our investigation, the only relevant geometric parameter is arms length since, according to the Mie theory, the scattering cross section is a function of the volume of the metallic nanoparticles. If we keep ROA width and height constant ($W = 20nm, \quad H = 30nm$), the only relevant parameter for volume is effective length. As indicated in Figure 4.20, for an L-shaped antenna that has antenna arms lengths A and B, an appropriate rod with equal volume has an effective length $L = A + B - W$. Equation (4.1) is the result of our approximation that the red line stands for a virtual single electron path for the electrons that travel from end to end of the nanoparticle and represent a longitudinal mode.

To investigate this behavior deeply, we chose a rod-like ROA with a length of 100nm and simulate a new set of ROAs to investigate the scattering properties of several L-shaped antennas with the same volume. According to the equation $L = A + B - W$ and values $L = 100nm, W = 20nm$, the sum of the L-shaped antenna's arm lengths needs to be $A + B = 120nm$. For several L-shaped antennas whose arms fulfill this condition, we calculate the scattering response for the case of polarization in the y-direction, shown in Figure 4.20. The results are shown in Figure 4.21.

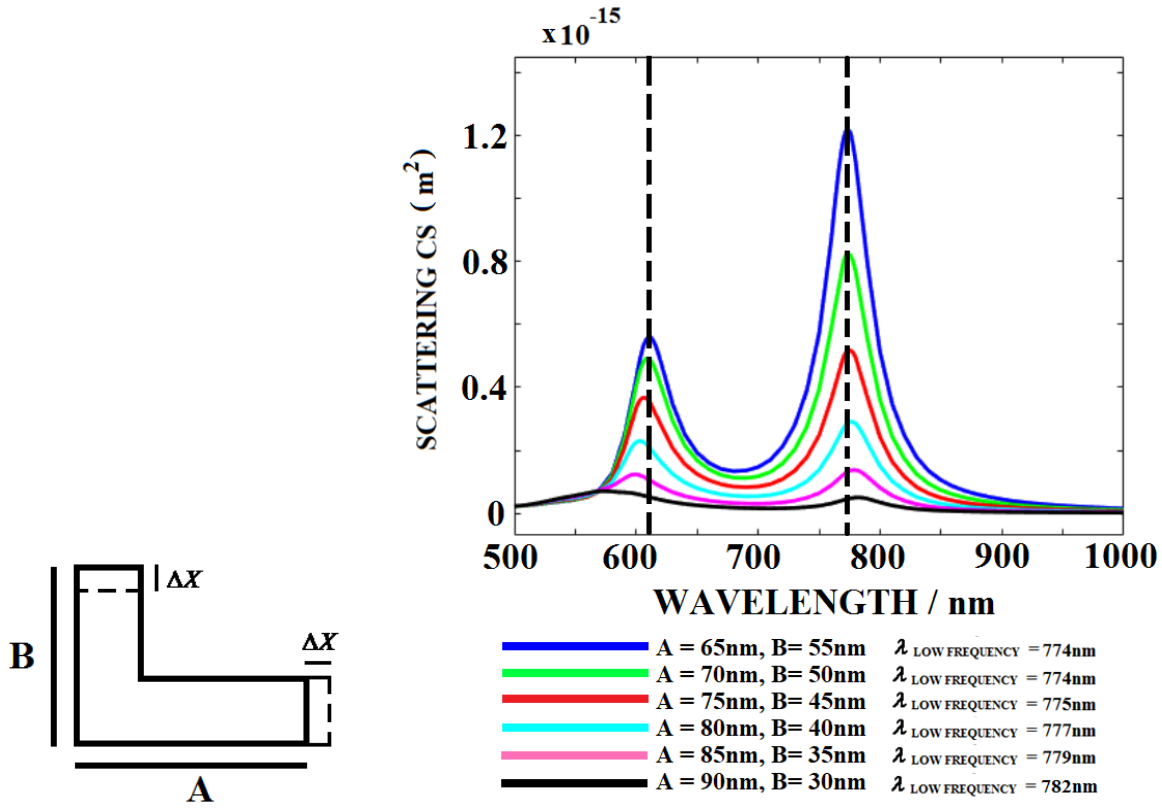

Figure 4.21: a) Representation of the arm length modification; b) far-field scattering properties (scattering cross section) of single L-shaped ROAs with the same effective length and different asymmetries. D is diagonal, as shown in Figure 4.20.

As shown in this figure, shortening ROA's arm B and increasing ROA's arm A leads to a shift of the high-energy ROA's resonance to the high-energy side. On the other hand, we also observe a shift of the low-energy ROA resonance to the low-energy side of the spectral bandwidth (the exact data for D and $\lambda_{LOW\_FREQUENCY}$ are given in Figure 4.21, and the behavior of the high-frequency resonant peak wavelength is shown in Figure 4.22).

Upon closely examining the triangle in Figure 4.20, we find that the combined lengths of the catheti (highlighted in red) remain constant across all simulation steps, whereas the hypotenuse length (highlighted in green) varies. When the cathetus lengths are the same ($A = B = 60nm$), hypotenuse D has a minimum value. In the following simulation steps, hypotenuse length D increases. It is noticeable that, besides the fact that resonance depends on nanoparticle effective length, the low energy mode wavelength also depends on the diagonal length (or angle α in Figure 4.20). Data show that diagonal D is proportional to restoring force that goes into the plasmon resonance shifting.

Alongside previous observations, we also want to find equations that can describe the correlation between effective length ($l_{EFF} = A + B - W$) and low energy resonant wavelength ($\lambda_{LOW\_FREQUENCY}$). This equation is also, to some degree, determined by the angle α or diagonal D. This is the reason why we are not able to express an equation that could obtain both variables l_{EFF} and α, but we can show it from some particular angles. Tables 4.2, 4.3, and 4.4 show results for angles from Figure 4.20 equal to 120°, 135° and 150°, respectively.

Table 4.2: Resonant wavelength of the second (low energy) resonance for the certain effective length (l_{EFF}) and for angle α from Figure 4.20 equal 120°

$\alpha(°)$	A(nm)	B(nm)	l_{EFF}(nm)	$\lambda_{HIGH\ FREQUENCY}(nm)$	$\lambda_{LOW\ FREQUENCY}(nm)$
120	30	44.64	54.64	**576**	**624**
120	35	53.30	68.30	**583**	**665**
120	40	61.96	81.96	**591**	**712**
120	45	70.62	95.62	**603**	**761**
120	50	79.28	109.28	**617**	**807**
120	55	87.94	122.94	**634**	**852**
120	60	96.60	136.60	**652**	**895**
120	65	105.26	150.26	**668**	**935**
120	70	113.92	163.92	**688**	**975**
120	75	122.58	177.58	**706**	**1011**
120	80	131.23	191.23	**731**	**1044**

Table 4.3: Resonant wavelength of the second (low energy) resonance for the certain effective length (l_{EFF}) and for angle α from Figure 4.20 equal 135°

$\alpha(°)$	A(nm)	B(nm)	l_{EFF}(nm)	$\lambda_{HIGH\ FREQUENCY}(nm)$	$\lambda_{LOW\ FREQUENCY}(nm)$
135	45	45	70	**587**	**668**
135	50	50	80	**593**	**704**
135	55	55	90	**601**	**739**
135	60	60	100	**611**	**774**
135	65	65	110	**622**	**809**
135	70	70	120	**634**	**841**
135	75	75	130	**647**	**875**

135	80	80	140	**660**	**904**
135	85	85	150	**674**	**933**
135	90	90	160	**689**	**963**
135	95	95	170	**705**	**994**
135	100	100	180	**720**	**1017**

Table 4.4: Resonant wavelength of the second (low energy) resonance for the certain effective length (l_{EFF}) and for angle α from Figure 4.20 equal 150°

$\alpha(°)$	A(nm)	B(nm)	l_{EFF}(nm)	$\lambda_{HIGH\ FREQUENCY}(nm)$	$\lambda_{LOW\ FREQUENCY}(nm)$
150	50	33.09	63.09	**580**	**649**
150	55	35.98	70.98	**584**	**674**
150	60	38.87	78.87	**589**	**702**
150	65	41.75	86.75	**595**	**728**
150	70	44.64	94.64	**602**	**757**
150	75	47.53	102.53	**610**	**783**
150	80	50.41	110.41	**620**	**811**
150	85	53.30	118.30	**630**	**837**
150	90	56.19	126.19	**641**	**862**
150	95	59.07	134.07	**648**	**888**
150	100	61.96	141.96	**659**	**911**
150	105	64.85	149.85	**670**	**934**
150	110	67.73	157.73	**681**	**957**
150	115	70.62	165.62	**694**	**980**
150	120	73.51	173.51	**706**	**1001**

From these tables, we can extract useful formulas for low- and high-frequency resonant wavelengths for each of the three angles mentioned above. As can be seen in formulas 4.4, 4.5, 4.6, and also in Figure 4.22 a), the dependency between low-energy resonant wavelength and the effective length of the L-shaped ROA is almost linear. For all three angles of α coefficients in the equations remain almost stable. We can also extract equations of dependency between the high energy resonant wavelength and the effective length of the L-shaped ROA. As shown

in equations 4.7, 4.8, 4.9, and Figure 4.22 b) for high-energy resonance, that dependency is parabolic.

1) $\lambda_{LOW\ FREQUENCY} = 3.134 \cdot l_{EFF} + 458.4[nm], \quad \alpha = 120^0$ (4.4)

2) $\lambda_{LOW\ FREQUENCY} = 3.193 \cdot l_{EFF} + 452.7[nm], \quad \alpha = 135^0$ (4.5)

3) $\lambda_{LOW\ FREQUENCY} = 3.225 \cdot l_{EFF} + 450.1[nm], \quad \alpha = 150^0$ (4.6)

1) $\lambda_{HIGH\ FREQUENCY} = 0.0042 \cdot l_{EFF}^2/[nm] + 0.113 \cdot l_{EFF} + 555.5[nm], \quad \alpha = 120^0$ (4.7)

2) $\lambda_{HIGH\ FREQUENCY} = 0.0044 \cdot l_{EFF}^2/[nm] + 0.131 \cdot l_{EFF} + 554.7[nm], \quad \alpha = 135^0$ (4.8)

3) $\lambda_{HIGH\ FREQUENCY} = 0.0045 \cdot l_{EFF}^2/[nm] + 0.101 \cdot l_{EFF} + 553.9[nm], \quad \alpha = 150^0$ (4.9)

a)

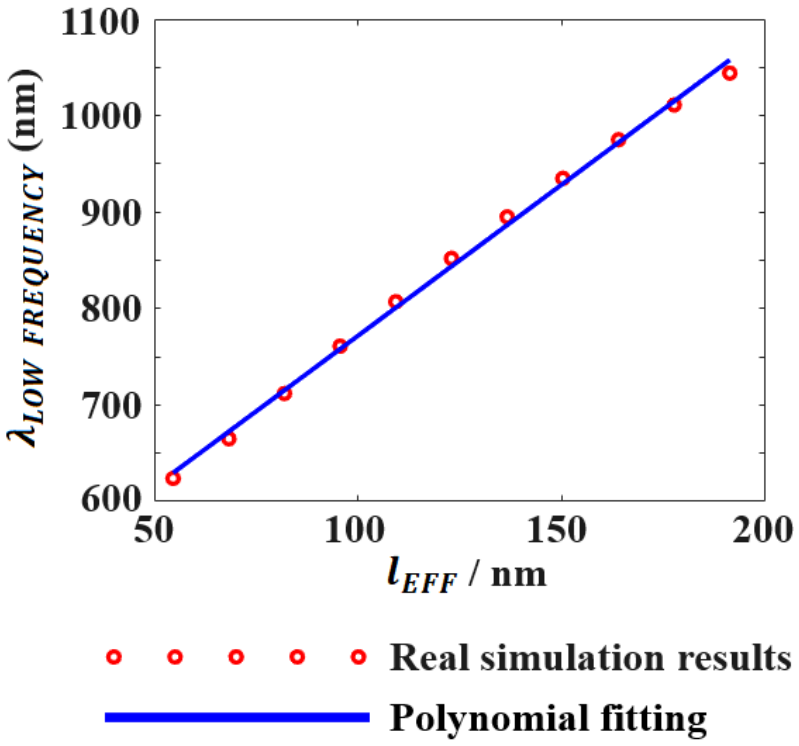

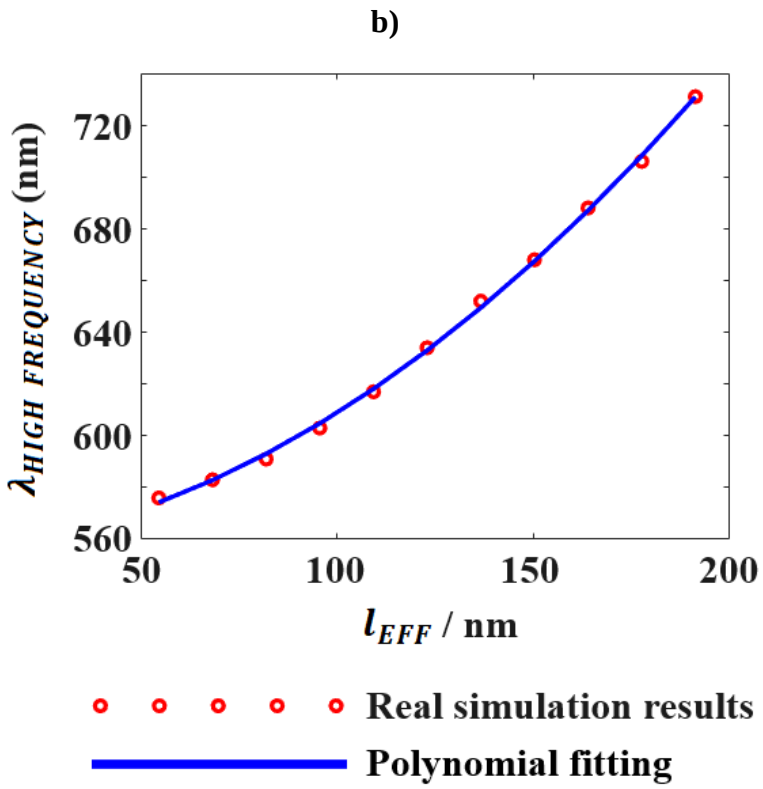

Figure 4.22: a) Dependency between the effective length of the L-shaped ROA (l_{EFF}) and the wavelength of low energy resonance for angle $\alpha = 120^0$ from Figure 4.20; b) dependency between the effective length of the L-shaped ROA (l_{EFF}) and the wavelength of high energy resonance for angle $\alpha = 120^0$ from Figure 4.20. In both cases are presented real values (circles) and polynomial fitting curves.

These equations could be important because they describe low-energy ROA resonance tuning only by changing the shape, not the volume. Of course, these equations are valid only for L-shaped antennas with given constant values, $W = 20nm$ and $H = 30nm$. For our approximation, the red line in Figure 4.20 defines the effective length of the L-shaped nanoparticle.

Now, we discuss high-energy mode ROA resonance. From Figure 4.21, it can be seen that the wavelength of the higher energy mode is more affected by diagonal cap D or angle alpha than the wavelength of the lower energy mode. Figure 4.20 shows the dependence between h, α and high energy mode peak wavelength ($\lambda_{HIGH\ FREQUENCY}$). Length h is the height of the triangle, which is already shown in Figure 4.20 (blue line). When $\alpha = 180°$, it is a pure rod. When $\alpha = 135°$, it is an L-shaped antenna with the same arm lengths ($A = B = 60nm$).

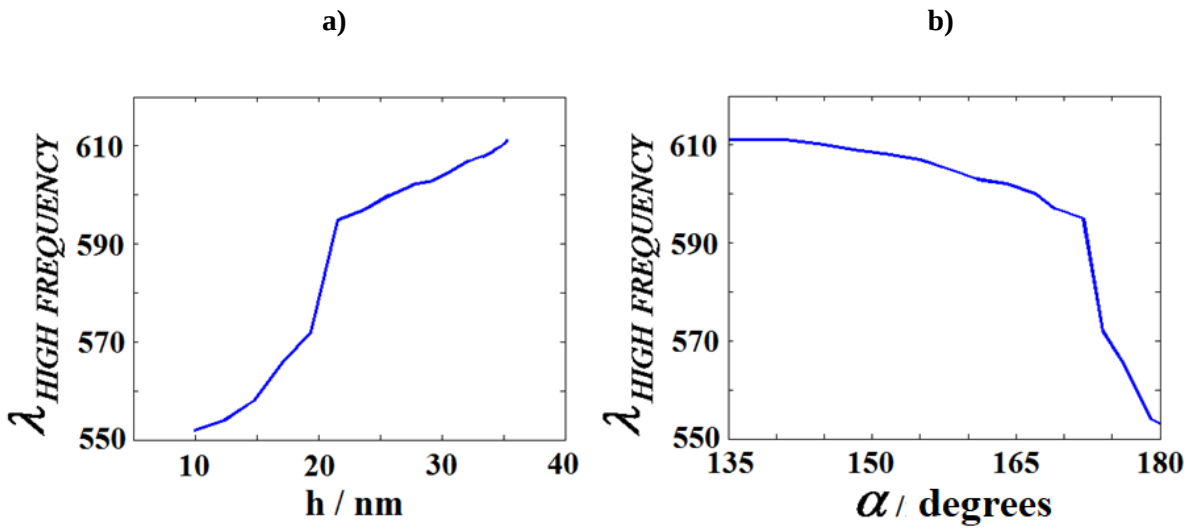

Figure 4.23: Relation between high energy mode wavelength and: a) height of the single L-shaped ROAs (see Figure 4.20); b) angle $\boldsymbol{\alpha}$ of single L-shaped ROAs (see Figure 4.20).

Figure 4.23 proves that high energy resonance wavelength is influenced by height h or angle α, as shown in Figure 4.20. That influence is evident in the angles $\alpha \in (170^0 - 180^0)$. In this angle range, the arm B of the L-shaped antenna becomes short, and therefore, the height h is very short also.

4.4.1 Bimodal coupled L-shaped antennas

Coupling the resonant optical and near-IR antennas is a method for localizing the field in small volumes beyond the diffraction limit. This behavior is very useful for coupling with quantum emitters, and it has also been profoundly investigated for several other properties [16, 17, 18]. Coupled bimodal structures have been discussed previously [37, 38, 39]**.** While we've discussed coupled rod-shaped antennas, it's important to note that they function in only one mode. Coupled L-shaped ROAs comprise two separate L-shaped nanoparticles with a nanometer-scale gap between them. We also depend on earlier studies of single L-shaped ROAs to inform our understanding of geometric modifications, field and current line distributions, and polarization sensitivity. Here, observing whether we can exhibit two resonances in the gap as a near-field response is crucial. There are several options for creating this coupled system, but we will use just two, as shown in Figure 4.24. As can be seen, the simulation set starts from a classical dipole rod-like antenna.

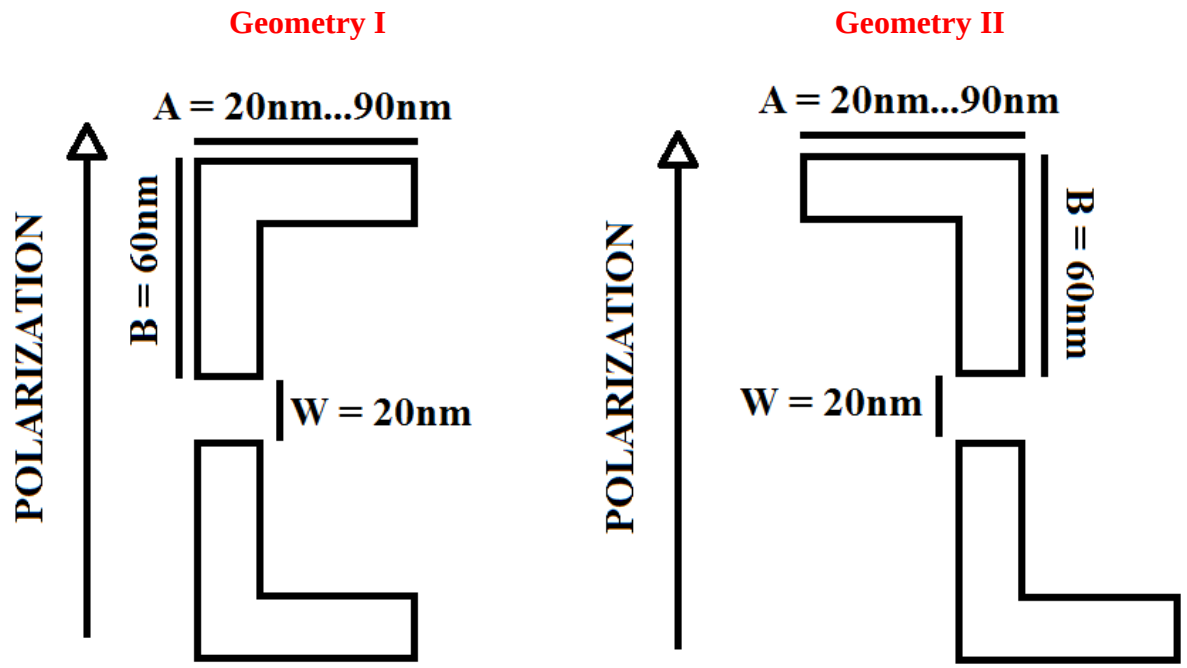

Figure 4.24: Representation of the arm L-shaped antenna coupling geometries I and II. B is kept at a constant 60nm, and A varied between 20nm and 90nm for both nanoparticles in the same direction for geometry I and in the opposite direction for geometry II.

Then, that dipole rod-like antenna is modified by adding metal on both sides in every simulation step. Of course, this addition of metal can be in the same direction (type **I**) or the opposite direction (type **II**). We use both methods to see which coupling is more efficient. All geometrical parameters are the same. With those antennas, we exhibit and control two resonances in the gap. In this set of simulations, we do not change the polarization direction. As can be seen in Figure 4.24, the polarization direction is along the rods that are directly coupled. By analyzing Figure 4.25, we can conclude that near-field and far-field properties have the same nature for both types of coupled L-shaped geometries.

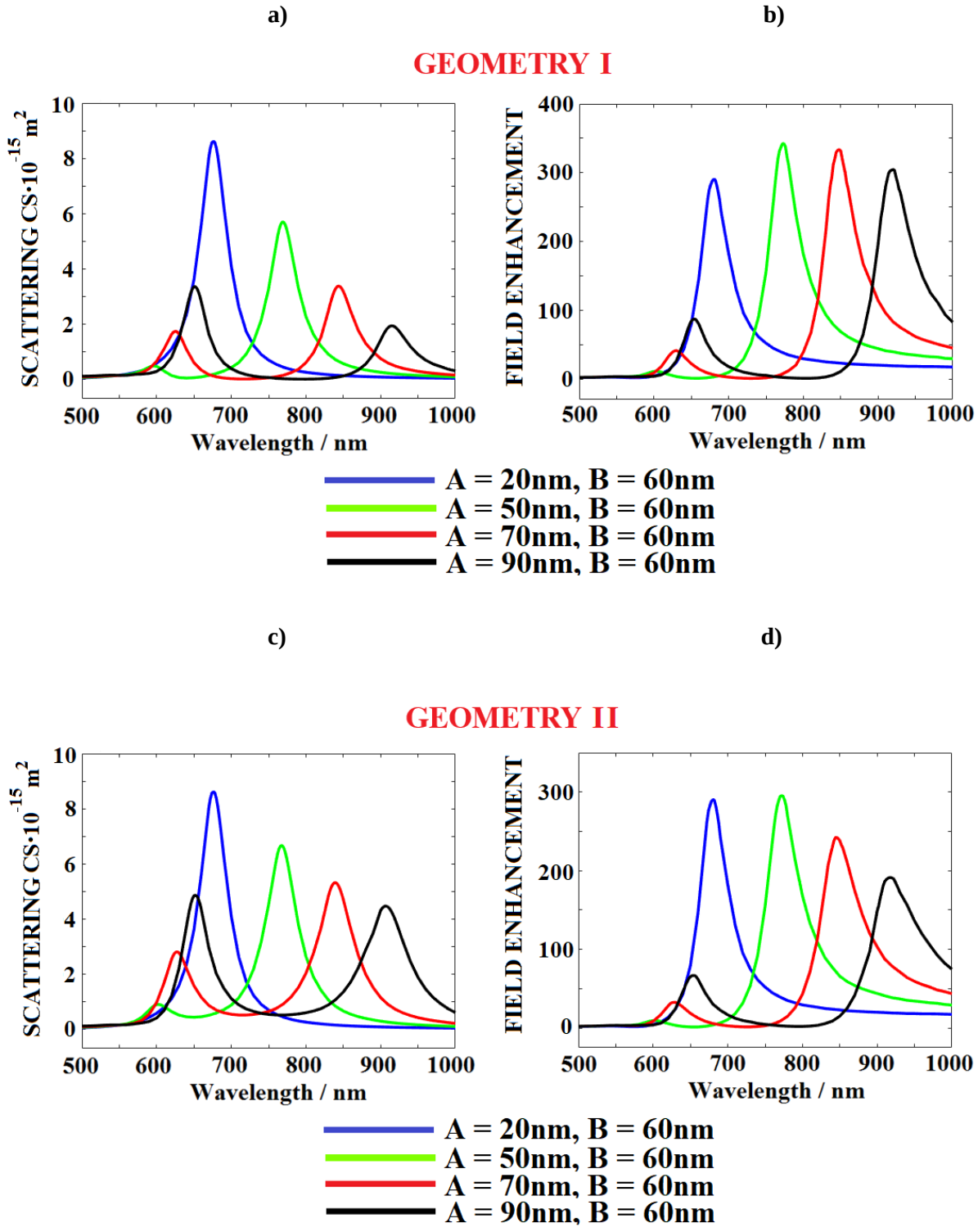

Figure 4.25: a) Absolute scattering cross-section of ROA for geometry I from Figure 4.24; b) field enhancement in the gap center of ROA for geometry I from Figure 4.24; c) absolute scattering cross-section of ROA for geometry II from Figure 4.24; d) field enhancement in the gap center of ROA for geometry II from Figure 4.24. Field enhancement here is $|\boldsymbol{E_{TOT}}|^2/|\boldsymbol{E_{IN}}|^2$.

For geometry type I, there is a stronger field enhancement in the middle of the gap. Figures 4.26 and 4.27 show near-field and current density distributions for high-energy and low-energy modes. We have chosen geometry type II for this purpose.

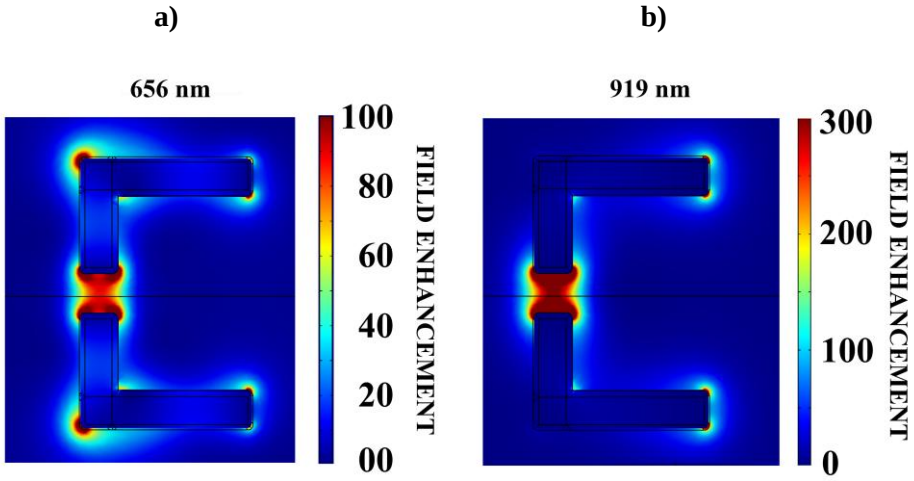

Figure 4.26: Near field distribution of the field intensity enhancement. The arm lengths are A=60nm and B = 90 nm. The resonance wavelengths are: a) 656 nm and b) 919 nm. The field distribution is plotted in the middle of the antenna height. Color bar or field enhancement means $|E_{TOT}|^2/|E_{IN}|^2$.

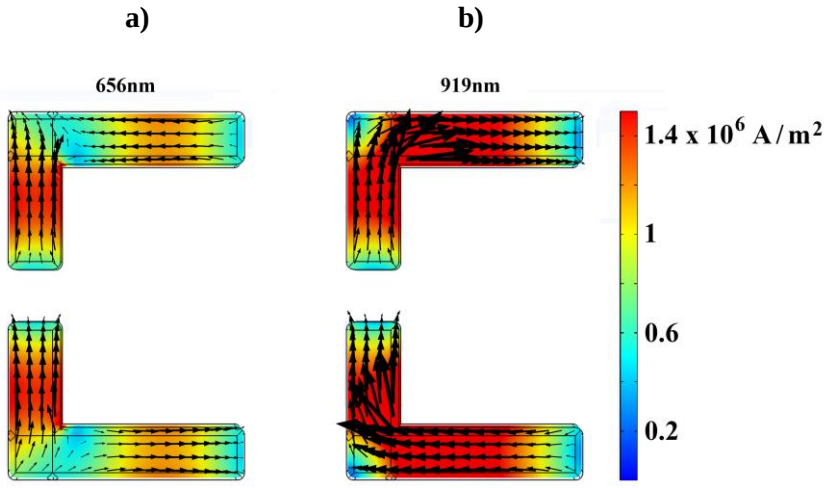

Figure 4.27: Current density of the bimodal coupled L ROA resonances. Arm lengths are A = 90 nm and B = 60 nm. The color bar is J (current density) with the vector representation of the current modes for ROA configurations I and II, respectively. a) ROA resonance 656 nm, b) ROA resonance 919 nm.

After the preliminary coupling investigation, we will show the coupling behavior when the gap width is only 2 nm for the case of geometry I, where it is indicated that the coupling is stronger. Moreover, we will not change arm A but we will change arm B (the arm in the vertical direction). Figure 4.28 (a) shows the top view for the reported coupled L-shaped nanoantenna design. Figures 4.28 (b) and 4.28 (c) show near and far field properties. Even though the gap

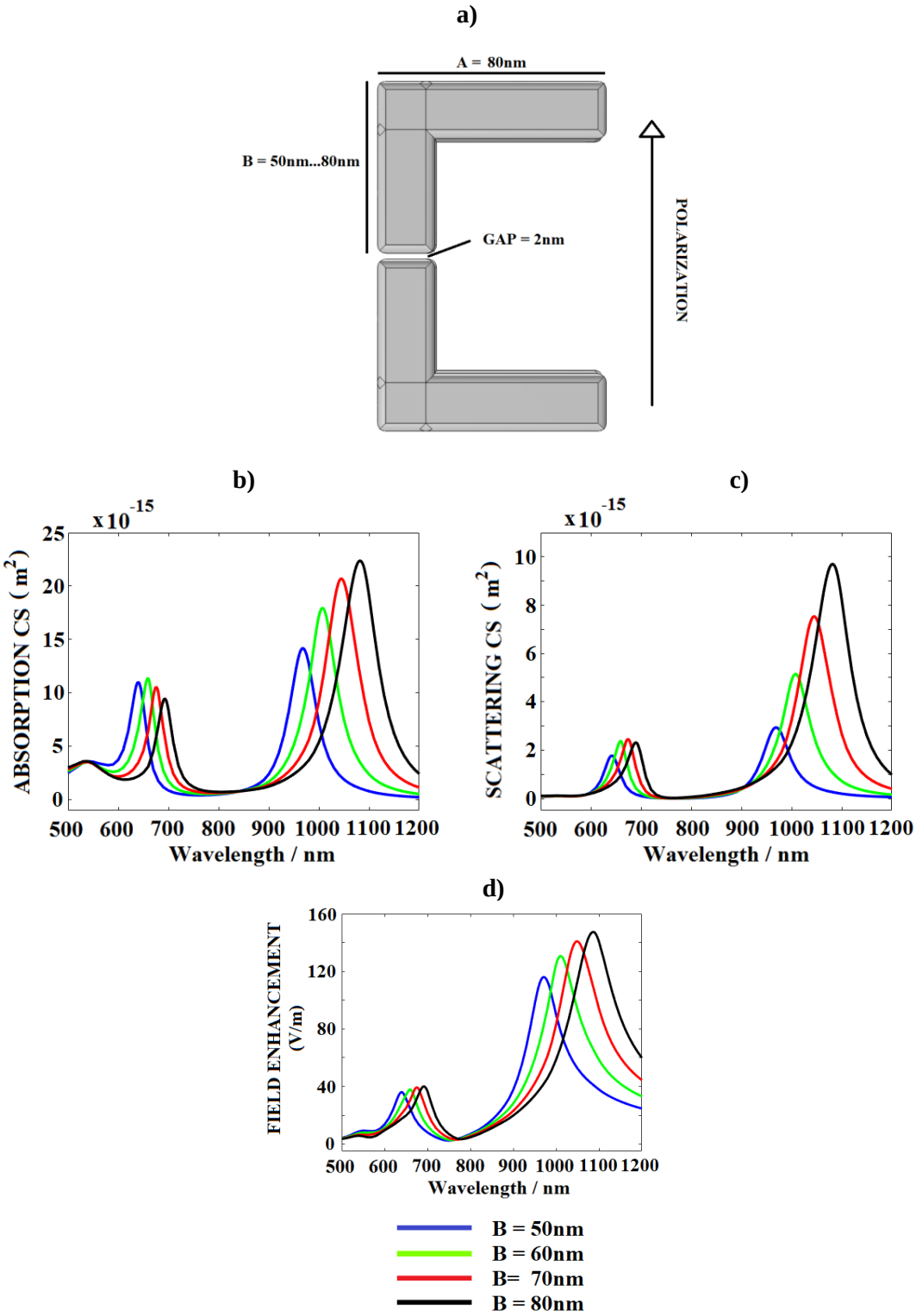

Figure 4.28: a) Top view of a coupled L-shaped ROA (x-y plane) with antenna arms termed A and B where B varies from 50 nm to 80 nm and A is kept constant at 80nm; b) and c) Absorption and scattering cross section; d) Field enhancement in the gap center at different values of B. Scale is $|E_{TOT}|/|E_{IN}|$.

is small, that does not change the nature of the similar absorption and scattering cross-section of coupled L-shaped nanoantenna and single L-shaped nanoantenna, as Figure 4.28 and Figure 4.17 show.

When the arm's length B increases, there is a red shift of low and high-energy resonances, and the second resonance amplitude increases. Figure 4.28 (d) displays the field enhancement for the coupled L-shaped design.

Due to the narrow gap in this investigation, step field enhancement will be much higher. Therefore, the scale for this analysis here will be $|E_{TOT}|/|E_{IN}|$ and not $|E_{TOT}|^2/|E_{IN}|^2$. By simulations, we want to estimate field enhancement in the center of the gap from Figure 4.28 (a) on a given scale $|E_{TOT}|/|E_{IN}|$. For the antenna arm lengths, A=60 nm and B=80 nm, the field enhancements in the gap are 40 and 147.3 for the high energy (692 nm) and low energy (1086 nm) resonance, respectively. As indicated in Figure 4.28 (c), an increment in arm's length B causes a smaller redshift of the high energy resonance and a more significant red shift of the low energy resonance. Also, in the case of high-energy resonance, there is no significant change in field enhancement. On the other hand, there is a considerable increase in field enhancement for low-energy resonance.

We conclude that the suggested design in Figure 4.28 (a) enables us to control field enhancement properties, especially for the low-energy resonance.

4.4.2 Discussion

If we analyze all solutions in terms of the vector representation of the current flow together with the amplitude of the current modes as depicted in Figure 4.18 for the two fundamental ROA resonance frequencies. We assume that a linear combination of two plasmon length basis functions is sufficient to reconstruct the eigenmodes of the asymmetric L-shaped ROAs. Therefore, we introduce a hypothetical hybridization model, as depicted in Figure 4.29. We start with the plasmon length of a short gold nano-bar with a dimension of 120 nm. The physical size/dimension of this single gold nanorod represents the base function of the independent plasmon length since the current oscillation at this longitudinal eigenfrequency is confined to the end-to-end phase condition. We simplify the particle dimension to a nanorod-like ROA with a constant particle width (thus, we keep the transversal particle resonance frequency constant) while increasing the longitudinal ROA length. Nanorods with a length of 120 nm

can be bent into the form of an L-shaped nanoparticle with arms 80nm and 60 nm. This corresponds to the effective length of this L-shaped nanoparticle as it already comprises the additional width of 20 nm (80 nm + 60 nm – 20 nm = 120 nm). Gold nanorod with a length of 120 nm has a longitudinal resonance eigenmode energy of 1.44 eV (corresponding to a wavelength of 862 nm), and the gold nanorod of length of 60 nm has a resonance at 1.88 eV (corresponding to a wavelength of 658 nm). Simultaneously, this L-shaped nanostructure with arm lengths 60nm and 80nm has high and low energy resonances at 634 nm and 843 nm with corresponding energies of 1.96 eV and 1.47 eV, respectively. These wavelengths correspond to 54 nm and 112 nm plasmon lengths, respectively. Asymmetric L-shaped ROAs can be constructed as linear combinations of two resonances. For further analysis, it is important to understand Figure 4.21, where resonant wavelengths are calculated for different combinations of arm lengths. In Table 4.5, we can see the high energy and low energy resonant wavelengths for different combinations of arms A and B of L-shaped ROA, all having the same effective length (A+B-W=120 nm). Figure 4.21 shows that while the length of the shorter arm decreases, the high energy resonance is shifting blue. The same behavior can be seen in Table 4.5, columns 2 and 5. This is strongly correlated with the abovementioned behavior from Figure 4.18, where it is pointed out that the highest current density amplitude is exclusively located at the shorter ROA arm of the L-shaped antenna, giving rise to the high energy resonance. Regarding the low-energy resonance, Table 4.5 (columns 3 and 6) shows that for a constant effective length of L-shaped antennas (120 nm in this case) and every combination of arms' lengths, the low-energy resonance remains almost stable, except for a small red-shift which is related to the change of the diagonal of the L-shaped nanostructure already analysed in Figure 4.20 and Figure 4.21. It can be seen from Figure 4.29 that the plasmon length of the L-shaped ROA defining the low energy eigenmode is shorter than the 120 nm individual gold nanorod, which has the same volume as the given L-shaped ROA. As Table 4.5, columns 6 and 8 show, the general conclusion is that there is always a small blue shifting of the low energy resonance of L-shaped ROA compared to the resonance of rod-shaped ROA, which has the same volume as this particular L-shaped ROA. In this case, that shifting is between 16nm and 21m. Also, in equations, we extracted formulas for linear dependency between the effective length of the L-shaped ROA (l_{EFF}) and the wavelength of low energy resonance.

On the other hand, we have found parabolic dependency between the effective length of the L-shaped ROA (l_{EFF}) and the wavelength of high energy resonance from Tables 4.2, 4.3, and 4.4.

The two fused ROA arms of this eigenmode solution are oscillating out-of-phase along each 'individual' arm of the L-shape with a well-pronounced current amplitude located at the short axis of this entity (Figure 4.18 and Figure 4.29).

This hybridization picture of plasmon length from individual longitudinal, unperturbed plasmon resonators finds analogies in the field of molecular orbital hybridization of binuclear atomic species A and B, where the hybridization eigenvalues of the symmetric and antisymmetric linear combinations give rise to highly polarized two-center-two-electron covalent bindings.

Table 4.5: Resonant wavelengths of different L-shaped and rod-shaped structures

1	2	3	4	5	6	7	8
A arm/ nm	B arm/nm	Diagonal of the "triangle" (red line in Figure 5)/nm	Height of the "triangle" (blue line in Figure 5)/nm	High energy resonant λ of L-shaped antenna with arms A and B/nm	Low energy resonant λ of L-shaped antenna with arms A and B/nm	Resonant λ of nanorod with length B/nm	Resonant λ of nanorod with length 120/nm
70	70	84.9	57.7	634	841	689	862
75	65	85.1	57.3	634	842	672	862
80	60	86	55.8	632	842	657	862
85	55	87.5	53.5	630	843	640	862
90	50	89.4	50.3	628	843	625	862
95	45	91.9	46.5	625	844	611	862
100	40	94.9	42.2	624	846	599	862

This analogy picture even holds for the symmetric L-shaped ROA (e.g., antenna arm A = 60 nm; B = 60 nm), where the eigenmode energy separation of plasmon length linear combination is symmetrically spread around the plasmon length basis function for the 60 nm gold nanorod (here, 1.88 eV). The design of multiple resonance optical antennas can benefit from the 'fused' plasmon length concept. Thus, broadband ROA devices with well defined tailored resonances

can be engineered by tuning the individual plasmon length of each contributing antenna arm. Furthermore, the polarization of the re-emitting light can be analyzed in terms of the effective internal dipole of the specific ROA resonance frequency. Therefore, mono-modal ROA resonance scattering and absorption can be accomplished even with a bi-modal asymmetric L-shaped ROA through the polarization control of the external linearly polarized excitation source.

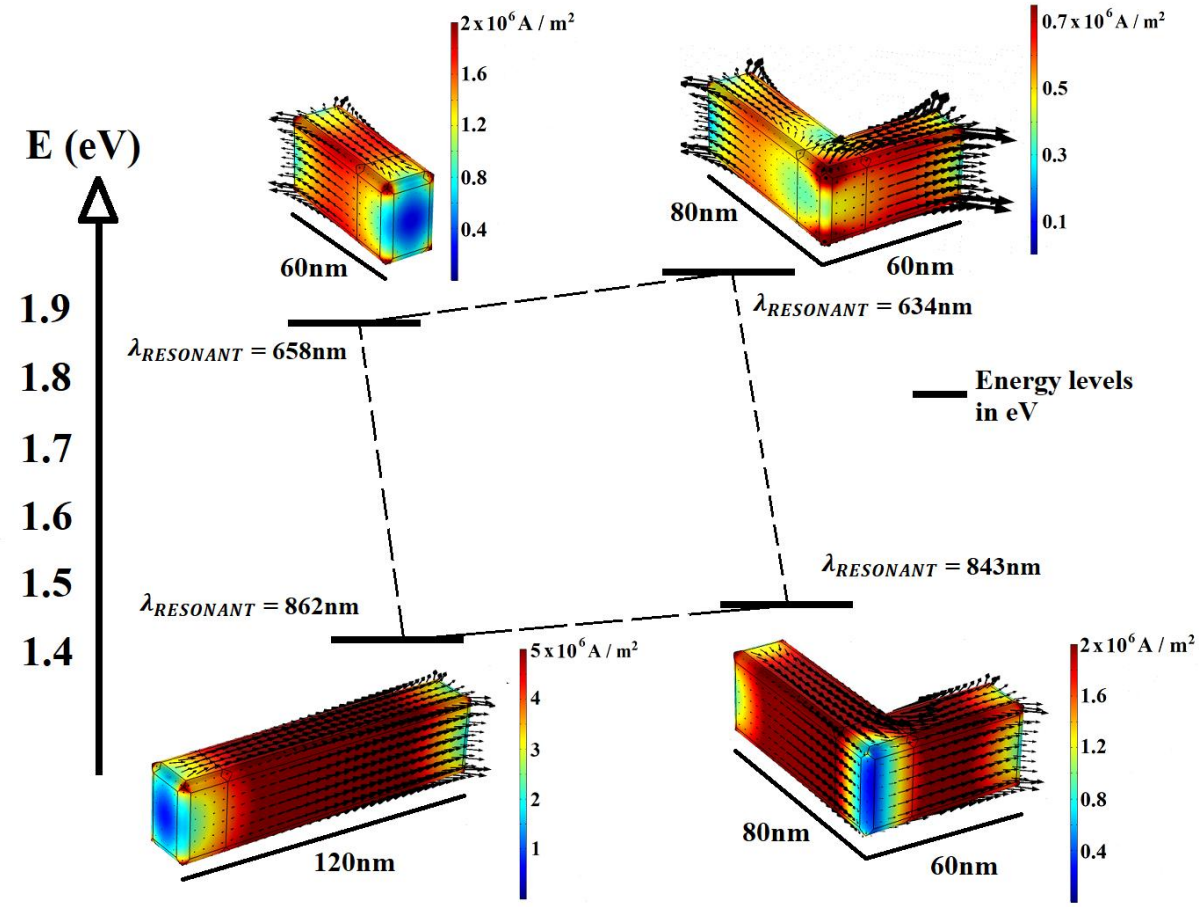

Figure 4.29: Fusing two different plasmon lengths (60 nm and 120 nm rod length with the ROA resonances at 658 nm and 862 nm, respectively) to construct the asymmetric L-shaped ROA longitudinal modes.

4.5 Bimodal single cross-shaped antennas

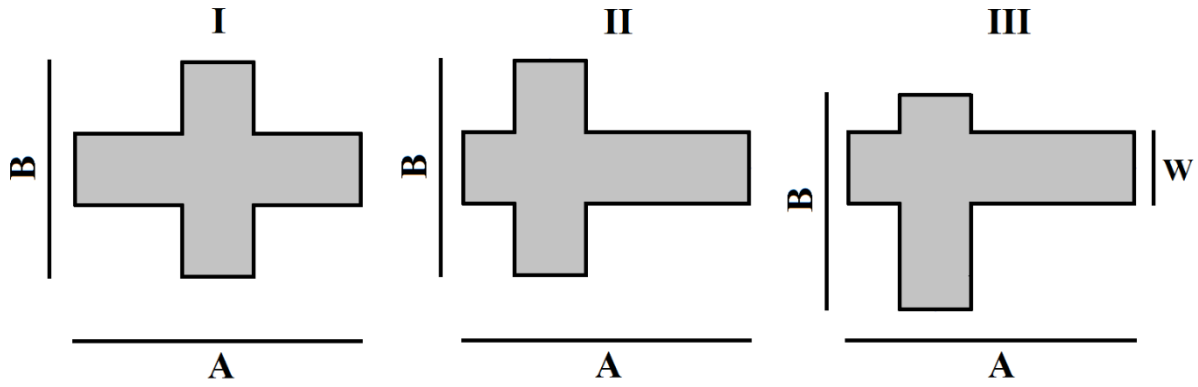

Figure 4.30: Top view of cross-shaped ROAs (x-y plane) with three types of symmetry levels. The antenna arms A and B and arm width W.

Figure 4.30 illustrates three general types of cross-shaped antennae regarding the symmetry with different arm lengths ($A \neq B$). For a more detailed investigation of cross-shaped antennas, we will first introduce some notations directly related to the level of symmetry.

I) A symmetric cross-shaped antenna is a cross-shaped antenna that has symmetry with respect to both vertical and horizontal axis.

II) A partially symmetric cross-shaped antenna is one that is symmetric with respect to the vertical or horizontal axis but not to both axes simultaneously.

III) An asymmetric cross-shaped antenna is symmetric with respect to neither the horizontal nor the vertical axis.

It is worth mentioning that the symmetry is not correlated with the overall arm lengths A and B. Cross-shaped nanostructures can exhibit an axis symmetry even if the arm lengths are different ($A \neq B$), but also can be asymmetric even if the arm lengths are equal ($A = B$).

4.5.1 Symmetric cross-shaped antenna

We now investigate in more detail the spectral properties of symmetric cross-shaped antennas. The analysis starts with the geometry from Figure 4.31.

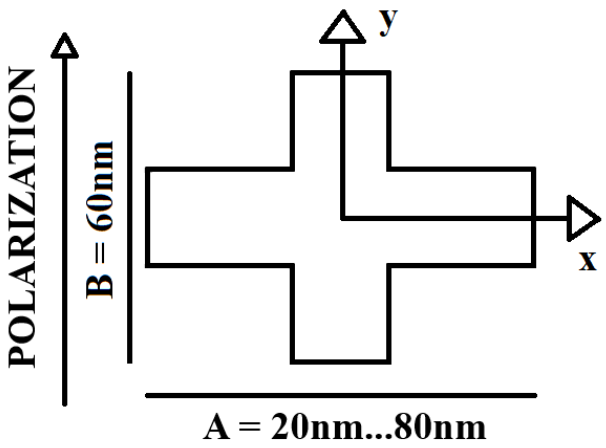

Figure 4.31: Top view of a single cross-shaped ROA (x-y plane) with the antenna arms termed A and B with respect to the linearly polarized plane wave excitation

As shown in Figure 4.31, the arm length A varies in our simulations from 20 nm to 80 nm in steps of 10 nm while B is held constant at 60nm. In the first step of the investigation, when A is 20 nm, the geometry is a single rod with a length B=60 nm. In all cases, the symmetry vs. both axes is maintained. The polarization direction is parallel to the y-axis, as indicated in Figure 4.31.

When we analyze the results in Figure 4.32, there is a slight blue shift of the resonant wavelength for $A = 20\ nm$, $A = 30\ nm$ and $A = 40\ nm$ (due to perturbed charge oscillation in the y-direction compared with the pure single rod). This effect saturates as a further increase of length A ($A = 50\ nm,\ 60\ nm \ldots$) does not lead to a further blue shift.

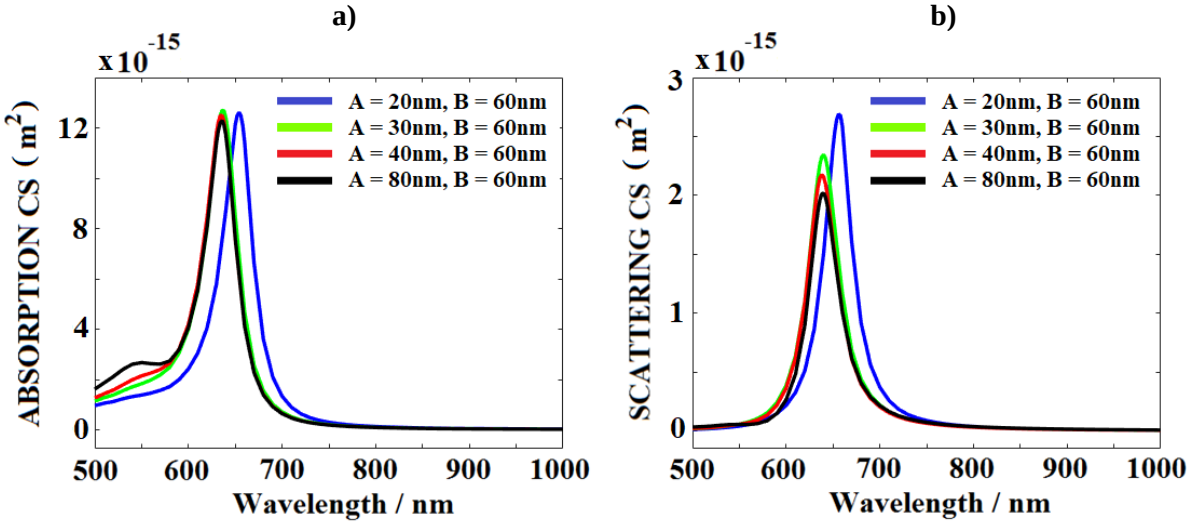

Figure 4.32: Far field optical properties of symmetric cross-shaped ROAs with increasing arm length. a) Absolute absorption cross-section; b) absolute scattering cross-section.

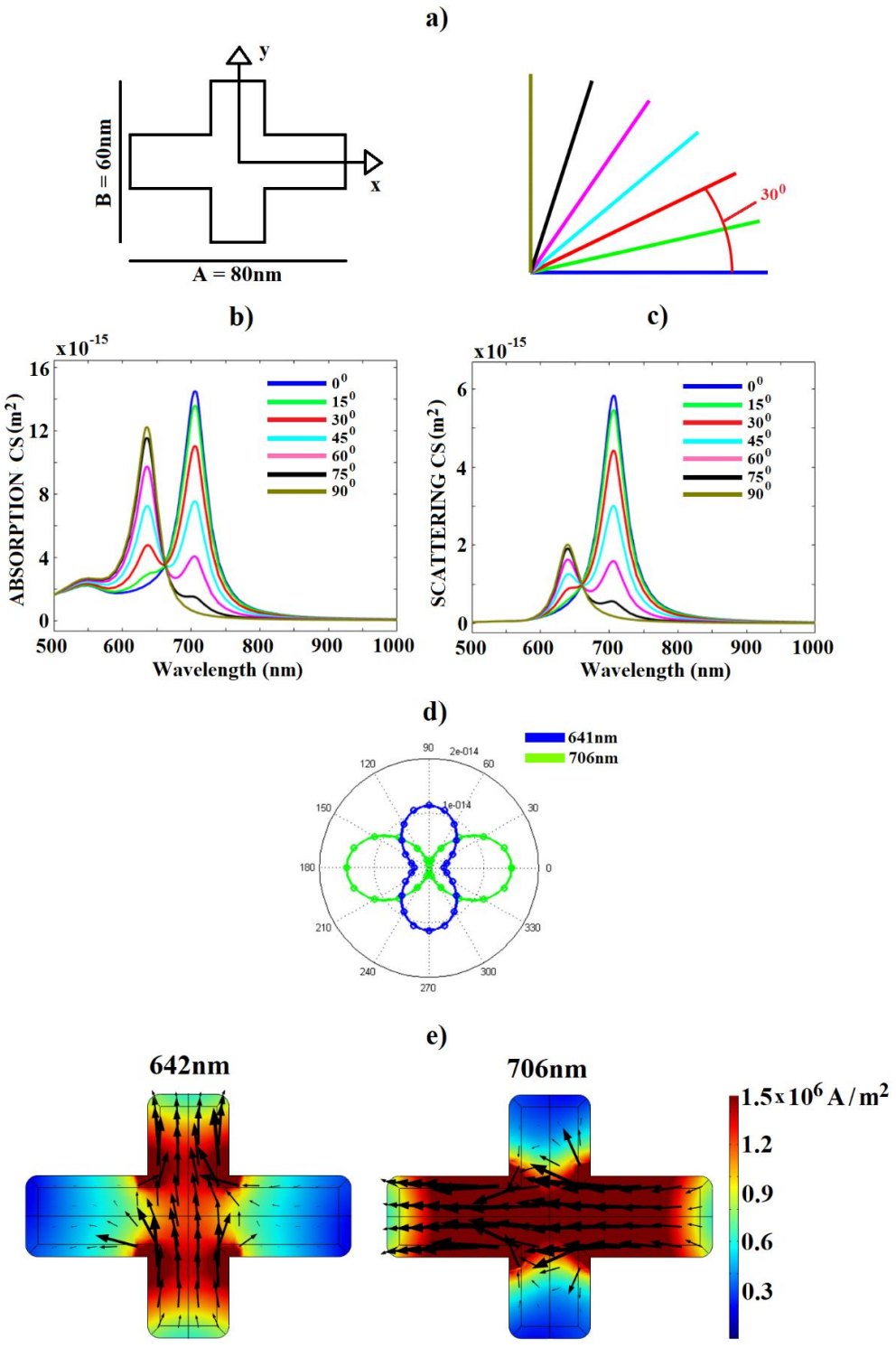

Figure 4.33: Electromagnetic plane wave excitation dependence of the scattering and absorption cross-section as a function of the polarization angle of the linearly polarized light for a symmetric cross-shaped ROA with arm lengths A = 60 nm and B = 80 nm. a) 2D schematic of the ROA and polarization directions; b) absorption cross-sections for different polarizations; c) Scattering cross-section for different polarizations; d) Polar diagram of the two longitudinal resonances; e) current densities of two ROA resonances at wavelengths 642 nm and 706 nm.

Now, we examine the polarization sensitivity of symmetric cross-shaped antennas. As shown in Figure 4.33, the cross-shaped ROA has arm lengths of 60 nm and 80 nm. It can be seen from this figure that a monomodal behavior for polarization angles 0° and 90° is observed. Bimodal behavior develops for other polarization angles, most pronounced at 45°. Figure 4.33 presents the current density distribution for the high- and low-energy modes, which are excited with a polarization angle of 45°. As mentioned, the cross-shaped antenna can be observed as a combination of two rods with lengths of 60 nm and 80 nm. Every one of those rods has its own resonant behavior. At the same time, it is already shown in the previous investigation in Figure 4.9 that the rod-shaped antenna is very polarization-sensitive and that the strongest spectral response appears when the polarization direction is along the longitudinal axis of the rod. Therefore, for some polarization angles, the shorter rod is dominant. For some other angles, a longer rod is dominant. As seen, for a polarization angle of 45°, the dominance of shorter and longer rods is equal.

4.5.2 Partially symmetric cross-shaped antenna

We now turn to the investigation of partially symmetric cross-shaped antennas. This investigation starts with single symmetric (Type I from Figure 4.30) cross-shaped antennas with the same arm lengths (A=B=80 nm) as in Figure 4.34. If we accept the coordinate system from Figure 4.34, the $\vec{k}$ vector of the plane wave is parallel to the z-axis, and the $\vec{E}$ vector lies in the xy plane.

We need to break the symmetry of a symmetric structure to get a partially symmetric structure. There are several ways to break the symmetry and to set polarization conditions. Still, there will be chosen symmetric cross-shaped ROA with equal arms A and B of 80 nm, and then only the arm with length B will be displaced in horizontal or x direction, as shown in Figure 4.34. In this way, the partial symmetry of the structure stays because ROA will keep the symmetry with respect to the vertical or y-axis. If we look at the symmetric definitions in Figure 4.30, we see that this corresponds to a transition from Type I to Type II. We will use the structure in Figure 4.34 a) to analyze far-field properties. Figure 4.34 b) shows the 3D model in COMSOL Multiphysics.

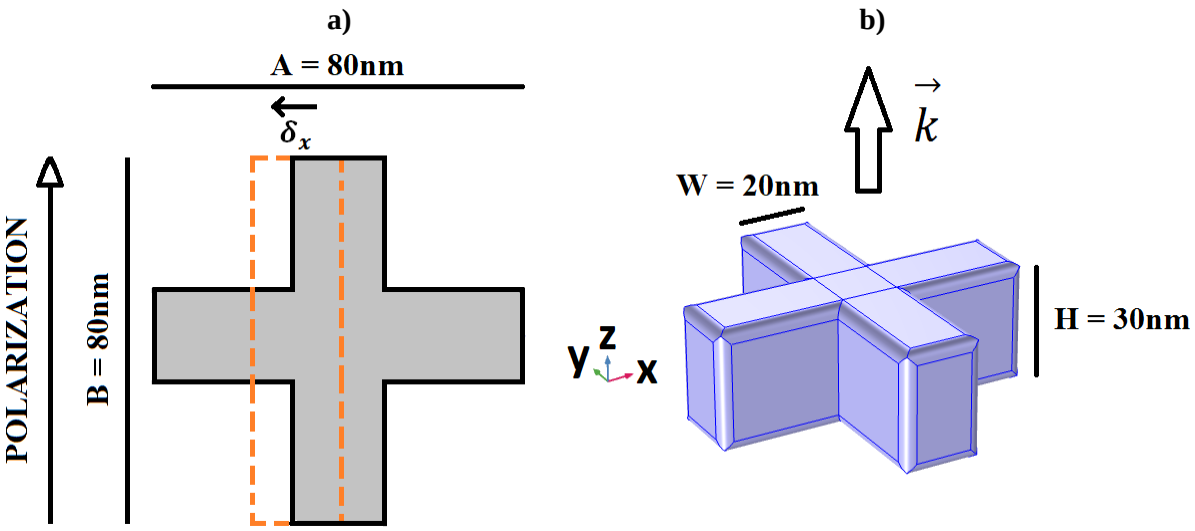

Figure 4.34. (a) Top view of a single partially symmetric cross-shaped ROA (x-y plane) with the antenna arms A and B; b) 3D model of the single cross-shaped partially symmetric ROA

In this chapter about cross-shaped ROAs, the displacements δ_x and δ_y will be used to control the movement of the rectangular element from its original central position, lowering the symmetry. As can be seen in Figure 4.34 a), in this first step of the investigation, the only relevant displacement value is δ_x as the vertical arm is moved only along the x-axis. As indicated in the same figure, the polarization direction is vertical.

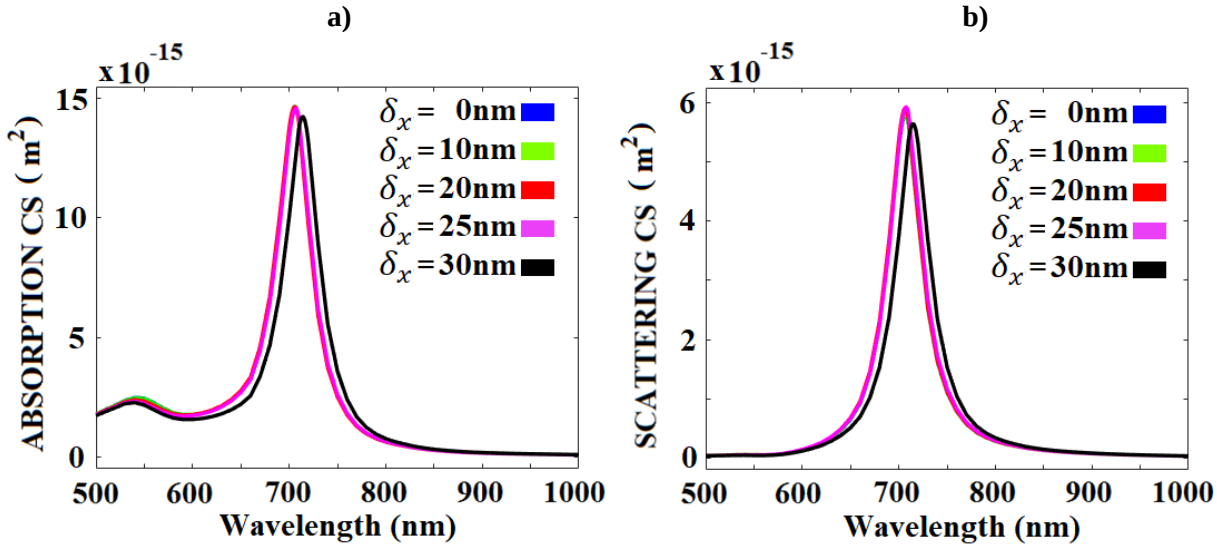

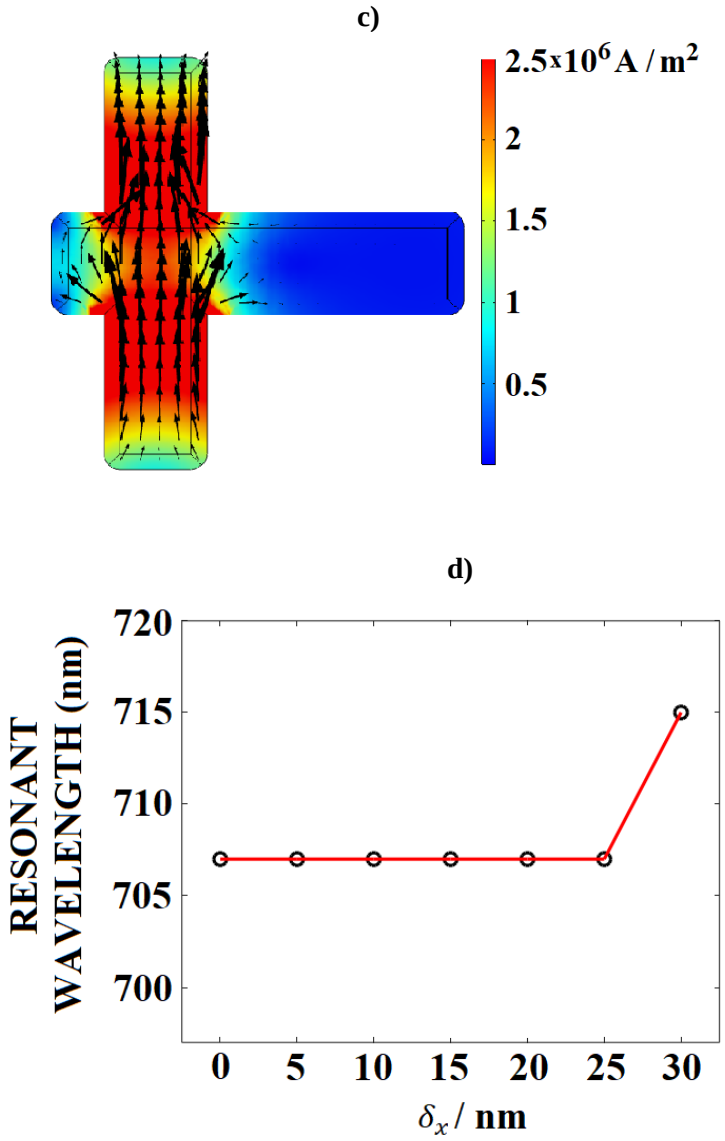

Figure 4.35. (a) Absolute absorption cross sections; (b) absolute scattering cross sections; (c) current density of a partially symmetric ROA at wavelength 707 nm and $\delta_x = 25\ nm$; (d) The dependency between δ_x and resonant wavelength for the partially symmetric cross-shaped antenna.

As Figure 4.35 a) and b) show, this cross-shaped single ROA is analyzed in terms of its scattering and absorption properties by "morphing" the antenna from a symmetric-shaped antenna to a partially symmetric cross-shaped antenna (Type II) by shifting the vertical arm B by δ_x=5 nm in the horizontal direction for each simulation step.

As shown in the previous investigation of symmetric cross-shaped ROA, we increased horizontal arm A. Here, the volume and antenna arm lengths are kept constant. As Figure 4.35 shows, behavior is monomodal, and there is almost no resonance shifting for the smaller values of the δ_x. Based on these results, we can make an important conclusion. If the polarization

direction is set along the symmetric arm of the partially symmetric cross-shaped antenna (in this case, the vertical arm), the antenna exhibits just one resonance, which is almost independent of the horizontal rod. Figure 4.35 a) and b) clearly show that for lower values of δ_x the resonant wavelength is almost constant, but for $\delta_x = 30$ nm small red-shifting of the resonant wavelength occurs since then the cross-shaped antenna becomes T-shaped and this causes a redistribution of the mode energy. Furthermore, Figure 4.35 c) shows the current density with current density lines of the partially symmetric ROA at a wavelength of 707 nm for the shift value of $\delta_x = 25$ nm. It can be seen from this figure that the nanoantenna shows monomodal behavior and mainly depends on the current distribution in the y-direction with small perturbations of current lines. Figure 4.35 d) presents the dependency of the resonant wavelength on the displacement δ_x. It can be seen from this figure that, for the small values of δ_x, the resonant wavelengths remain the same at 707 nm. While at δ_x=30 nm, the cross-shaped antenna is T-shaped, as seen in Figure 4.35 a), and the resonant wavelength is slightly shifted to 715 nm.

4.5.3 Asymmetric cross-shaped antennas

As had been explained for partially symmetric cross-shaped ROAs, there are more ways to break cross-shaped ROA symmetry. Here, we choose again the way not to change ROA's volume, but just the position of certain arms. Here, the vertical arm B will be displaced in both horizontal (x) and vertical (y) directions, as depicted in Figure 4.36 a).

In this way, the structure's symmetry is no longer present because the ROA will not have symmetry on either the horizontal or vertical axis. Analysing this symmetry breaking through symmetry definitions corresponds to transitioning from Type I to Type III. Thus, the investigation begins with a single symmetric (Type I) cross-shaped ROA with the same arm lengths ($A = B = 80\,nm$), as Figure 4.36 shows. In the investigation of partial symmetric cross-shaped ROAs only δ_x was relevant. Here, both displacements δ_x and δ_y are relevant. The polarization direction is also indicated in the same Figure 4.36 a). This antenna becomes an L-shaped ROA with equal arms in the last simulation step. As already mentioned, the volume and antenna arm lengths are kept constant.

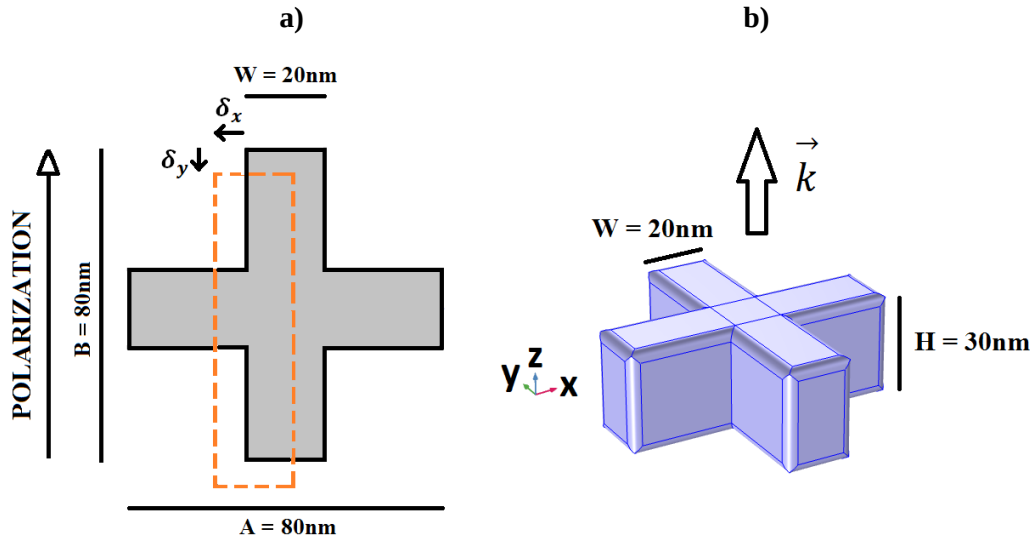

Figure 4.36. (a) Top view of a single partially symmetric cross-shaped ROA (x-y plane) with the antenna arms termed A and B; b) 3D model of the single cross-shaped ROA

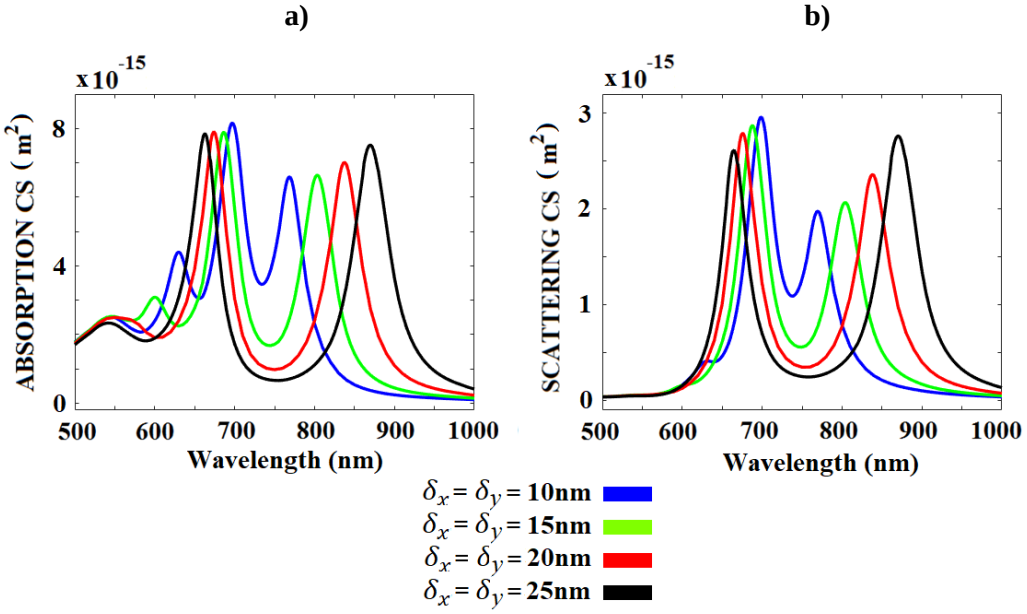

Figure 4.37. (a) Absorption cross-section; (b) scattering cross-section for structure for the design in Figure 4.36.

Numerical results of the optical cross-section at different values of δ_x and δ_y are in Figures 4.37 (a) and (b). It can be seen from these figures that, at $\delta_x = \delta_y = 0$ nm, the cross-shaped antenna is symmetric to both axes and it shows only monomodal behavior. For smaller values of $\delta_x = 5$ nm and $\delta_y = 5$ nm, the multimodal behavior is still not obvious, so it is not necessary to present this case. The main part of our investigation starts from $\delta_x =$

10 nm and $\delta_y = 10$ nm. As it, seen, for these values, the structure already shows slight triple-resonance behavior. Similar behavior but less obvious can be seen for $\delta_x = 15$ nm and $\delta_y = 15$ nm. If we further increase the values of $\delta_x = \delta_y = 20$ nm or $\delta_x = \delta_y = 25$nm, the ROAs show clearly bimodal behavior. In the last step for $\delta_x = \delta_y = 30$ nm the cross-shaped ROA becomes an L-shaped ROA. To analyse more deeply triple-modal behavior, we will choose the case of $\delta_x = \delta_y = 10$ nm which is depicted by the blue color in Figure 4.40 (a). The trimodal nature of the ROA behaviour is especially obvious for the absorption cross-section. From the spectrally dependent cross sections and the analysis of the current density lines for the three different resonances, as depicted in Figure 4.37 and Figure 4.38, it is possible to analyze all three modes. The lowest-frequency ROA eigenmode can be assigned to a smoothly - bent - longitudinal current mode of the longest L-shaped metallic part of the cross-shaped antenna (Figure 4.38 for wavelength 768 nm). The highest-frequency ROA eigenmode can be assigned to a smoothly - bent - longitudinal current mode of the shortest L-shaped metallic part of the cross-shaped antenna (Figure 4.38 for wavelength 630 nm).

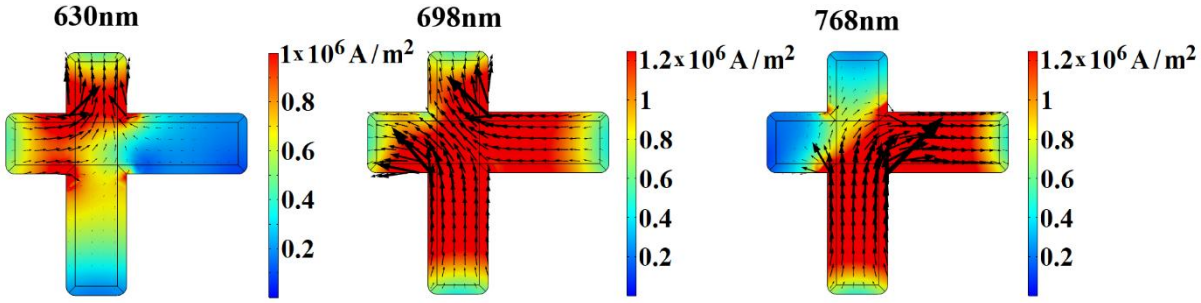

Figure 4.38. The current density of a partially symmetric ROA at the existing three resonances of 630 nm, 698 nm, and 768 nm, respectively. In this study, $\delta_x = \delta_y = 10$ nm.

Finally, between the lowest and the highest frequency ROA eigenmode, there is an eigenmode that has the current mode signature of an out-of-phase longitudinal resonance oscillating along two individual middle-long L-shaped parts of the cross-shaped antenna (Figure 4.38 at the wavelength of 698nm). For $\delta_x = \delta_y = 20$ nm and $\delta_x = \delta_y = 25$ nm the highest energy mode disappears, which is logical because, in these cases, the physical dimensions of "longest L" and "middle-long L" are very close.

4.5.4 Analysis of coupled cross-shaped antennas with equal arms

In this investigation, the approach will be to analyze the first behaviour of cross-shaped coupled ROA with a very small gap with a width of 20 nm. Here, the two coupled Type I cross-shaped antennas have the same arm lengths (A = B = 80 nm). In order to analyze near-field properties in this gap, our first step will be investigating the coupled version of those antennas, as shown in Figure 4.39 (a). Figure 4.39 (b) shows the 3D model in COMSOL Multiphysics. Speaking about symmetry breaking, here we will displace only the arm with length B in horizontal or x direction, as depicted in Figure 4.39 (a). This again corresponds to a transition from Type I to Type II regarding the symmetry. No matter which way is chosen, geometrical parameters of the antenna, like the lengths of the arms (A = B), gap width, and width of arms, are kept constant. The polarization direction is also indicated in the same Figure 4.39 (a). It can be seen from Figure 4.40 that the antenna's spectral response shows a bimodal behavior even for small δx.

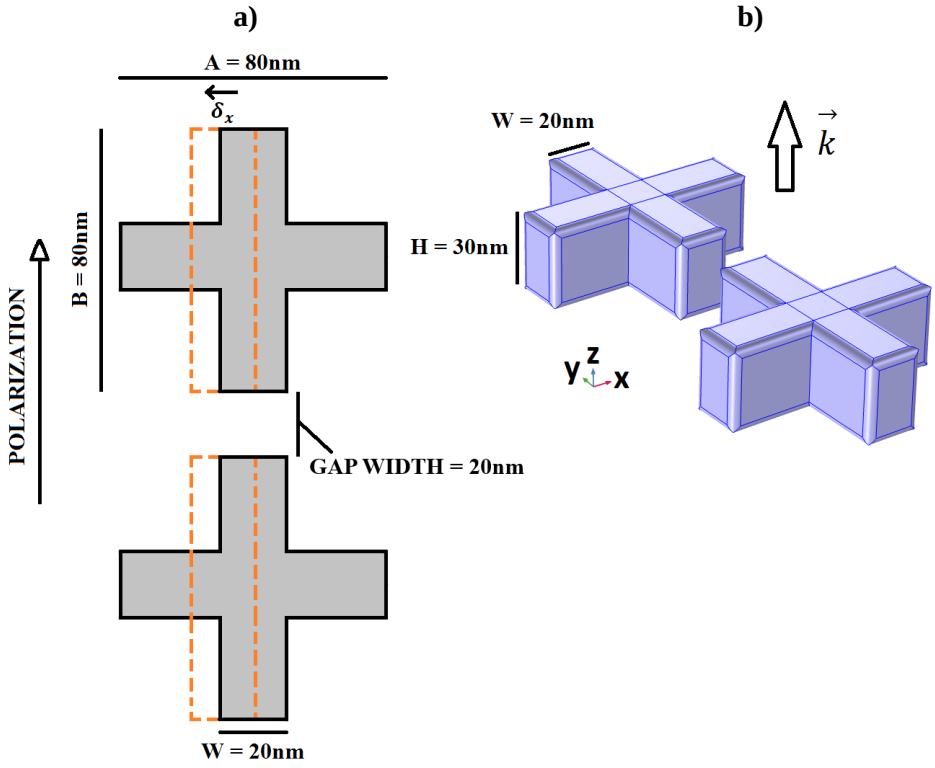

Figure 4.39. a) Top view of a coupled cross-shaped ROA (x-y plane) with equal antenna arms termed A and B where arm B is moved in δx steps in x-direction; b) 3D model of the coupled-cross-shaped ROA.

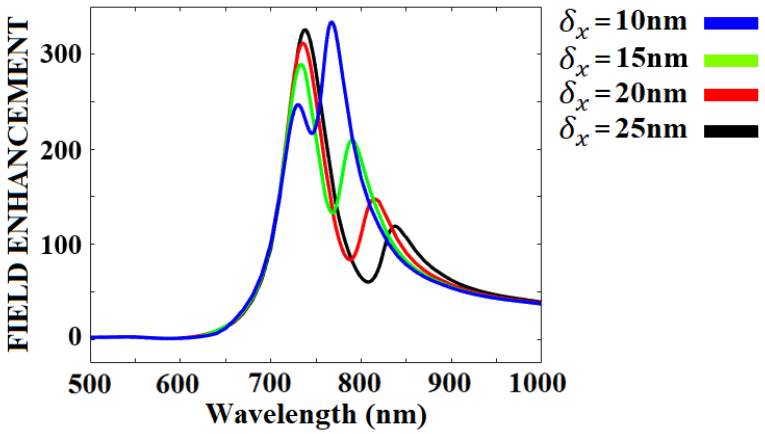

Figure 4.40. Field enhancement $|E_{TOT}|^2/|E_{IN}|^2$ in the gap center for different values of δ_x and gap width of 20 nm.

The high energy resonance shifts to higher wavelengths and becomes more pronounced for higher δx. This figure shows that for every shifting of arm B for 5 nm, there is a smaller red-shifting of high energy resonance (2 nm-3 nm) and a bigger red-shifting of the low energy resonance (22 nm-25 nm). This causes an increasing wavelength separation between the two resonant peaks for every shifting step of arm B. To better understand this wavelength separation, we will perform a current density line analysis for two values of δ_x=10 nm and δ_x=20 nm. These values correspond to the blue and red lines from Figure 4.40. For $\delta_x = 10\ nm$ resonant wavelengths are 730 nm and 767 nm. For $\delta_x = 20\ nm$ resonant wavelengths are 736nm and 815nm. Figure 4.41 b) where $\delta_x = 20\ nm$, clearly shows that the high-energy resonance at wavelength 736 nm takes place mainly on the "rod-part" of the antenna (blue "rod-part" from Figure 4.40). Furthermore, low-energy resonance at wavelength 815 nm takes place mainly on the right-hand side of the "L-part" of the antenna (red "L-part" from Figure 4.40). By increasing δ_x, there is an increase in the effective length of the "L-part" of the antenna and, therefore, an increase in the resonant wavelength of the longitudinal mode that appears on that part of the structure. This will be even more obvious when we analyze triple-modal single cross-shaped antennas. A very important result is shown in Figure 4.41 a) where $\delta_x = 10\ nm$. It shows that the high-energy resonance at wavelength 730 nm takes place on the vertical arm, but due to perturbation, the right-hand side of the "L-part" of the antenna slightly affects it. At the same time, low energy resonance at wavelength 767 nm takes place mainly on the right-hand side of the "L-part" of the antenna, but it is also affected by the vertical arm. It is important to mention that in all simulations; the vertical arm is kept constant (80 nm). Here, we can

presume that these perturbations appear due to the changing of δ_x, and therefore "L-part" of the antenna is getting closer to the vertical arm from a geometric point of view. This agrees with the results shown in Figure 4.40 where the shifting of the high energy resonance by increasing δ_x is much smaller than the shifting of the low-energy resonance.

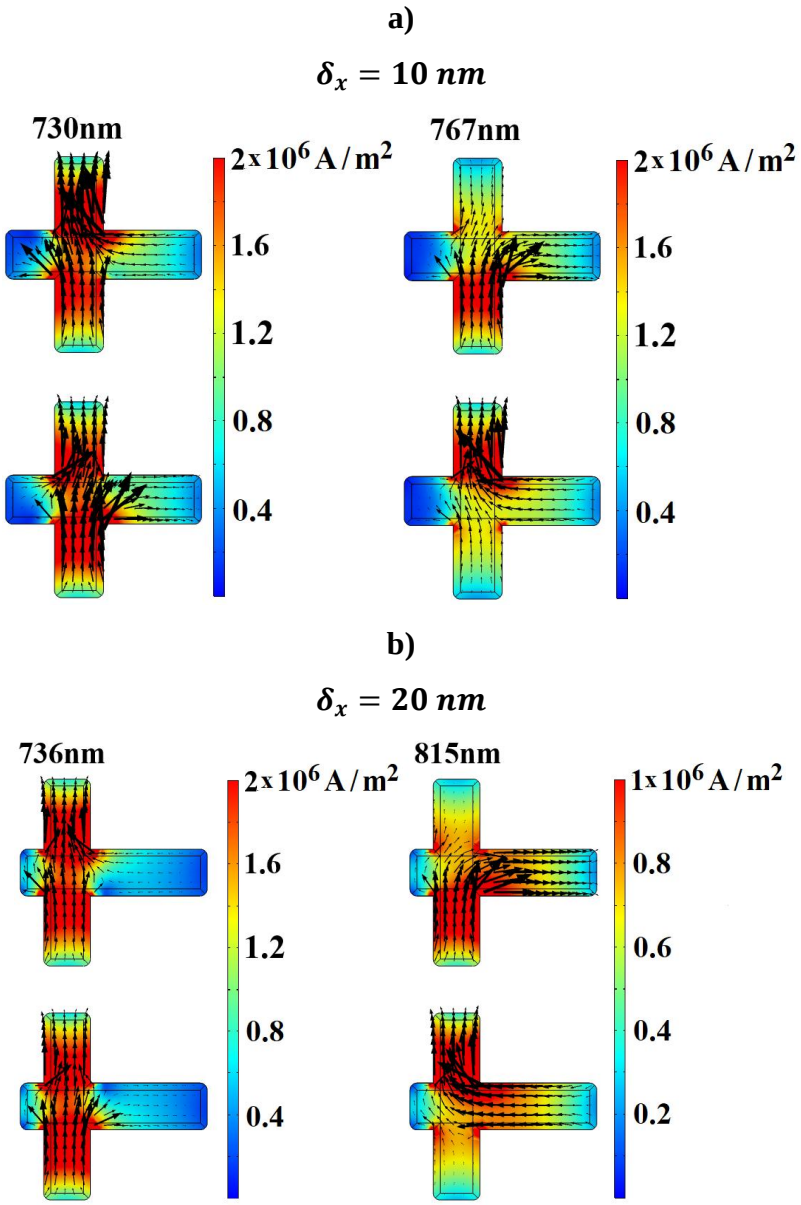

Figure 4.41. a) current density of the bimodal ROA for resonant wavelengths for $\delta_x = 10\ nm$. The ROA resonant wavelengths are 730 nm and 767 nm; b) current density of the bimodal ROA for resonant wavelengths for $\delta_x = 20\ nm$. The ROA resonant wavelengths are 736 nm and 815 mm.

After this analysis, another study will be carried out to investigate the influence of the gap on field enhancement. For this examination, we choose cross-coupled ROA with $\delta_x = 25\ nm$. Figure 4.42 shows the results. It can be noticed that decreasing the gap width significantly

increases the field enhancement in the gap center and shifts the resonance to the low-energy region. If we decrease the gap width, we also increase the capacitance of the gap by applying the general formula. Therefore, we decrease the resonant frequency, which is the red shifting of the resonance.

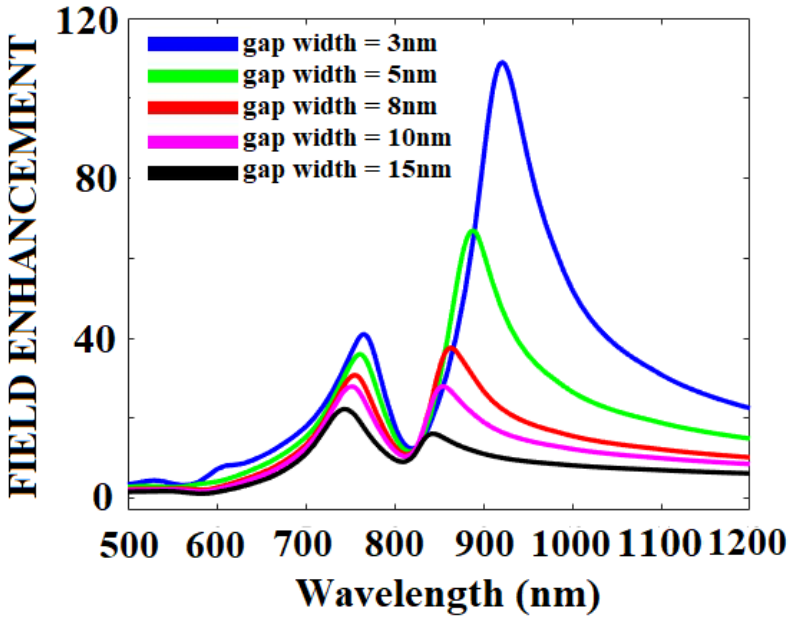

Figure 4.42. Field enhancements $|E_{TOT}|^2/|E_{IN}|^2$in the gap center for several values of gap and the constant shifting value of $\delta_x = 25\ nm$.

Now that we know the resonant behavior of coupled cross-shaped antenna and the influence of the gap, we can make one investigation with a very small gap width of 2 nm. The first part of the investigation, which had a gap width of 20nm, helped us to understand mode analysis. With a small gap width of 2 nm, we want to see possible field enhancement levels. As Figure 4.43 shows, the analysis begins with the two coupled symmetric cross-shaped antennas with the same arm lengths ($A = B = 80\ nm$) and with a gap width of 2 nm. The coupled structures that we investigated are shown in Figure 4.43 a) and b). Figure 4.43 (b) shows the 3D model in COMSOL Multiphysics. As has already been mentioned, there are several ways we can break the symmetry of cross-shaped nanoparticles. Here, we chose to go from symmetry to the partially symmetric cross nanostructure by displacing only the horizontal arm with length B in horizontal or x direction as depicted in Figure 4.43 (a). This corresponds to a transition from Type I to Type II regarding the symmetry. The antenna's Geometrical parameters, like the arms' lengths, gap width, and width of arms, are kept constant. Figure 4.43 (a) also indicates the polarization direction. Figure 4.43 (c) and (e) clearly show that even very small δx nanoantenna

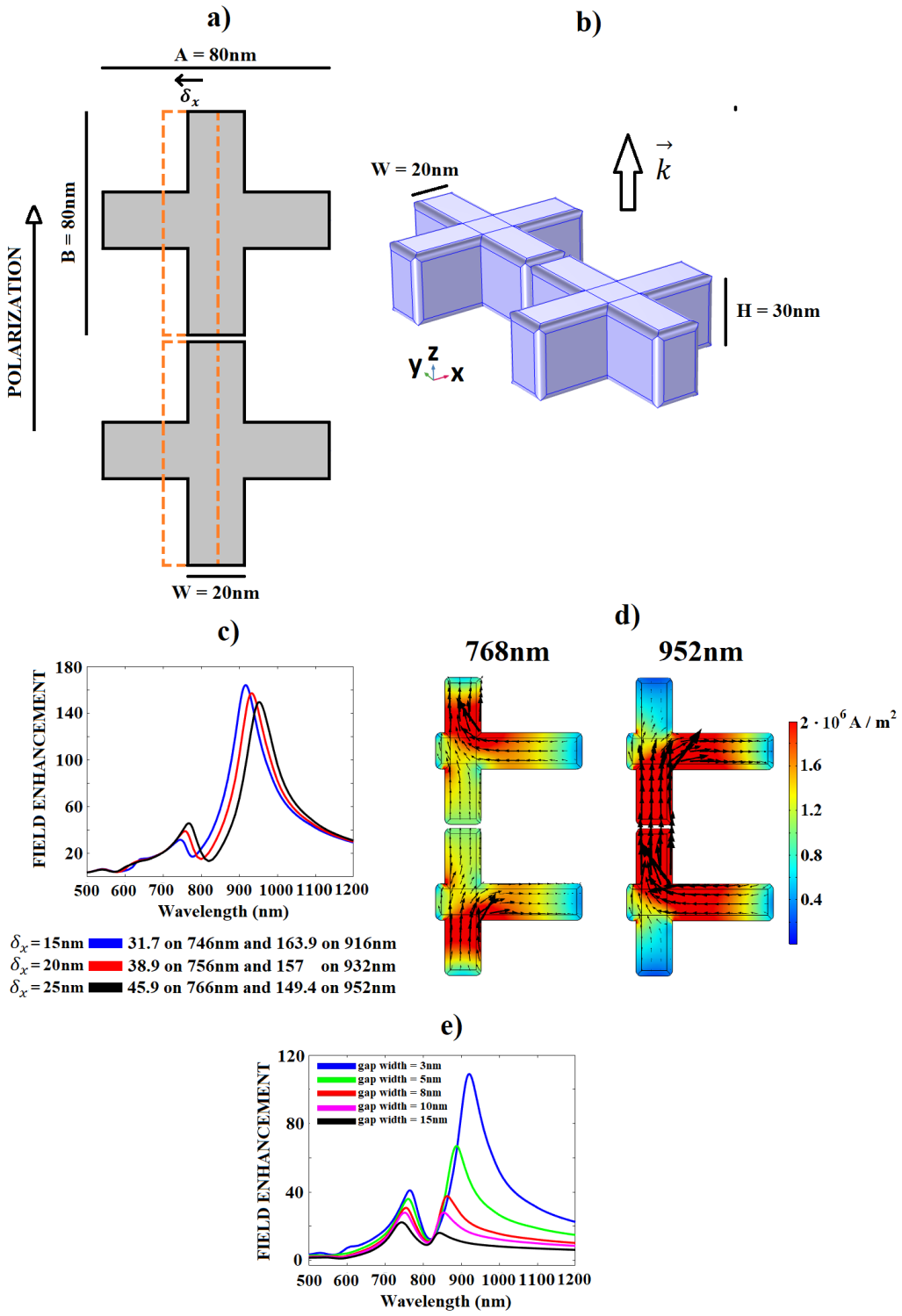

Figure 4.43. a) Top view of a coupled cross-shaped ROA (x-y plane) with equal antenna arms termed A and B where arm B is moved in δx steps in x-direction; b) 3D model of the coupled-cross-shaped ROA; c) Field enhancement $|E_{TOT}|/|E_{IN}|$ in the gap center for different values of δ_x and gap width of 2 nm; d) current density of the bimodal ROA for resonant wavelengths for $\delta_x = 15\,nm$. The ROA resonant wavelengths are 768 nm and 952 nm; (e) field enhancements $|E_{TOT}|/|E_{IN}|$ in the gap center for several values of gap and the constant shifting value of $\delta_x = 15\,nm$.

has bimodal behavior. Moreover, Figure 4.43 c) shows that for every shifting of the arm with length B for 5nm, there is a red-shifting of high energy resonance for around 10 nm and red-shifting of the low energy resonance for around 20nm. Therefore, every shifting of the arm with length B in the left direction causes increasing wavelength separation between the two resonant peaks. For field analysis, we choose a cross-shaped antenna with $\delta_x = 25\,nm$ (a black line in Figure 4.43 (c)). For the low-energy resonant wavelength of 952 nm, it can be seen in Figure 4.43 (d) that the "L-part" of the antenna has the strongest influence on low-energy resonance. If δ_x increases, there is an increase in the effective length of the "L-part" and therefore an increase in the resonant wavelength of the longitudinal mode that appears on that part of the structure. Later, this will be clearer in the triple-modal analysis. Figure 4.43 (d) also shows that the high energy resonance with wavelength 768 nm is influenced by the vertical arm and partially by the "L-part" of the antenna. This is why the shifting of the first resonance by increasing δ_x is much smaller than the shifting of the low energy resonance.

4.5.5 Triple-modal cross-shaped antennas

Until now, only cross-shaped antennas with monomodal or bimodal behavior have been discussed. Previous investigation and Figure 4.37 shows that three resonances can be observed for special types of cross-shaped ROA because some "parts" of the cross-shaped antenna have a stronger influence on specific resonant behavior than other "parts". Figure 4.37 a) shows that in the case of a partially symmetric antenna, the most decisive influence on the resonance comes from the vertical rod when the polarization direction is vertical. At the same time, Figure 4.38 shows that some "L-parts" of the asymmetric cross-shaped antenna influence certain resonances of three existing resonances. Besides polarization conditions, for detailed analysis of triple-mode resonance behavior, it is crucial that a cross-shaped antenna could be interpreted as a combination of L-shaped and rod-like antennas (Figure 4.44). If we choose a cross-shaped antenna that has a different effective length of blue, green, and red parts of the antenna (Figure 4.44), we can build triple-resonant structures. The cross-shaped antenna's shorter "L-part" can be assigned to the first high-energy resonance (blue color in Figure 4.44). The "vertical rod-part" of the cross-shaped antenna can be assigned to the second resonance (green color in Figure 4.44). Finally, the longer "L-part" of the cross-shaped antenna can be assigned to the third resonance (red color in Figure 4.44). Thus, under certain polarization conditions, it is

possible to design a cross-shaped antenna exhibiting even three resonances in the optical and near-IR spectrum.

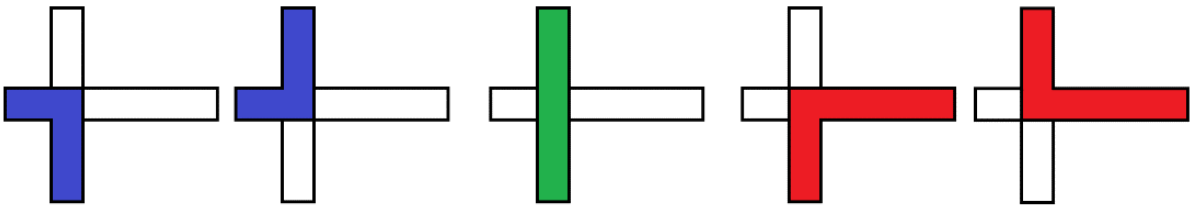

Figure 4.44: A partially symmetric cross-shaped antenna can be regarded as composed of two L-shaped antennas (shown in blue and red) and one rod-like antenna (shown in green).

From the L-shaped bimodal structures but also rod-shaped monomodal structures, we observed that it is essential to study the polarization dependence of the antennas. To investigate the triple-modal structure, we will use partially symmetric antennas with symmetric arms in the y-direction. Optical and near-IR properties will be studied by shifting the vertical arm without changing the arm length and horizontal arm length without arm shifting. Therefore, new notations like A_{LEFT}, A_{RIGHT}, B_{BELOW} and B_{ABOVE} in Figure 4.45 need to be introduced. In the first simulation set, we modify just the length A_{LEFT} (increase length of left arm) as shown in Figure 4.45, while all other variables remain constant. In all simulations regarding triple-modal ROAs, the polarization angle will be 30^0 as shown in Figure 4.45.

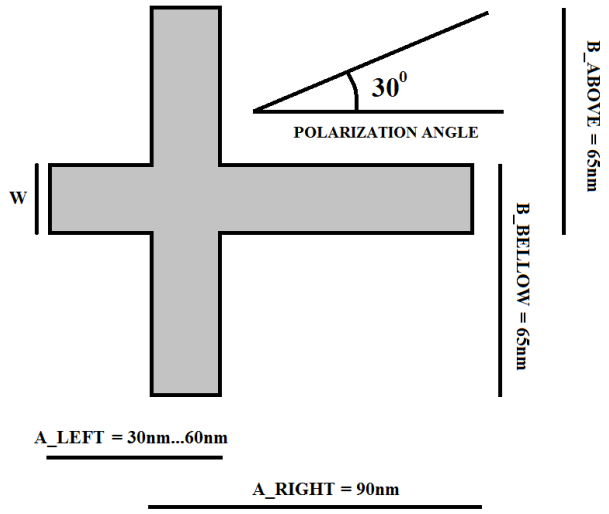

Figure 4.45: Top view of a single cross-shaped ROA (x-y plane) with antenna arms B_{BELLOW}= 65 nm, B_{ABOVE}= 65 nm, A_{RIGHT}= 90 nm. A_{LEFT} varies from 30 nm to 60 nm in 5nm steps.

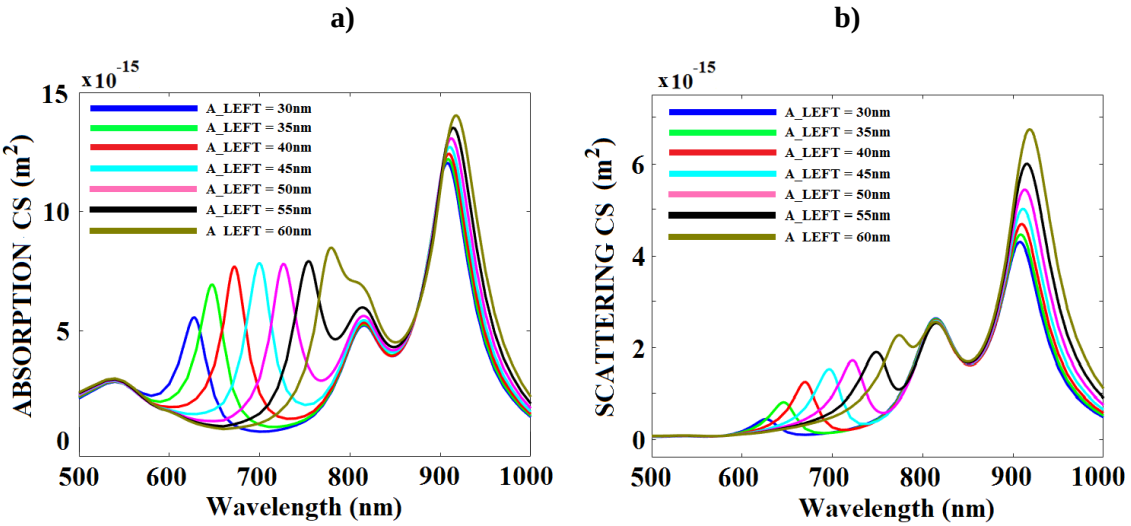

Figure 4.46: Far-field properties of single asymmetric cross-shaped ROAs with changing arm length in the left direction (A_{LEFT}). a) absolute absorption cross-section of ROA; b) absolute scattering cross-section of ROA. Absorption and scattering cross-section are calculated according to classical antenna theory.

Results in Figure 4.46 show that the second resonant wavelength at 814 nm remains almost constant. It is attributed to the rod-like antenna mode given by the vertical arm of the antenna (green part in Figure 4.44). The current density shown in Figure 4.47 for 814 nm agrees with this statement.

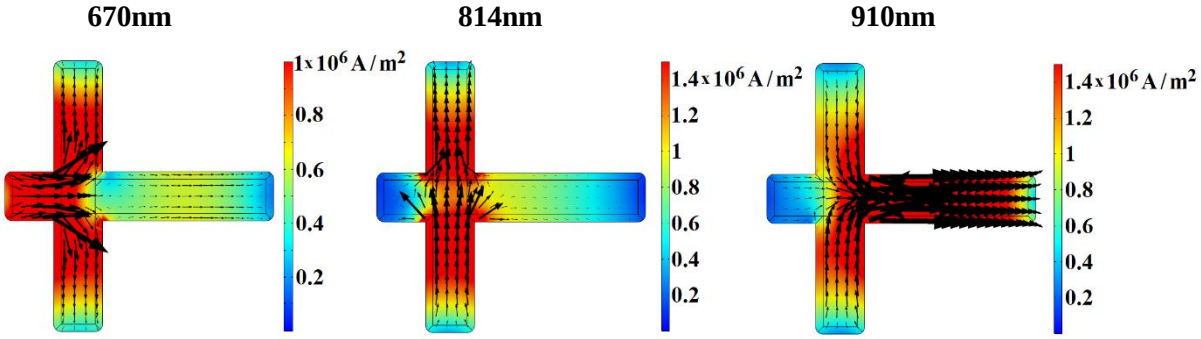

Figure 4.47: Current densities of the resonances for resonant wavelengths 670 nm, 814 nm, and 910 nm for $A_{LEFT} = 40\ nm$. The color bar represents j (current density) with the vector representation of the current modes for the partially symmetric cross-shaped configuration.

Furthermore, Figure 4.46 shows a slightly red shifting of the third resonant wavelength while A_{LEFT} increases. This is attributed to the fact that this resonance takes place mainly on the right-hand side "L-part" of the antenna (red "L-part" from Figure 4.44). However, this resonance, on the other hand, due to perturbation it is a little bit affected by a modification of A_{LEFT}. Table

4.6, which shows resonant wavelengths for the third resonance, which will clarify this phenomenon.

As can be seen in Table 4.6, the resonant wavelength remains constant at 908 nm for smaller values of A_{LEFT}. For higher values of $A_{LEFT} = 45\ nm$ resonant wavelength starts to rise. In all simulations B_{BELOW} and B_{ABOVE} are kept at constant (65 nm). Therefore, we can presume that increasing A_{LEFT} has some influence on low-energy resonance since A_{LEFT} is getting closer to the B_{BELOW} and B_{ABOVE} from a geometric point of view.

Table 4.6: Resonant wavelengths of low energy resonances for different values A_{LEFT}

A_{LEFT} (nm)	Resonant wavelength of the low energy resonance (nm)
30	908
35	908
40	908
45	911
50	913
55	915
60	922

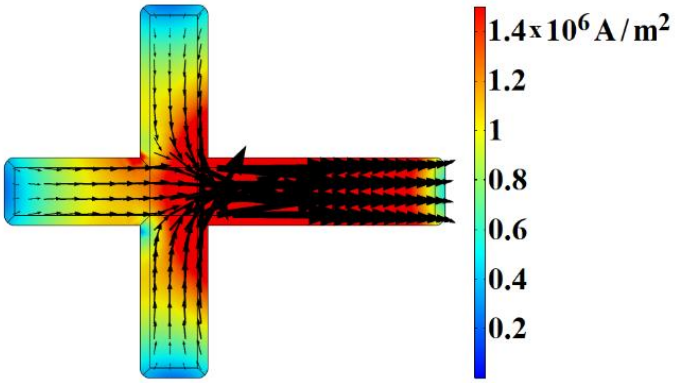

Figure 4.48 Current density of the resonance for resonant wavelength 922 nm for $A_{LEFT} = 60\ nm$. The color bar represents j (current density) with the vector representation of the current modes for the partially symmetric cross-shaped configuration.

This statement is explained by Figure 4.48, which presents the current density with field lines on a resonant wavelength 922 nm for $A_{LEFT} = 60$ nm. It clearly shows the significant impact of B_{BELOW} and B_{ABOVE}, but also of A_{LEFT} on a low energy resonant wavelength.

In the next simulation set, we used the geometry from Figure 4.49 where only A_{RIGHT} is modified in 5 nm simulation steps while other values are kept constant ($B_{BELOW} = 65\ nm$, $B_{ABOVE} = 65\ nm$, and $A_{LEFT} = 40\ nm$). The polarization direction angle is again set to 30^0 .

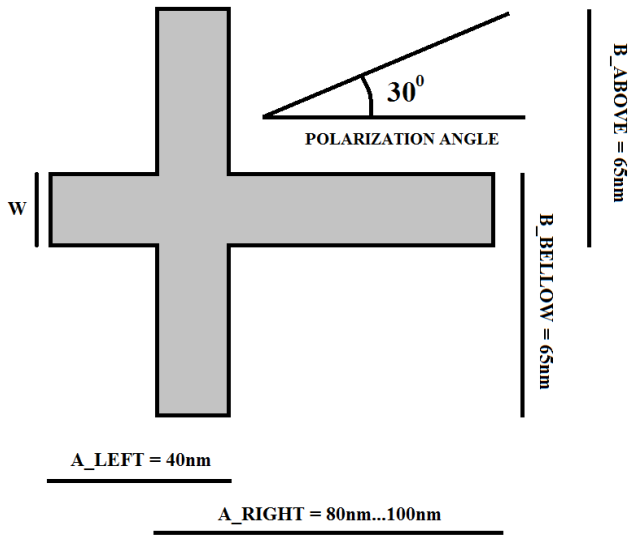

Figure 4.49: Top view of a single cross-shaped ROA (x-y plane) with the antenna arms B_{BELLOW} = 65 nm, B_{ABOVE} = 65 nm, A_{LEFT} = 40 nm. A_{RIGHT} varies from 80 nm to 100 nm in steps 5 nm.

Results in Figure 4.50 a) and b) show that the first and second resonant wavelengths remain almost constant. The explanation for this is that changing the dimension of A_{RIGHT} causes a changing length of the red "L-part" of the cross-shaped antenna depicted in Figure 4.44. As mentioned, this red "L-part" of the cross-shaped antenna has the dominant influence on the third resonance. Thus, the other two resonances remain almost constant.

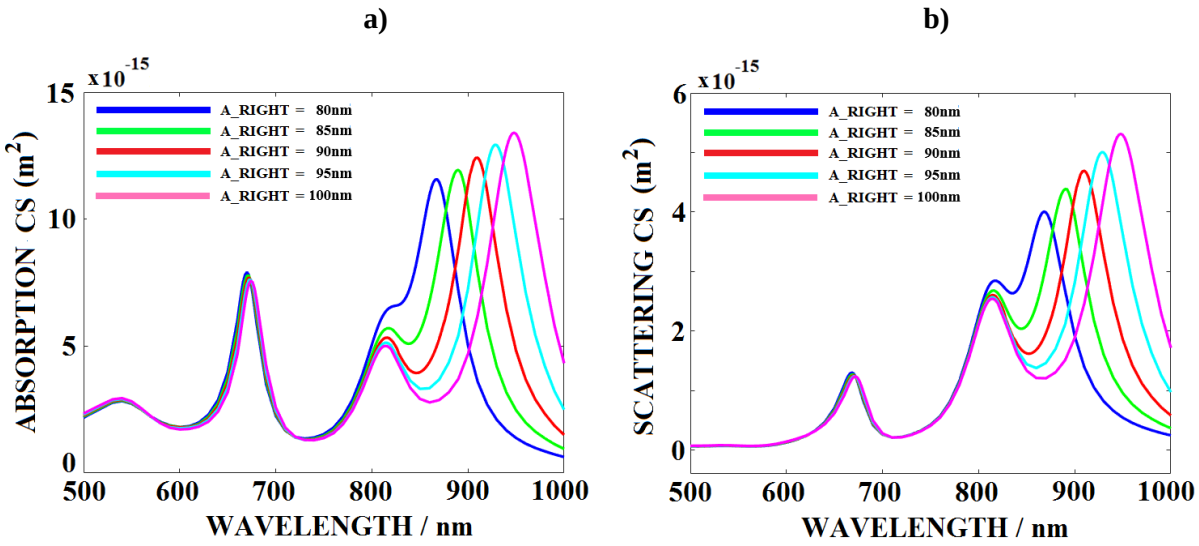

Figure 4.50: Far field optical properties of single asymmetric cross-shaped ROAs with changing arm length in the right direction (A_{RIGHT}). a) absolute absorption cross-section of ROAs; b) absolute scattering cross-section of ROAs.

The third simulation set examines the effect of shifting the vertical arm in steps of 5nm, as shown in Figure 4.51. From a geometric point of view, this is similar to the investigation from Figure 4.35, where a partially symmetric cross-shaped antenna is analyzed, but here the polarization angle is set to $30°$ and physical dimensions are different. Here, shifting the vertical arm to the left side means decreasing of A_{RIGHT} and increasing of A_{LEFT} while other values are kept constant ($B_{BELOW} = 65\,nm$ and $B_{ABOVE} = 65\,nm$). Figure 4.52 shows that the resonant wavelength of the second resonance remains the same during all simulation steps, as arm B has a constant length, and the resonant wavelength of the second resonance remains the same during all simulation steps. If we analyze the results in Figure 4.52, the first resonance shifts red because increasing A_{LEFT} leads to an increased length of the short "L-part" of the cross-shaped antenna (blue color from Figure 4.44), which strongly influences the first resonance. Finally, the third resonance in Figure 4.52 shifts blue because the decreasing A_{RIGHT} will decrease the length of the long "L-part" of the cross-shaped antenna (red color from Figure 4.44), strongly influencing the third resonance.

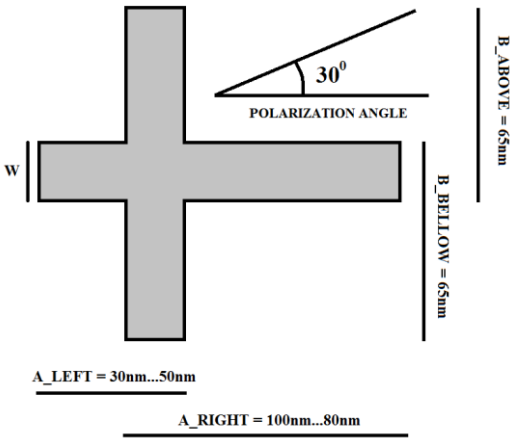

Figure 4.51: Top view of a single cross-shaped ROA (x-y plane) with the antenna arms B_{BELOW} = B_{ABOVE} = 65 nm. A_{LEFT} varies from 30 nm to 50 nm in steps 5nm. A_{RIGHT} varies from 100 nm to 80 nm in steps 5 nm.

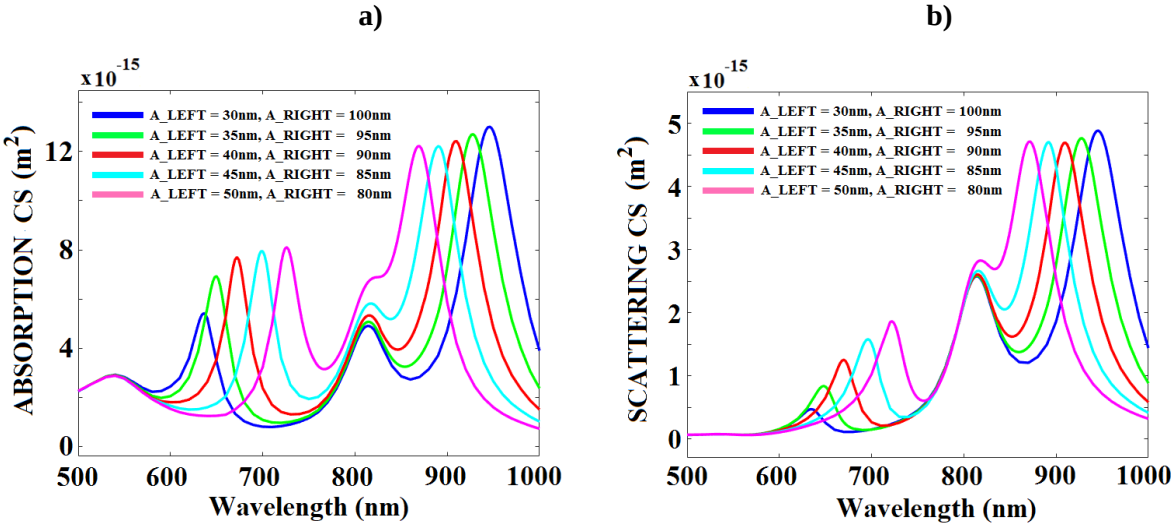

Figure 4.52: Far field optical properties of single asymmetric cross-shaped ROAs without changing arm length but with "morphing" antenna form (moving horizontal rod in the right direction). a) absolute absorption cross-section of ROA; b) absolute scattering cross-section of ROA. Absorption and scattering cross-section are calculated according to classical antenna theory.

These single cross-shaped triple-modal antennas are also polarization-sensitive. Figure 4.53 shows optical properties of a partially symmetric ROA with $B_{BELOW} = B_{ABOVE} = 65\,nm$ and $A_{LEFT} = 40\,nm$, $A_{RIGHT} = 90\,nm$. If we calculate arm lengths, in this case, both arm lengths are 110 nm. The interesting point is that the spectrum can be tuned for all three resonances. Each spectral response can be tuned because the "L-parts" and "rod-parts" of the cross-shaped antenna are also polarization-sensitive. As we already saw in the case of bimodal cross-shaped antennas, if the light is polarized with proper polarization angle direction, it is possible to tune

the spectral response intensity by changing the polarization angle. In the case of trimodal cross-shaped antennas, it is similar.

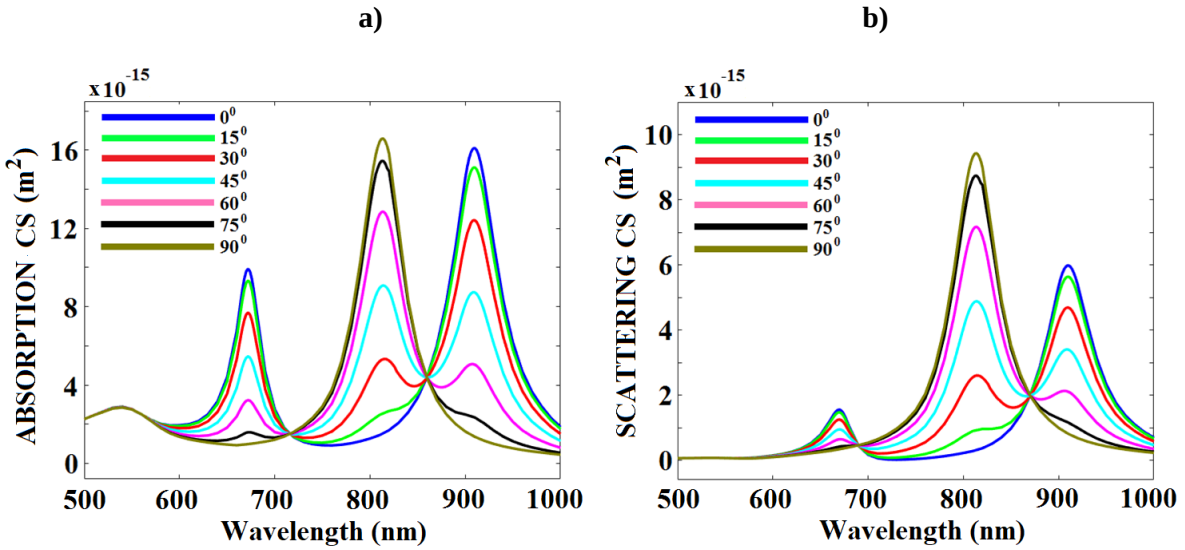

Figure 4.53: Electromagnetic plane wave excitation dependence of the scattering and absorption cross-section as a function of linear polarization change for a symmetric cross-shaped ROA with constant arm lengths; a) absorption cross-section with a set of varying linearly polarized plane waves; b) scattering cross-section with a set of varying linearly polarized plane waves.

Finally, the polarization sensitivity of the coupled cross-shaped structure from Figure 4.54 is also investigated for several polarization angles, and the constant shifting value of $\delta_x = 25$ nm.

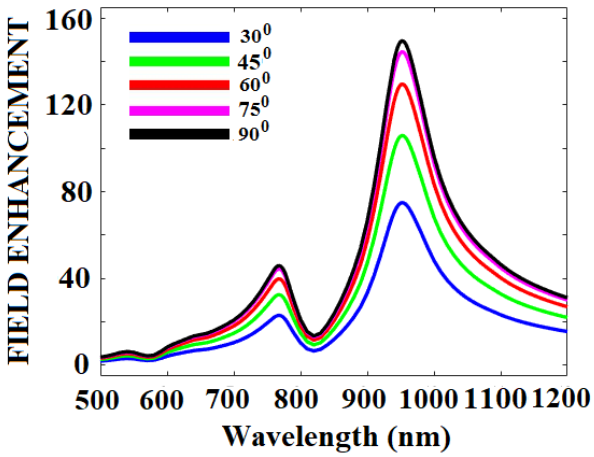

Figure 4.54: Field enhancement $|E_{TOT}|/|E_{IN}|$ in the gap center for different values of polarization angle and gap width of 2 nm.

The only difference here is that we will use a gap width of 2 nm to see how polarization impacts very small gaps. Results are shown in Figure 4.54, where it can be seen that the polarization angle of 90^0 gives the highest enhancement, which is logical for this kind of configuration. Like in the single cross-shaped polarization investigation, there is no resonant shifting by changing the polarization angle.

4.5.6 Discussion

Cross-shaped ROAs are excellent examples of how we can use plasmon length definition to make bimodal or trimodal cross-shaped nanoantennas. In this investigation, we did not change the height and width of the antennas. Therefore, the only parameter which affects particle volume is longitudinal length. Constant particle width is in direct relation to constant transversal particle resonance frequency. It is shown in several figures where absorption cross-sections were presented (Figure 4.32 a), Figure 4.33 b), Figure 4.35 a), Figure 4.37 a), Figure 4.46 a), Figure 4.50 a), Figure 4.52 a), Figure 4.53 a)). For the triple-modal antenna, crucial for analysis is Figure 4.44, which shows that cross-shaped antennas can be regarded as a combination of rods and L-shaped parts and also shows which "part" of the cross-shaped antenna is "responsible" for which resonance. For this analysis, vector representations of the current flows are in Figure 4.33 e), Figure 4.35 c), Figure 4.38, Figure 4.41, Figure 4.43 d), Figure 4.47, and Figure 4.48. This concept allowed us to use plasmon-length basis functions for building multi-modal blocks. In the case of the bimodal cross-shaped nanoantennas, we can reconstruct the eigenmodes of the cross-shaped nanoantenna by using the plasmon length basis functions of the rod-like nanoantennas. For analyzing single cross-shaped ROAs, we can use two gold nano-bars with lengths of 60 nm and 80 nm. Resonant wavelengths for the 60 nm and 80nm gold single nanorod ROAs are 656 nm and 725 nm, respectively. Figure 4.33 shows that the plasmon length of the cross-shaped ROA defining the low-energy eigenmode is 706nm, being significantly shorter than the low-energy mode for the 80 nm individual gold nanorod (725 nm). Also, the plasmon length of the cross-shaped ROA defining the high energy eigenmode is shorter than the 60 nm individual gold nanorod (642 nm < 656 nm). These energy ROA resonances 642 nm and 706 nm correlate to a plasmon length of rods with lengths 57 nm and 75 nm, which we numerically confirmed. The obvious blue-shifting of the resonance can be interpreted due to the perturbation of current flows like in Figure 4.33 e), thus shortening the effective plasmon length of the cross-shaped antenna arms compared to the original rod-

shaped ROAs. Furthermore, it is clear that if we keep the length of one arm constant, the resonance along that arm is almost independent of the exact positioning of the second arm (Figure 4.46 and Figure 4.50).

5 Slot antennas

In this chapter, we will discuss “inverted” antennas compared to the rod antennas, L-shaped and cross-shaped nanoparticles discussed in the previous chapter. The theory relies on Babinet’s principle, formulated in the 1800s by the French physicist Jacques Babinet [119]. Initially, it was established as an optical principle but was later used extensively in high-frequency technology [120] to analyze aperture antennas. It makes an analogy between two cases:

1) We have a metallic nanoparticle with some cross-section shape and a certain height
2) We have a metallic plate or layer or film and one hole in that structure, which has exactly the same cross-section shape as the nanoparticle in case 1)

This analogy will be investigated numerically through simulations of near-field behavior. If we have an array of slots in some noble metallic layer, optical transmission through this sub-wavelength structure [121] is very useful in different applications besides plasmonic solar cells.

5.1 Slotted transmission lines and waveguide radiators

Engineers in the microwave/RF industry have used transmission line systems for very different applications for decades. If we speak about slotted rectangular waveguides, this transmission line system is used in radar technology since 1960. The concept is deeply investigated, especially in 915Mz and 2.45GHz (so-called ISM band). There are many sources where the operation of these waveguides is investigated [122, 123, 124]. These slot radiators are very commonly used in telecommunication and radar applications and can also be used in microwave heating technology. They are polarization-sensitive and can be designed in many ways depending on the inclination angle and position of the slots. In recent years, they have also been very often used as electromagnetic radiation in microwave chambers and cavities. One of the biggest challenges in the microwave heating industry is dealing with homogeneous heating of different materials. These radiators can be used as EM heaters in the cavity with certain design methods.

The slotted waveguide, in principle, radiates the power through slots that can be positioned on the broad or narrow walls of a waveguide. In practice, they can be designed as resonant and non-resonant structures. The wave in the resonant slotted waveguide is a standing wave, and the wave in the non-resonant slotted waveguide is a traveling wave. There is a common procedure for the design of a resonant type of this structure.

$\lambda_0 -$ wavelength in free space

$\lambda_{cutoff} -$ this is the cutoff wavelength. For the wavelength higher than the cutoff wavelength, there is no wave propagation in the waveguide.

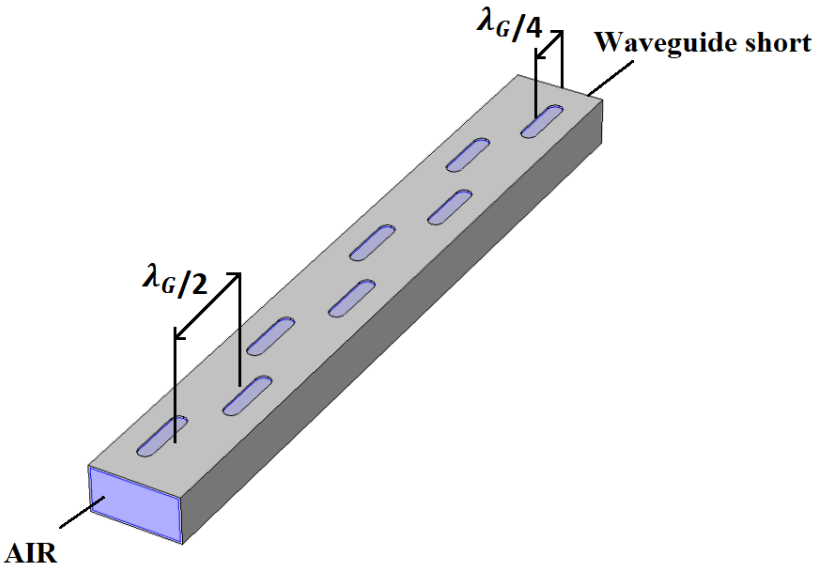

Figure 5.1: Slotted rectangular waveguide or radiating waveguide. The picture is drawn in software COMSOL Multiphysics

For engineers, the most important mode in a slotted rectangular waveguide is the first TE10 mode, which has a working frequency above the first cutoff frequency and below the second cutoff frequency. For this mode, the guide wavelength, which is the distance between two equal-phase planes along the waveguide, can be calculated.

$$\lambda_G = \frac{\lambda_0}{\sqrt{1 - \left(\frac{\lambda_0}{\lambda_{cutoff}}\right)^2}} \tag{5.1}$$

Some rules have already been established for the design of slots. The first slot should be at a distance $\lambda_G/4$ from the feed side of the waveguide, and the last slot should be at a distance $\lambda_G/4$ from the short-circuit side of the waveguide. Longitudinal distance between slots should be around $\lambda_G/2$ like in Figure 5.1.

5.2 Radiating cables or leaky wave transmission line systems

Another application is mobile communication. Radiating cables have been used since 1970, but they have become very important in recent years because of the very high number of internet users. Without those cables, it is very hard to provide the signal in indoor areas, especially tunnels. Therefore, engineers use radiating cables or leaky wave cables. These cables are designed similarly to any other RF cable (inner conductor, outer conductor, dielectric foam, or some dielectric spacer between inner and outer conductor and jacket around the outer conductor), but to provide internet signal in indoor systems, we have slots in the outer conductor. These slots have different sizes and angle inclinations. Radiating cables are designed with periodic slot groups like in Figure 5.2. This periodicity causes reflection peaks at the first resonance frequency and higher-order harmonics. Engineers use the method established by Dr. Petri to suppress higher-order harmonics [125]. The final goal in designing these cables is to provide proper system loss of the cable, consisting of attenuation loss and coupling loss. These values (especially coupling loss) are very polarization-sensitive. Therefore, the sizes and angle inclination of slots are crucial for design [126].

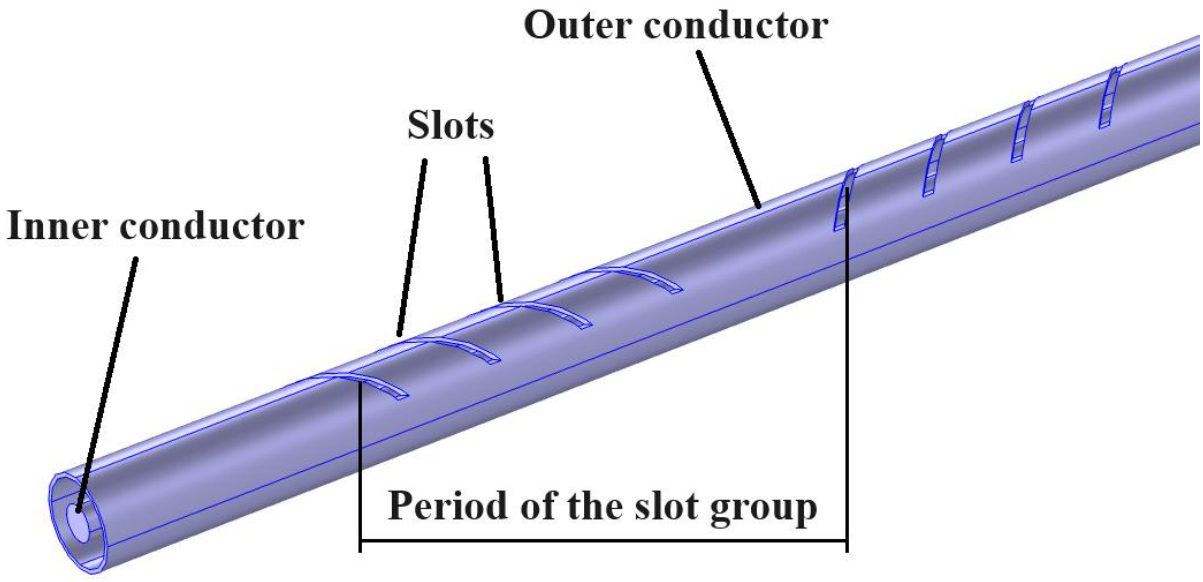

Figure 5.2: Radiating cable or leaky wave. The picture is drawn in the software Comsol Multiphysics.

This concept can also be applied in the optical and near-IR regimes. This technology has become very prominent in recent years since new manufacturing methods can provide slot dimensions below the operating wavelength in these regimes.

Until now, we have discussed electric dipole resonances while investigating usual optical and near-IR nanoparticles or ROAs. In the case of the slot antennas, we are rotating the system by 90^0. Thus, we exchange magnetic and electric field components of the incident wave and actually cause a magnetic dipole moment [127]. Based on the size of the slot and polarization direction, we can optimize parameters and provide the best possible desired radiation behavior. Of course, investigation in optical and near-IR regimes is different because, in microwave bands, we are not dealing with the plasmonic behavior of the metal. Therefore, metal is always observed as a perfect electric conductor.

Babinet's principle relates the diffraction patterns generated by opaque bodies to the diffraction patterns generated by complementary bodies. The term "complementary" here refers to a hole in a metal plane with the same shape and size as the original opaque body (Figure 5.3).

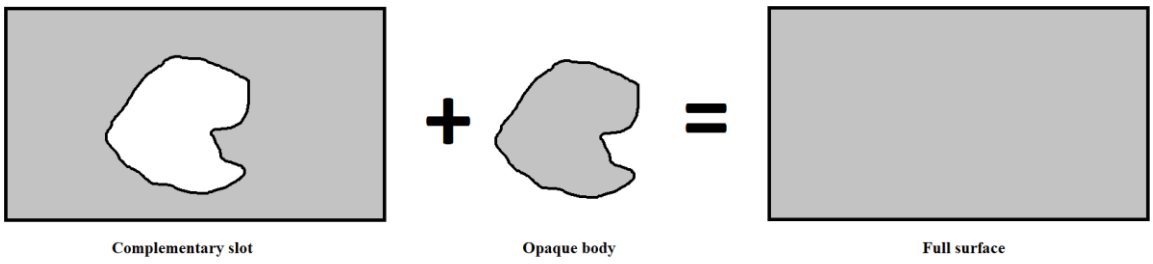

Figure 5.3: Dividing of the surface on the opaque body and complementary slot

Babinet's principle says that the sum of radiation patterns from an opaque body and its complementary slot equals the radiation pattern caused by the overall body. If we talk about LSPR, an opaque body as a nanoparticle should show the same radiation characteristics as its complementary slot but with an inverted phase. That means if we polarize the nanoparticle along one axis to have the same radiation response, we should polarize its complementary slot along the axis perpendicular to the previous one. Therefore, the electric field in the case of the nanoparticle and the magnetic field in the case of its complementary slot are parallel.

As we mentioned in coupled ROAs in previous chapters, highly localized fields in gaps can be used in Raman experiments. In slot antennas, nanoholes also could be used for similar purposes [128, 129, 130, 131, 132]. Plasmonic slot antennas are generally used for different photonic

devices [133]. The simplest way to analyze this principle is to investigate rod nanoparticles and rectangular slots in metallic layers with equal length and width. Of course, the height of the rod nanoparticle is the same as the thickness of the metallic layer. Compared to the classic rod nanoparticle, the electric field of the incident wave needs to be rotated by an angle of 90 end superscript to the 0 Numerical setup, similar to the previous investigation with some differences. Here, we set the height of the metallic layer where slots are made at 70nm. The reason for that is if we go with a smaller height of the metal, we can also see the influence of height on field distribution, and we want to avoid additional resonances caused by height. This setup will also be used to investigate L-shaped and cross-shaped nanoantennas. Some papers with these slot antenna shapes are already published [29, 134, 135, 136].

5.3 Rod-shaped slot antennas

This is the simplest example of Babinet's principle. When we had standard rod-shaped nanoparticles, the electric field polarization direction would be along the longitudinal axis if we wanted to reach maximum scattering and absorption. If we make rod-shaped slots in the metallic layer, to provide maximum field enhancement in the center of that slot, as we already mentioned, we need to rotate the electric field for 90°. Rod length varies from 80nm to 140nm in 10nm steps. The rod width is 20nm, and the metallic layer height is 70nm. Of course, the depth of the slot nanoantennas is the same as the thickness of the gold film, which is deposited only on glass. We calculated field enhancement for every simulation in the middle of the slot. Also, we represented field distribution and current lines, as in previous investigations with nanoparticles.

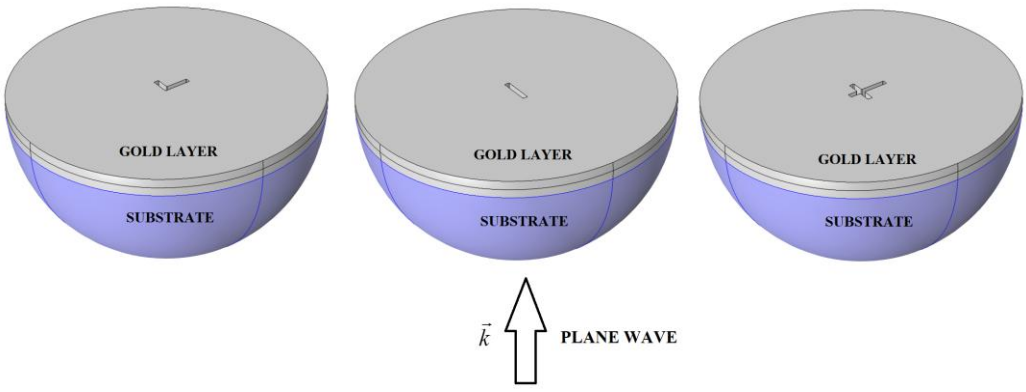

Figure 5.4: Simulation geometry in COMSOL Multiphysics for all three slot antenna types (L-shaped, rod-shaped, and cross-shaped from the left to the right).

Figure 5.5 shows a top view of the structure that should be investigated. It is worth noting that the height of the gold layer is 70 nm to avoid the influence of the vertical mode on SPP analysis. This structure is also polarization-sensitive.

We will analyze the results by calculating field enhancement exactly in the red point from Figure 5.5, which is in the middle of the gold layer height. All dimensions except slot length (L) are constant. The polarization angle is 0^0 in all simulation steps. Therefore, this slot antenna behaves like a magnetic dipole. This is a typical example of Babinet's principle. When we analyze rod-shaped ROA for the best results, it was necessary to orient polarization along the longitudinal axis of the ROA. Here we need to orient polarization along the transversal axis of the antenna. This is exactly 0^0 in Figure 5.5. We plotted results for six different rod lengths between 80 and 130 nm.

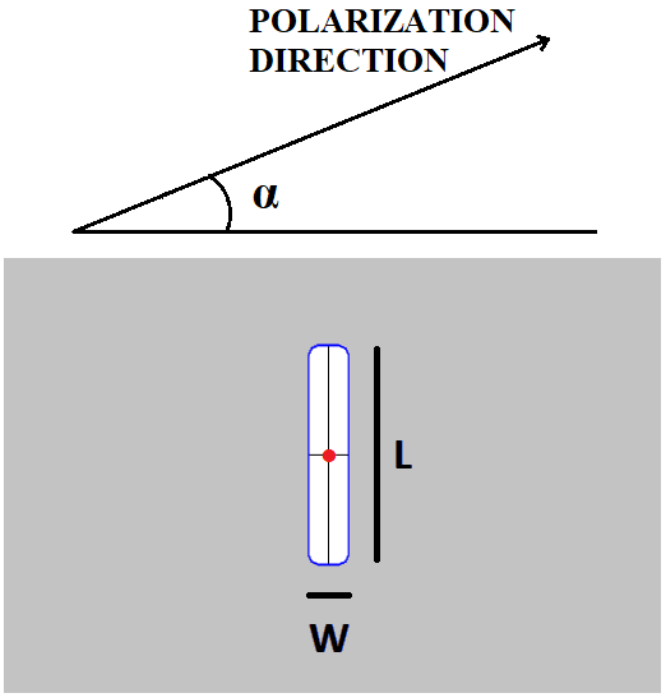

Figure 5.5: Top view of the optical rod-shaped slot antenna. Field enhancement is calculated in the red dot placed in the middle of the gold layer height.

Results from Figure 5.6 show the expected red-shifting of resonant peak wavelength with an increase in the slot length. We can also observe higher field enhancement in the slot for longer slots. It is noticeable that these field enhancement levels are much higher than coupled rod-shaped ROAs from Chapter 4.2.1. Also, in Figure 5.7, the polarization sensitivity of rod-shaped optical slot antenna can be seen. The polarization angle is plotted in Figure 5.5. The orientation

of polarization impacts field enhancement in the slot but not on the wavelength of the resonance.

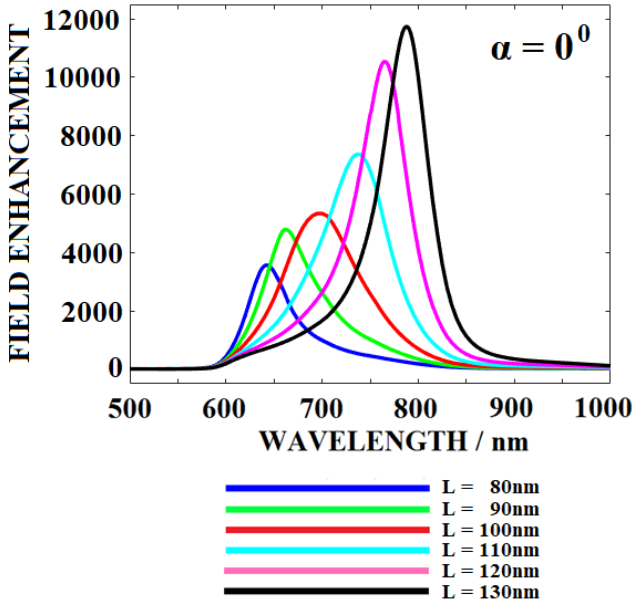

Figure 5.6: Near field optical properties (field enhancement) of rod-shaped optical slot antenna with increasing slot length. Field enhancement is calculated in the red dot from Figure 5.5. Field enhancement on the y-axis is $|E_{TOT}|^2/|E_{IN}|^2$.

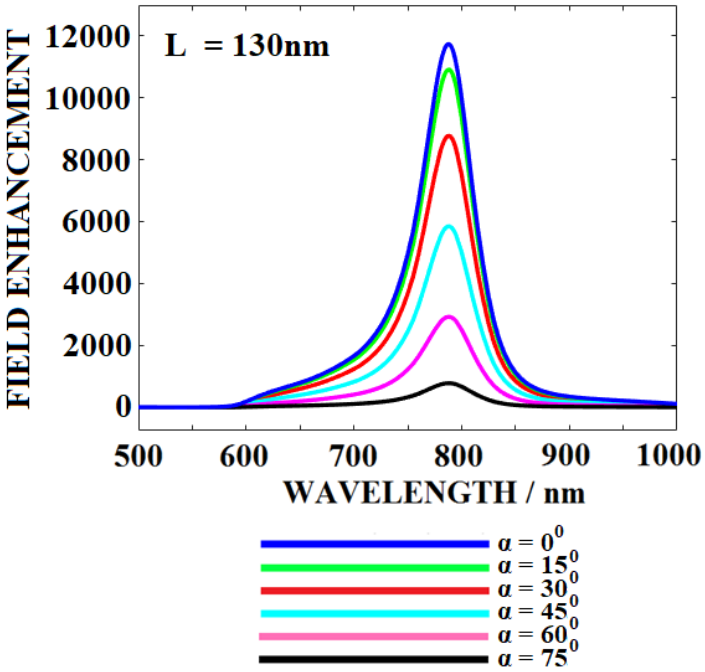

Figure 5.7: Near field optical properties (field enhancement) of rod-shaped optical slot antenna with different polarization angles. Field enhancement is calculated in the red dot from Figure 5.3. Field enhancement on the axis is $|E_{TOT}|^2/|E_{IN}|^2$.

Figure 5.7 does not present results for the polarization angle of 90^0 since in that case spectral response is insignificant to bi visible in comparison with spectral responses caused by other incident waves with the other polarization angles. This is similar situation which we had during investigation of rod-shaped single ROA where we observed transversal mode in Figure 4.11.

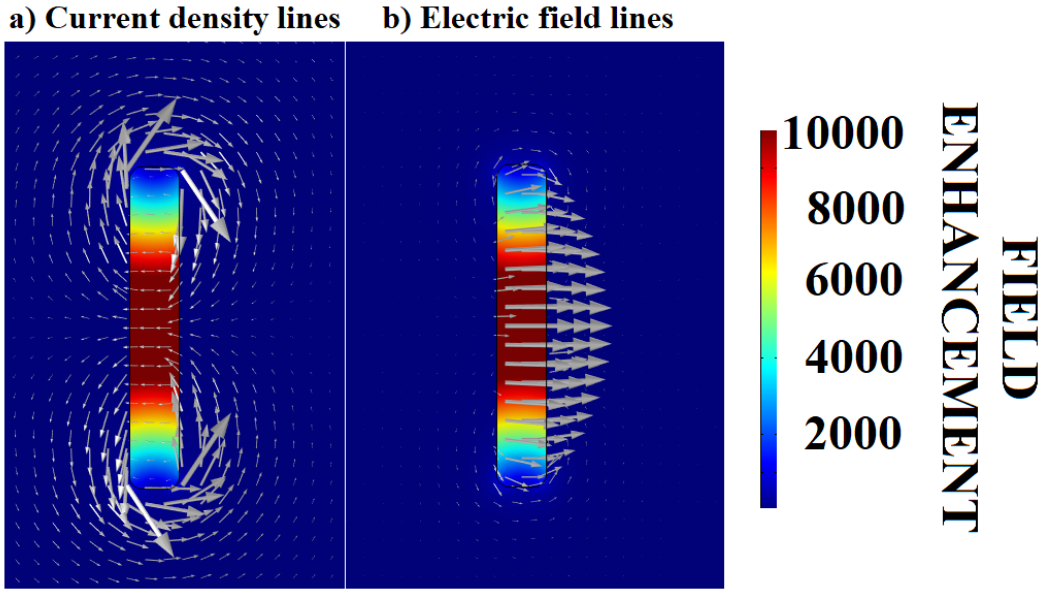

Figure 5.8: Near field distribution of the field intensity enhancement with: a) current density lines and; b) electric field lines. The rod length is 130 nm. The resonant wavelength is 788 nm. The field distribution is plotted in the middle of the gold layer. Color bar or field enhancement means $|E_{TOT}|^2/|E_{IN}|^2$.

In Figure 5.8, near field distribution shows that the strongest field is concentrated in the middle of the rod, and the field becomes weaker as we go to the rod ends. This is similar to rod-shaped ROAs from Chapter 4.2, but the distribution of current density lines is different. In the slot antenna case, current density vector lines go around the slot and are strongest around slot antenna ends. Figure 5.8 b) shows electric field lines with clearly expected transversal orientation.

5.4 L-shaped slot antennas

As was theoretically investigated in Chapter 4.4, we can design an L-shaped nanostructure exhibiting two optical and near-IR spectrum resonances. By shape modification, we are also able to control resonant peaks. If we want to design a slot antenna that exhibits two resonances,

the easiest way is to fabricate a slot antenna with rod-shaped slots of different lengths. Work with polarization-sensitive L-shaped slot structures has already been published [137]. Also, a proposal for the application of L-shaped slot plasmonic structures in three-dimensional nanoscale optical routers has been published [138]. Again, from Figure 5.6, resonance shifting with slot length variation can be observed. The idea is simple: in a gold layer, an array of rod-shaped slots can be fabricated with varying lengths. This would provide different resonances in the spectrum.

Here, we investigate L-shaped slot antennas to make an analogy with the previous investigation. Figure 5.9 presents a top view of the L-shaped slot antenna in the gold layer. One arm length varies while the other is kept constant. The arms are termed A and B. For each wavelength, we increase one of the ROA arm lengths from 90 nm to 120 nm in steps of 10 nm while the other ROA arm is held constant at 75 nm. The polarization direction in all simulation steps is along the arm, which varies as shown in Figure 5.9 (along the x direction). From the near-field distribution, it is noticeable that the field is strongest in the middle of the arms. Therefore, we will calculate field enhancement in two spots, at the middle of the arm with length B and at the center of the area where the L-shaped structure is bent.

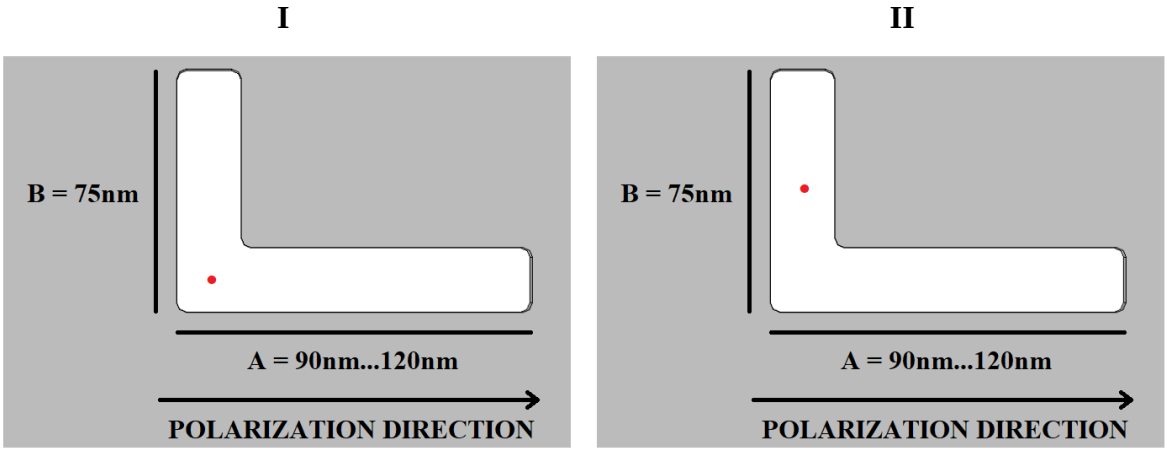

Figure 5.9: Top view of the optical L-shaped slot antenna. Field enhancement is calculated in the red dot in the middle of the gold layer height. I) In case I, the red dot is located at the center of the area where the L-shaped structure is bent. II) In case II, the red dot is located at the center of the shorter arm.

The results for cases I and II from Figure 5.9, presented in Figure 5.10, are similar. The only difference is that for case II, we observe stronger field enhancements.

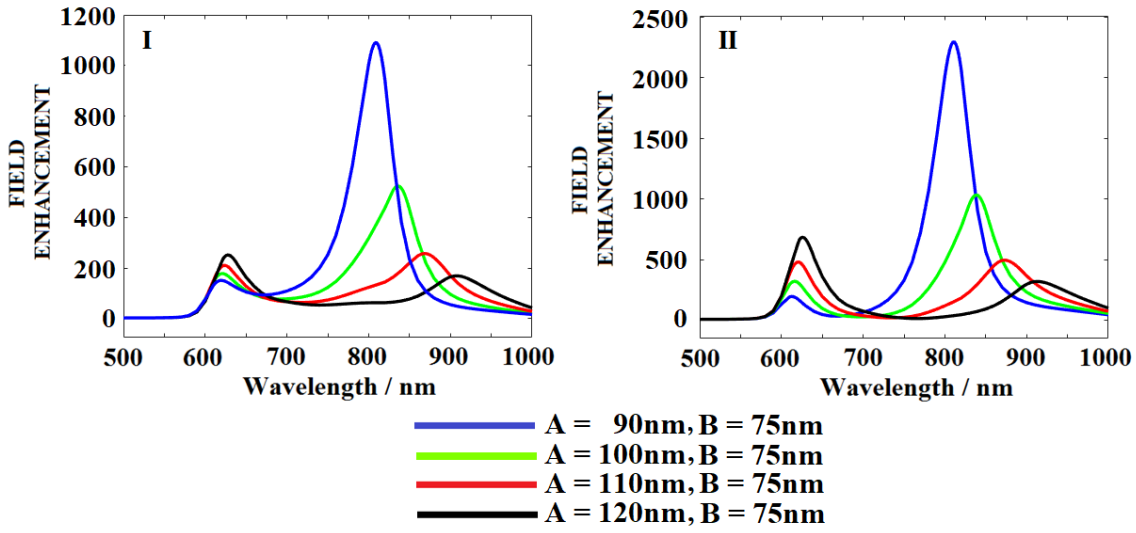

Figure 5.10: Near field optical properties (field enhancement) of L-shaped optical slot antenna with geometry from and for both cases I and II from Figure 5.9

Like in Chapter 4.4, we can see nano-geometry and its correspondent plasmon resonance. Here, the longitudinal current mode shows that its oscillation is pinned to the physical dimension with nodes at the nanorod ends. When we increase the length of one arm, like in Figure 5.6 and Figure 4.17, we observe two resonances that shift both blue (or to the low energy side of the spectral bandwidth) but with increasing wavelength separation between the bimodal resonance wavelengths. In the case of the slot antenna, we are also able to break the symmetry of the nanorod slot and develop the bimodal resonant system.

Another interesting plot for analysis is the current density lines distribution (grey color in Figure 5.11). This is similar to the current mode representation of the asymmetric L-shaped ROAs depicted in Figure 4.18. From the current density, vector representation can be noticed in two distinct modes linked to the bimodal resonances of the L-shaped slot antenna. As is already shown in the analysis of rod-shaped slot antenna in Figure 4.18, current density lines are located around rod-shaped slot antenna ends. For low energy resonance, we can make an analogy with L-shaped ROA where we saw how charge carriers oscillate in phase. The low-frequency L-shaped slot antenna eigenmode can be assigned to a slightly perturbed – bent – eigenmode of rod-shaped slot antenna, giving rise to the antenna resonance at 868 nm. At the same time, high-frequency antenna resonance at 624 nm has a current density lines distribution around antenna ends but also around the area where L-shaped slot arms are bent. If we compare

current density lines in Figure 5.11 c) and Figure 5.11 d), current lines from Figure 5.11 c) give the impression that instead of one L-shaped slot antenna, we have two separated rods close to each other. This is very similar to the investigation in Chapter 4.4 where we had current density lines with opposite signatures, which meant that in resonance, charges oscillate out-of-phase along each individual L-shaped slot antenna arm A and B.

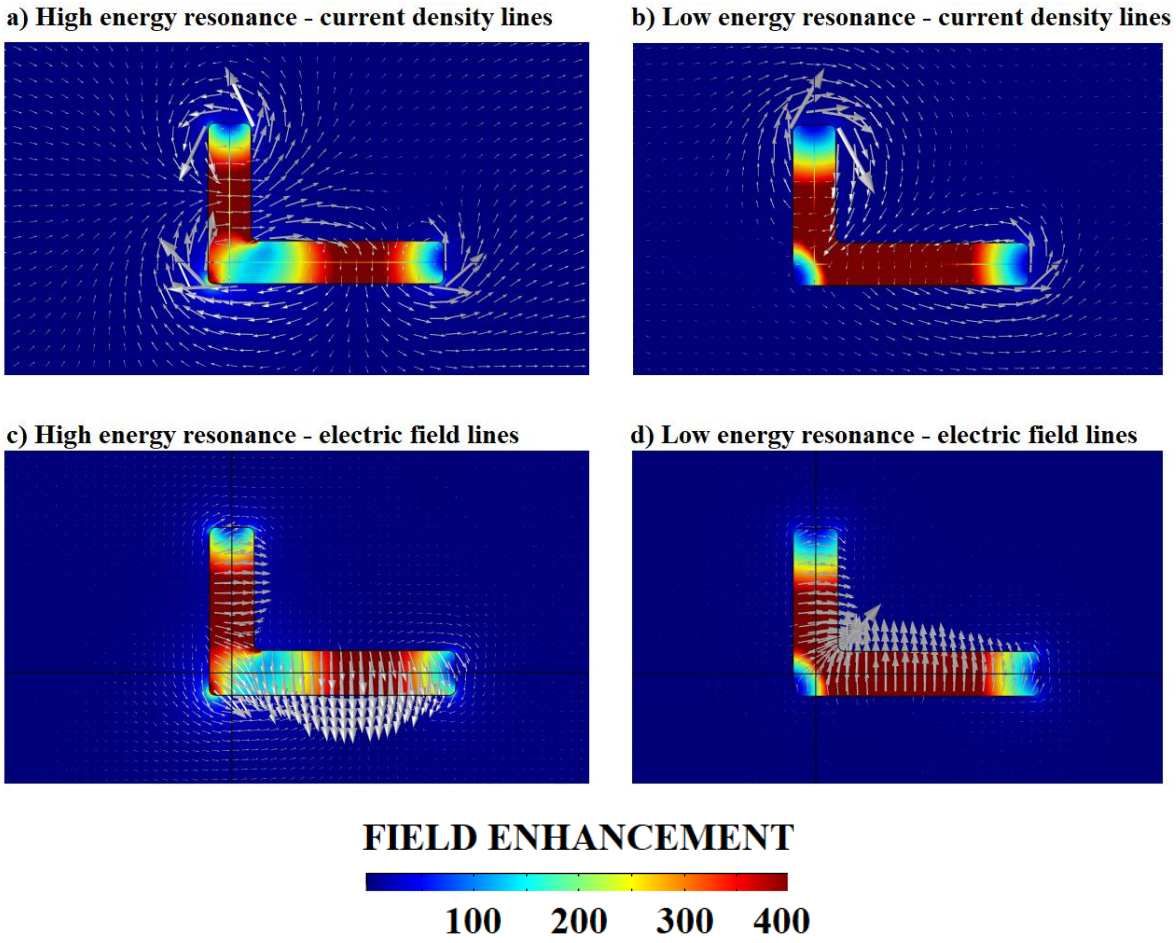

Figure 5.11: Near field distribution of the field intensity enhancement with current density lines. The arm lengths are 110 nm and 75 nm. The resonance wavelengths are: a) and c) 624 nm; b) and d) 868 nm. The field distribution is plotted in the middle of the gold layer. Color bar or field enhancement actually means $|E_{TOT}|^2/|E_{IN}|^2$.

Polarization dependence as a function of frequency can also be analyzed here. We analyze an L-shaped ROA with equal arms, as in Figure 5.12.

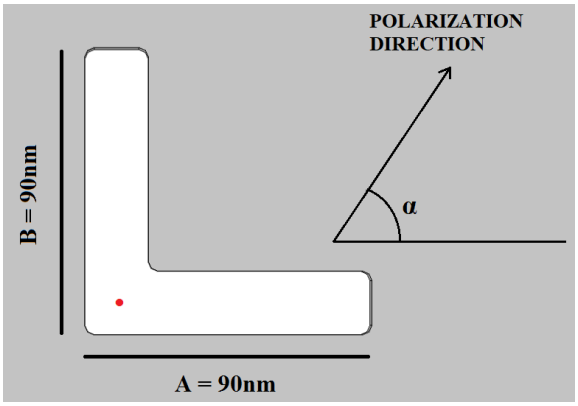

Figure 5.12: Top view of the optical L-shaped slot antenna with equal arms (90 nm). Field enhancement is calculated in the red dot in the middle of the gold layer height at the center of the area where the L-shape structure is bent.

Varying the polarization orientation near field properties can be tuned. Here also, we can observe one interesting behavior which proves the complementary nature of Babinet's principle. In Chapter 4.4, Figures 4.19 and 4.20, we have analyzed which polarization direction should excite certain modes. For L-shaped nanoparticles, we already saw that if we orient polarization in a direction that connects L-shape nanoparticle ends, low energy mode will be excited (green line from Figure 4.20). If we orient polarization in a direction that is perpendicular to the previous direction, high energy mode will be excited (red line from Figure 4.20). As it can be seen in Figure 5.13, here is the opposite situation.

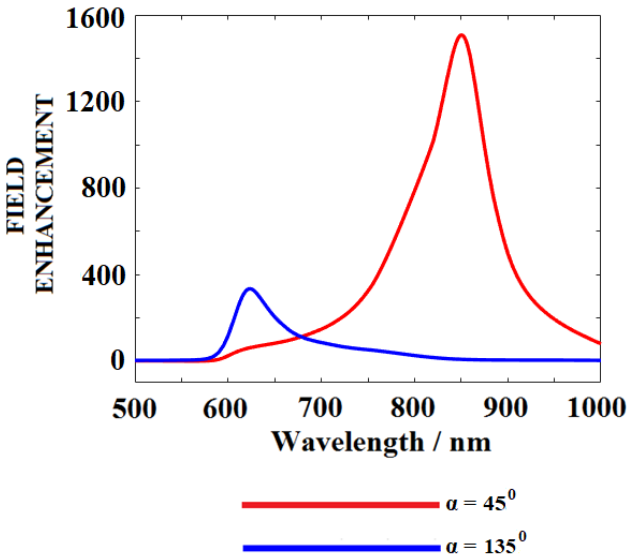

Figure 5.13: Near field optical properties (field enhancement) of L-shaped optical slot antenna with geometry from Figure 5.12 and polarization angles 45^0 and 135^0. For these angles, the corresponding wavelengths are 850 nm and 623 nm.

If we orient polarization to the angle 45° with respect to the x-axis low-frequency mode will be addressed. If we orient polarization to the angle 135° with respect to the x-axis high frequency mode will be addressed.

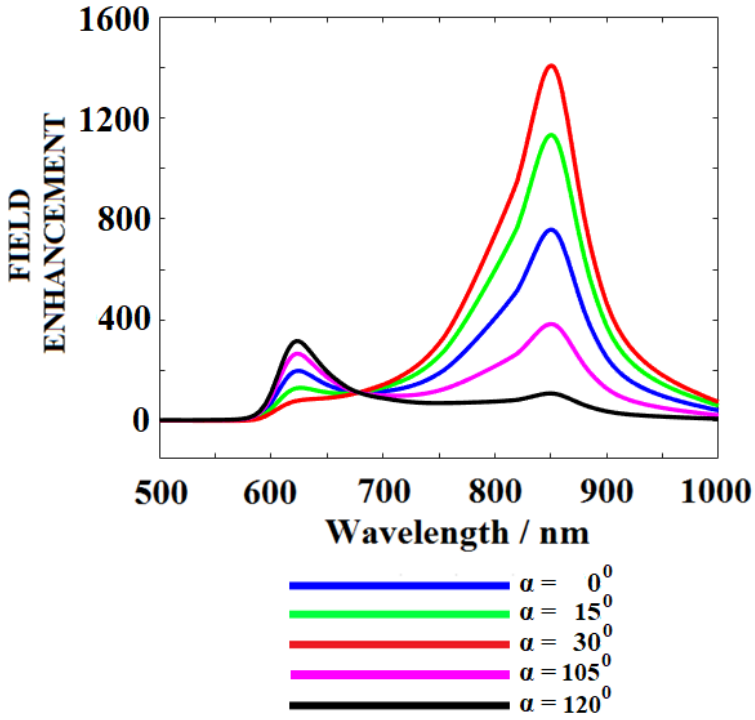

Figure 5.14: Near field optical properties (field enhancement) of L-shaped optical slot antenna with geometry from Figure 5.12 and different polarization angles.

In Figure 5.14, results for other polarization angles are presented. Since this L-shaped slot antenna has equal arms, some polarization angles will yield the same results because of symmetry. For example, results for polarization angles 15^0 and 75^0 will be the same. Same applies for 120^0 and 150^0.

5.5 Cross-shaped slot antennas

Cross-shaped slot nanostructures are very useful to show how these antennas exhibit three resonances, as in Chapter 4.5.5 where we had usual gold cross-shaped nanoparticles. In Figure 5.15, there is a top view of a cross-shaped slot antenna. In this chapter, we will not analyze in detail all types of cross-shaped nanostructures (asymmetric, partially symmetric, etc.); instead, we will immediately start with certain slot antennas that have a three-modal spectral response. But anyway, we will use terms and notations like in Chapter 4.5.5 (A_{LEFT}, A_{RIGHT}, B_{ABOVE}, B_{BELOW}). We will also show the resonant behavior of these structures. While changing the

linear polarization angle, it is possible to control the excitation of all three resonances individually. Of course, not all three resonances are polarization sensitive in the same way in terms of field intensity enhancement. If we observe cross-shaped types from Chapter 4.5, here we will investigate only partially symmetric nanostructures or nanostructures that have symmetric arms just in one direction. Therefore, all simulations will be $B_{ABOVE} = B_{BELOW}$ and $A_{LEFT} \neq A_{RIGHT}$. As mentioned in Chapter 4.5 this analysis can help design multiple plasmon resonant systems used in nano-optical active circuits.

Some geometric parameters are the same as those in the investigation of rod-shaped and L-shaped slot antennas. The width of the arms and the height of the gold layer are constant in all simulations: 20 nm and 70 nm, respectively.

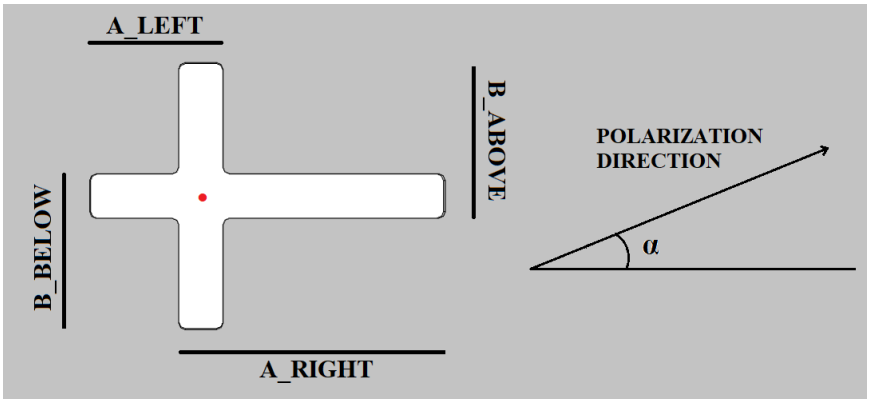

Figure 5.15: Top view of a single cross-shaped slot antenna (x-y plane)

In the first simulation set, we investigate the influence of A_{RIGHT} on spectral response. Figure 5.16 shows the structure that we investigate. All geometrical parameters except A_{RIGHT} are kept constant. As it is shown, the polarization angle will be 60^0 in all simulation steps. Field enhancement is calculated in a red dot in the middle of the gold layer height.

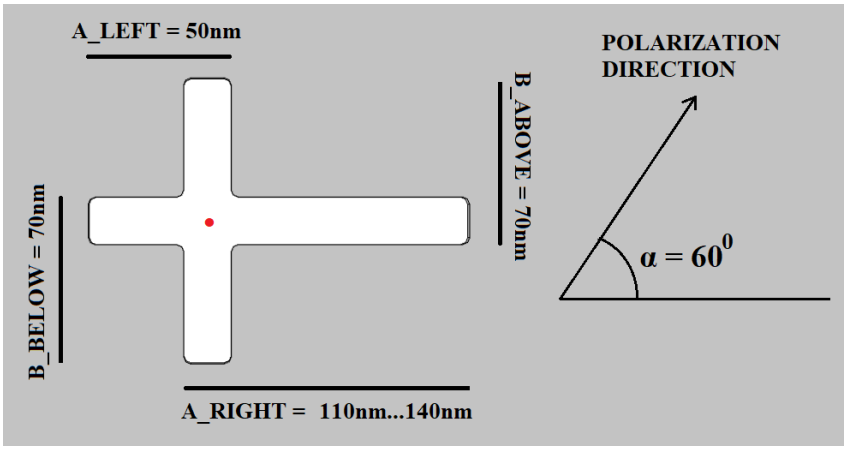

Figure 5.16: Top view of a single cross-shaped slot antenna (x-y plane). A_{RIGHT} varies from 110 nm to 140 nm in 10 nm steps.

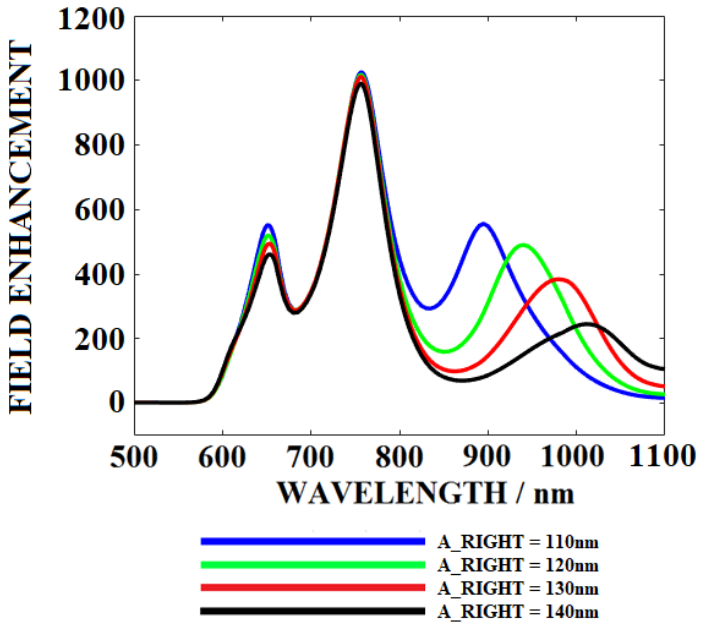

Figure 5.17: Near field optical properties (field enhancement) of cross-shaped optical slot antenna with increasing dimension A_{RIGHT}.

As it can be noticed in Figure 5.17, by variation of A_{RIGHT} practically only the position of the third resonance shifts red. Therefore, in this case, the first two resonances are almost independent. This is very similar to results from Figures 4.49 and 4.50, where we observed far-field properties of triple-modal cross-shaped single ROA. There, we had a polarization angle 30^0.

In the second set of simulations, the variable is A_{LEFT} on spectral response. Figure 5.18 shows the top view of this structure. Like in the previous case, the polarization angle was constant.

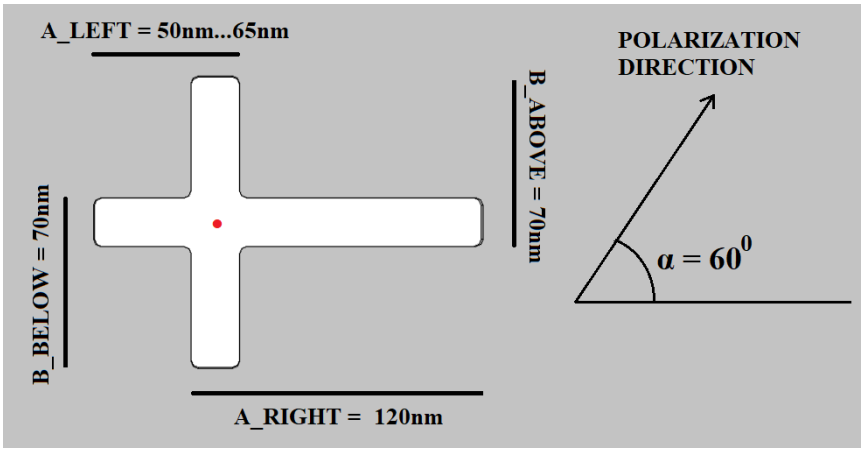

Figure 5.18: Top view of a single cross-shaped slot antenna (x-y plane). $\boldsymbol{A_{LEFT}}$ varies from 50 nm to 65 nm in 5 nm steps.

Figure 5.19 clearly shows the red-shifting of the first resonant wavelength and the very slight red-shifting of the third resonant wavelength. Here, we can say that only the second resonant wavelength is independent in terms of A_{LEFT} influence. We can observe significant red-shifting of the first resonance and very slight red-shifting of the third resonance. This is a very similar investigation to those in Figures 4.45 and 4.46.

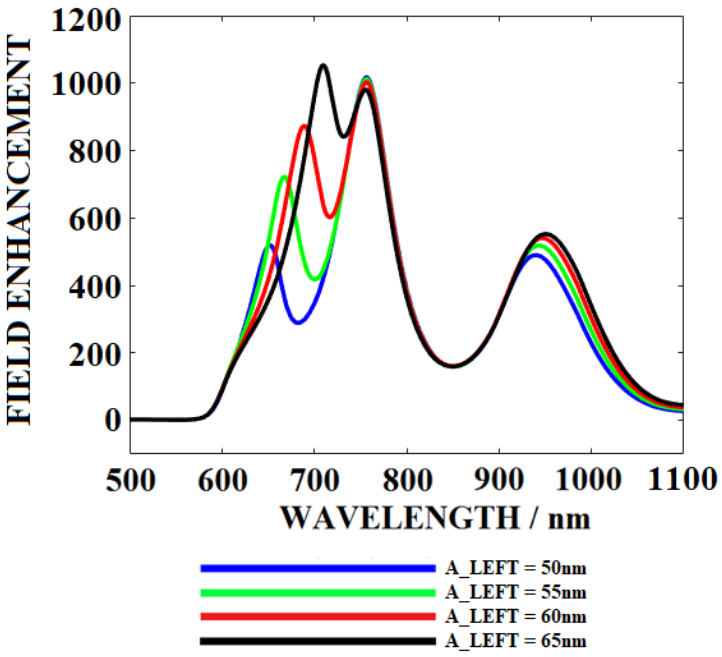

Figure 5.19: Near field optical properties (field enhancement) of cross-shaped optical slot antenna with increasing dimension A_{LEFT}. Field enhancement actually means $|E_{TOT}|^2/|E_{IN}|^2$.

In the next set of simulations, variables are B_{ABOVE} and B_{BELOW} while A_{LEFT} and A_{RIGHT} are constant. Figure 5.20 shows the top view of this structure. Like in the previous case, the polarization angle was constant.

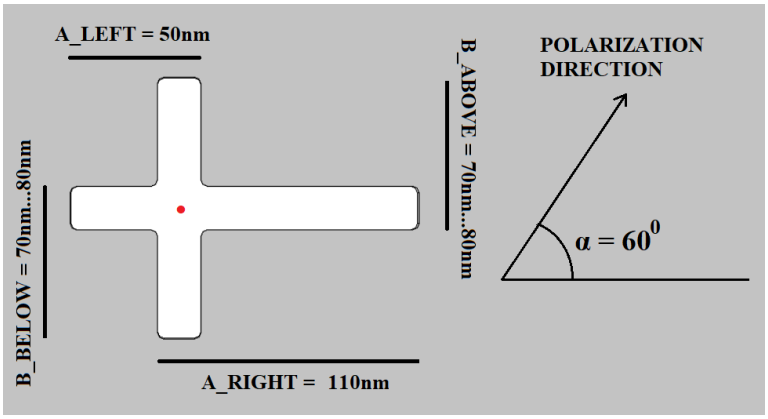

Figure 5.20: Top view of a single cross-shaped slot antenna (x-y plane). B_{ABOVE} and B_{BELOW} vary from 70 nm to 80 nm in 5 nm steps.

Figure 5.21 clearly shows the red-shifting of all three resonances by variation of B_{ABOVE} and B_{BELOW}. If we make an analogy with Figure 4.44, the variation of B_{ABOVE} and B_{BELOW} leads to the variation of all three "parts" of the cross-shaped ROA (blue, green, and red). As was already mentioned in Chapter 4.5.5, the cross-shaped antenna's shorter blue "L-part" from Figure 4.44 can be assigned to the first high-energy resonance, the green "vertical rod-part" from Figure 4.44 can be assigned to the second resonance, and the longer red "L-part" from the Figure 4.44 can be assigned to the third resonance of the cross-shaped ROA. Therefore, an increase of B_{ABOVE} and B_{BELOW} is related to the red-shifting of all three resonances, as Figure 5.21 indicates.

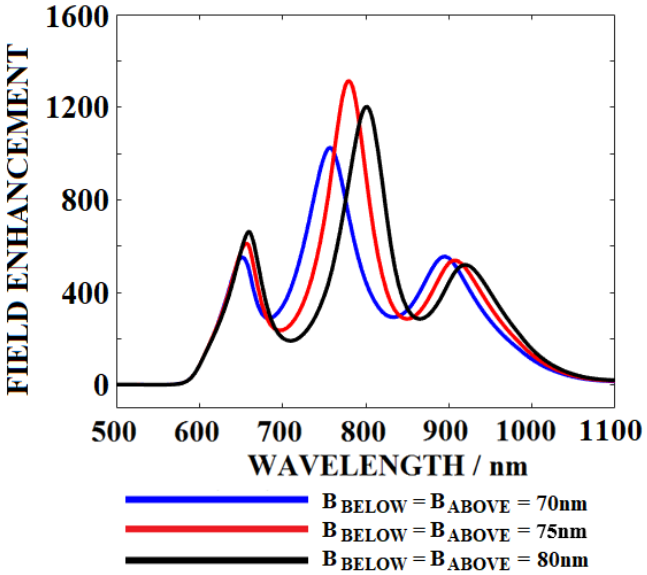

Figure 5.21: Near field optical properties (field enhancement) of cross-shaped optical slot antenna with increasing dimensions B_{ABOVE} and B_{BELOW}. Field enhancement actually means $|E_{TOT}|^2/|E_{IN}|^2$

Like in all other previous cases, this cross-shaped slot antenna structure is polarization-sensitive. Since here we have chosen a partially symmetric structure, it is not necessary to change the full range of polarization angles from 0^0 to 180^0. If we take a look at Figure 5.20, for example, the polarization angle of 15^0 will give the same results as the polarization angle of 165^0,the polarization angle of 30^0 will give the same results as the polarization angle of 150^0, etc.

Therefore, we will investigate near-field properties only for angles between 0^0 and 90^0, but only for angles that show clear triple-modal resonant behaviour. Thus, we choose only the following for angles, as in Figure 5.22.

Finally, Figure 5.23 shows the near-field distributions and current density lines for all three resonances. From a quality point of view, the field distribution is very similar to that in Figure 4.49 in Chapter 4.5.5, where we analyzed triple-modal cross-shaped ROAs and observed those plots as a quasi-combination of rods and L-shaped parts. Moreover, when we observe the current density lines from Figure 5.23 (grey lines), it is a very similar analysis to Figures 5.8 and 5.11, where we discussed rod-shaped and L-shaped slot antennas separately.

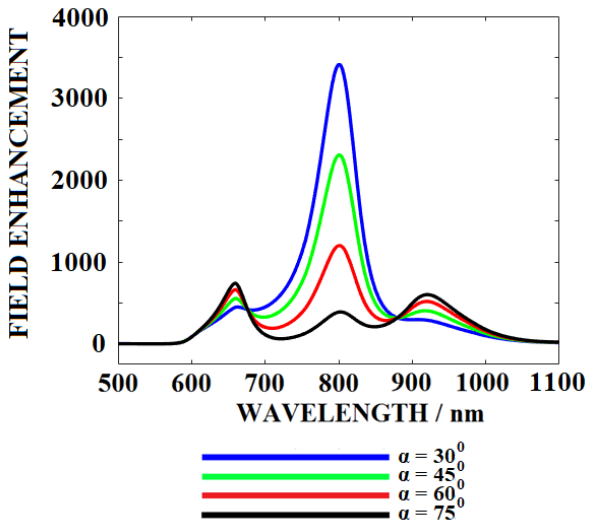

Figure 5.22: Near field optical properties (field enhancement) of cross-shaped optical slot antenna with different polarization angles. Other dimensions are $A_{LEFT} = 50\,nm$, $A_{RIGHT} = 110\,nm$, $B_{ABOVE} = B_{ABOVE} = 80\,nm$. Field enhancement actually means $|E_{TOT}|^2/|E_{IN}|^2$

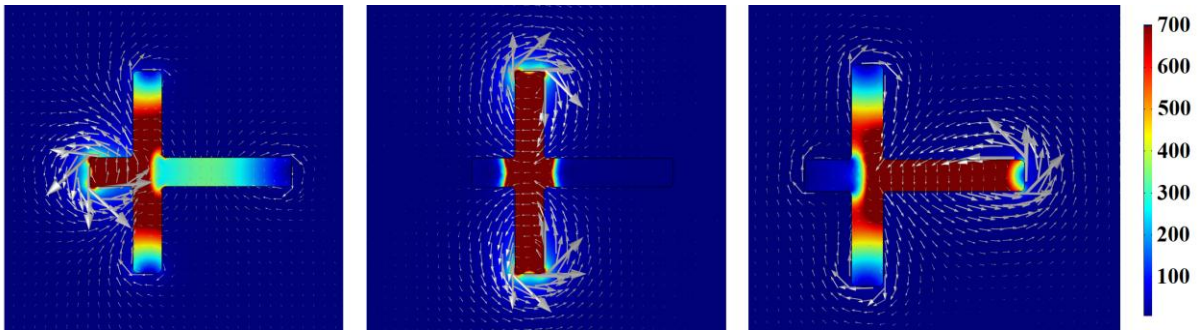

Figure 5.23: Near field distribution of the field intensity enhancement. Dimensions are $A_{LEFT} = 50\,nm$, $A_{RIGHT} = 110\,nm$, $B_{ABOVE} = B_{ABOVE} = 80\,nm$. The resonance wavelengths are 659 nm, 801 nm, and 921 nm. The field distribution is plotted in the middle of the gold layer height. Color bar or field enhancement means $|E_{TOT}|^2/|E_{IN}|^2$. Grey lines are current density lines.

5.6 Discussion about L-shaped and cross-shaped slot antennas

We extend the discussion from Chapters 4.4 and 4.5 on slot versions of these antennas. Chapters 5.3, 5.4, and 5.5 theoretically and numerically show that by changing the slot shape in the gold layer, we can create slot nanostructures that exhibit monomodal, bimodal, and even triple-modal resonance behavior. Like in ROAs investigation, where we always start from rod-shaped ROA, and then by "fusing" concept, we analyze L-shaped and cross-shaped structures; here we started from a rod-shaped slot antenna and observed the transition from rod-shaped to

L-shaped and cross-shaped structure. Like in the overall thesis, the only parameter we changed is the longitudinal length of the slot. Transversal and vertical physical dimensions are kept constant. Following Babinet's principle, we know that the electric field in the case of ROAs and the magnetic field in the case of slot antennas are parallel. This helps us make certain analogies. If we have already proved that electric field lines in the case of ROAs antennas are accommodated between arm ends, magnetic field lines will be accommodated between arm ends in the case of slot antennas. Therefore, current density lines are oriented around arm ends which is shown in several figures. Visual energy reconstruction, like in Figure 4.29, will not be presented. However, based on the vector representation from Figure 5.8, Figure 5.11, Figure 5.23, and resonant wavelengths, we can assume that, in the case of slot antennas, more complex bimodal structures can be designed using a linear combination of two plasmon length basis functions.

Figure 5.11 shows the field and current density lines for an L-shaped slot antenna with "arm" lengths of 110 nm and 75 nm. For this L-shaped slot antenna configuration, the wavelengths of high energy and low energy modes are 624 nm and 868 nm. If we observe Figure 5.11 and the field enhancement distribution along with current density lines, we can say that we found interesting shorter arms (75 nm) and effective lengths of L-shaped slots (110 nm + 75 nm – 20 nm = 165 nm). Numerically, it is found that resonant wavelengths for single rod-shaped antennas with arm lengths of 75 nm and 165 nm are 635 nm and 888 nm, respectively. Therefore, it can also be noticed that the eigenvalue of the high energy mode (which correlates to the wavelength of 624 nm) is blue-shifted with respect to the short, unperturbed rod-shaped slot antenna of length 75 nm (which correlates to the wavelength of 638 nm). Like in Chapter 4.4, where we discussed L-shaped ROAs, here it is also clear that the plasmon length of the L-shaped slot antenna defining the low energy eigenmode is shorter compared to the 165 nm (wavelength 868 nm corresponds to the rod-shaped slot antenna with length 156 nm).

Here, we will also make a short analogy between cross-shaped ROAs and cross-shaped slot antennas. Cross-shaped ROAs have already been discussed in 4.5.6. Following the analogy between ROAs and slot antennas, cross-shaped slot antennas could also be observed as a combination of rod-shaped slot antennas. The only parameter we changed during the investigation is length. As in the L-shaped slot antenna case, it applied vector representation of the current flow, which is helpful in understanding how the single-mode rod-shaped slot antenna structure develops into the bimodal and triple-modal cross-shaped slot antenna

structure. By using the plasmon length basis function, we can build multi-modal blocks. As can be seen, if we compare Chapters 4.5, 4.5.5, and 5.5, in the case of cross-shaped slot antennas, we did not perform a full investigation as we did for cross-shaped ROAs but instead started from the triple-modal structure, which is sufficient to demonstrate that it is possible to reconstruct the eigenmodes of the cross-shaped slot antenna using the plasmon length basis functions of the rod-like slot antenna. In Chapter 4.4, it was shown that the plasmon lengths of the cross-shaped ROA with arm lengths 60 nm and 80 nm defining the high energy eigenmode and the low energy mode is significantly shorter compared to the plasmon length of 60 nm and 80 nm individual gold nanorods, respectively. The principle here is the same. Here, we choose two rod-shaped slot antennas with 100 nm and 130 nm lengths. It is numerically found that the resonant wavelengths for the rod-shaped slot antennas with lengths of 100 nm and 130 nm are 704 nm and 788 nm, respectively. To perform the same analysis as in the cross-shaped ROA case, we will perform just one simulation run to the show near-field properties of the symmetric cross-shaped slot antenna with arms 100 nm and 130 nm, as shown in Figure 5.24. The polarization angle is 30^0.

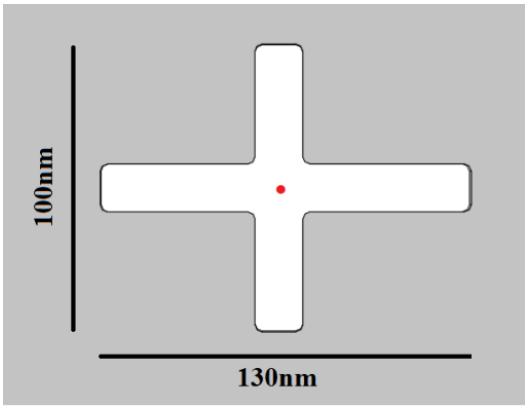

Figure 5.24. Top view of a single cross-shaped slot antenna (x-y plane) with symmetric arms.

This slot antenna exhibits two resonances with wavelengths of 684 nm and 775 nm. These two wavelengths correspond to the rod-shaped slot antennas with lengths of 97 nm and 124 nm. The blue-shifting of resonances in the case of the cross-shaped slot antenna, compared to the resonances of a single rod-shaped slot antenna with the same arm length, can, as discussed in Chapter 4.5.1, also be interpreted as a perturbation, thus shortening the plasmon length of the rod-shaped slots from which the cross-shaped slot antenna is composed in comparison to the original rod-shaped slot antenna.

6 Conclusions

Resonant optical antennas (ROAs) are nanodevices that can enhance the electromagnetic field in their vicinity and scatter the light in the far field. The improved field is localized in a subdiffraction-limited volume. Their ability to exhibit strong field enhancement in the gap makes them suitable for coupling with quantum emitters. This thesis contributes to a better understanding of how the resonant behavior can be controlled effectively with geometrical parameters deviation and polarization setup. Several types of bimodal antennas have established scaling laws in the form of equations that relate resonant wavelengths and geometrical parameters. Since every geometrical parameter influences the resonant behavior, it is difficult to obtain an equation that combines all geometrical parameters. Thus, the main geometrical parameter under investigation was the length or longitudinal parameter. In this work, the behavior of ROA nanoantennas was both investigated and optimized using numerical via finite element method (FEM) using commercial software package COMSOL Multiphysics.

In this context, novel ROA designs have been studied to explore their ability to enhance and manipulate electromagnetic fields at the nanoscale. The first design is based on L-shaped nano-antennas. The reported designs exhibit monomodal and bimodal resonance behavior with a high field enhancement of 40 for high energy and 147.3 for low energy resonance. By changing the length of the antenna, the mode resonances can be tuned. Further, the polarization sensitivity and tunable nature of these designs enhance their versatility, allowing for selective excitation of different resonance modes based on the polarization angle. The second design is based on coupled cross-shaped exhibits, with a field enhancement of 45.9 for the high-energy resonance and 149.4 for the low-energy resonance, respectively, on the $|E_{TOT}|/|E_{IN}|$ scale.

On the other hand, plasmonic slot antennas also show significant field enhancement. In this work, the gap width of the coupled nanoantennas was 2 nm, and the width of the slot antennas was 20 nm. Therefore, field enhancements of nanoantennas and their slot counterparts should not be compared. However, it is worth mentioning that on the $|E_{TOT}|^2/|E_{IN}|^2$ scale L-shaped slot ROAs also exhibit bimodal resonance behavior with a field enhancement of 350 for the high energy and 1000 for the low energy on $|E_{TOT}|^2/|E_{IN}|^2$ scale for dimensions A = 100 nm and B = 75 nm as Figure 5.10 shows. These field enhancement levels are much higher than it was shown for L-coupled ROAs with 20 nm gap-width from Figure 4.25. An interesting conclusion is that cross-shaped slot ROAs show three modes when we observe field enhancement. Results are in Figures 5.17, 5.19, 5.21, 5.23. These figures show that different

wavelength separations between resonant peaks come with different geometrical parameters and polarization conditions. As it was seen, there are several options to perform this analysis like changing A_{LEFT}, A_{RIGHT} or both in the same time B_{ABOVE} and B_{ABOVE}. We will choose antenna from Figure 5.16 and 5.17 where A_{RIGHT} is changing. For geometrical dimension $A_{RIGHT} = 110nm$. On $|E_{TOT}|^2/|E_{IN}|^2$ scale cross-shaped slot antennas exhibit field enhancements of 580, 1020, and 585 for the high-energy resonance, medium-energy resonance, and the low-energy resonance, respectively. Both types also show polarization sensitivity. As in the L-shaped slot antenna case, these field enhancement levels are much higher than those shown for cross-coupled ROAs with a 20nm gap-width from Figure 4.40.

The findings of this thesis open up new avenues for the design of multiple plasmon resonance devices that offer ultra-high field enhancement, crucial for various applications in quantum optics, sensing, and nano-scale photonic systems. The novel ROA designs reported in this thesis provide a solid foundation for future research and development in nanoantenna-based technologies, with the potential for integration into next-generation nano-optical circuits operating at multiple frequencies.

Future work

Although a comprehensive study of the proposed designs was executed in this thesis, other aspects of the structure are still to be discovered. Machine learning techniques could optimize antenna designs and increase electric field enhancement more efficiently by predicting resonance behaviors and identifying design parameters for improved performance. Employing new plasmonic materials with lower losses, such as transition metal nitrides, may extend functionality across different wavelength ranges and improve thermal stability. Additionally, enhancing multi-modal designs for sensing applications, particularly in refractive index sensing or molecular detection, would expand their practical use. Lastly, the real-time tunability of these structures will be explored using phase-change materials or graphene, which could be interesting in many applications.

Abbreviations

VIS – visible

NIR – near infrared

OSC – organic solar cells

CPU – central processing unit

THz – terahertz

EM – electromagnetic

NP – nanoparticle

SPP – surface plasmon polariton

UV – ultraviolet

DDA – discrete dipole approximation

LSPR – localized surface plasmon resonance

TE – transversal electric mode

TM – transversal magnetic mode

ε_r – relative dielectric permittivity

ε_{xy} – component of dielectric function

ε_0 – vacuum permittivity

δ_{xy} – Kronecker delta

ω – angular frequency

k – wave number

$k_{x,y}$ – wave number components

μ_r – relative magnetic permeability

μ_{xy}– component of magnetic permeability

μ_0 – vacuum of free space permeability

$\vec{r}$ – position in 3D space where we calculate some physical value

$\vec{E}(\vec{r},t)$ – electric field vector

$\vec{B}(\vec{r},t)$ – magnetic flux density

$\vec{H}(\vec{r},t)$ – magnetic field vector

$\vec{D}$ - electric displacement field vector

$\vec{J}_e$ - free current density

$\rho_e(\vec{r},t)$ – volume charge density in space and time

λ – wavelength

τ – relaxation time

γ – collision frequency or damping rate

$\vec{J}$ – current density

σ – electrical conductivity

$\vec{e}_x$ – unit vector in x direction

m_e – effective mass of electron

m_b – effective mass of bound electron

e – electric charge of electron

x – electron displacement

v - velocity

ω_0 – natural frequency

ω_p – plasma frequency

$\vec{p}$ - electric dipole momentum inside material

n - volume concentration of charge carriers

$\vec{P}$ – macroscopic polarization

$\bar{n}$ – complex refractive index

k_{SPRING} – spring constant of the oscillator

f – frequency

f_j - oscillator strength

$I(x)$ - beam intensity in x direction

α_{coef} – attenuation coefficient

r – radius of nanoparticle

ψ_i, ξ_i - Riccati-Bessel functions

V – volume of nanoparticle

ε_{metal} – relative dielectric permittivity of the metal

ε_{medium} - relative dielectric permittivity of the dielectric of surrounding medium

$Q_{scattering}$ – scattered light

$Q_{absorption}$ – absorbed light

α_{sphere} – polarizability of nanoparticle

e_{factor} – ellipsoid factor

$\vec{I}$ – current vector

$d\vec{l}$ – infinitesimal length vector

$\vec{S}$ - Poynting vector

P_S – average radiated power

$\vec{P}_{DENSITY}$ – power density

$P_{rad\_isotropic}$ – radiated power of isotropic source

D – directivity

P_{rad} – radiated power

$\eta_{RADIATION\_EFF}$ – radiation efficiency

η_{TOTAL_EFF} – total efficiency

$P(\lambda, T)$ - Planck's law for black body radiation

T – temperature of the black body

h – Planck's constant

c – speed of light in vacuum

k - Boltzmann constant

$G(\theta, \phi)$ – gain

Z – impedance

RF – radio frequency

X – imaginary part of impedance (reactance)

V – voltage of transmission line

C – capacitance

S – surface

W – width

H – height

δ - skin depth

k - imaginary part of refractive index

P_{abs} - absorbed power of the antenna

Q – quality factor

k_{SPP} – wave number of surface plasmon polaritons

FDTD - finite difference time domain method

FEM - finite element method

ITO – indium tin oxide

ROA – resonant optical antenna

GAP – gap width

3D – three dimensional

eV – electron volt

α – angle

V_{geom} – volume

S_{11} – reflection scattering parameter

List of Figures

Figure 4.36: (a) Top view of a single asymmetric cross-shaped ROA (x-y plane) with the antenna arms termed A and B; b) 3D model of the single cross-shaped ROA

Figure 4.37: Far field properties for geometry from Figure 4.36.

Figure 4.38: The current density of a partially symmetric ROA at the existing three resonances of 630nm, 698nm and 768nm, respectively.

Figure 4.39: a) Top view of a coupled cross-shaped ROA (x-y plane) with equal antenna arms termed A and B where arm B is moved in δx steps in x-direction; b) 3D model of the coupled-cross-shaped ROA.

Figure 4.40: Field enhancement $|E_{TOT}|^2/|E_{IN}|^2$ in the gap center for different values of δ_x and gap width of 20nm.

Figure 4.41: a) current density of the bimodal ROA for resonant wavelengths for $\delta_x = 10nm$. The ROA resonant wavelengths are 730nm and 767nm; b) current density of the bimodal ROA for resonant wavelengths for $\delta_x = 20nm$. The ROA resonant wavelengths are 736nm and 815mm.

Figure 4.42: Field enhancements $|E_{TOT}|^2/|E_{IN}|^2$in the gap center for several values of gap and constant shifting value of $\delta_x = 25nm$.

Figure 4.43: a) Top view of a coupled cross-shaped ROA (x-y plane) with equal antenna arms one arm Bis moved in δx steps in x-direction; b) 3D model of the coupled-cross-shaped ROA; c) Field enhancement $|E_{TOT}|/|E_{IN}|$ in the gap center for different values of δx and gap width of 2nm; d) current density of the bimodal ROA for resonant wavelengths for δx=15nm; (e) field enhancements $|E_{TOT}|/|E_{IN}|$ in the gap center for several values of gap and constant shifting value of δx=15nm.

Figure 4.44: A partially symmetric cross-shaped antenna can be regarded as composed of two L-shaped antennas (shown in blue and red) and one rod-like antenna (shown in green).

Figure 4.45: Top view of a single cross-shaped ROA (x-y plane) with different antenna arms where A_{LEFT} from 30nm to 60nm in 5nm steps.

Figure 4.46: Far-field properties of single asymmetric cross-shaped ROAs with changing arm length in the left direction (A_{LEFT}). a) absolute absorption cross section of ROA; b) absolute scattering cross section of ROA.

Figure 4.47: Current densities of the resonances for resonant wavelengths 670nm, 814nm and 910nm for $A_{LEFT} = 40$ nm. The color bar represent j (current density) with the vector representation of the current modes for the partially symmetric cross-shaped configuration.

Literature

[1] S. A. Maier, *Plasmonics: Fundamentals and Applications*. Springer, 2007.

[2] P. Mühlschlegel, H.-J. Eisler, O. J. F. Martin, B. Hecht, and D. W. Pohl, "Resonant optical antennas," *Science*, vol. 308, no. 5728, pp. 1607–1609, 2005.

[3] P. Bharadwaj, B. Deutsch, and L. Novotny, "Optical antennas," *Advances in Optics and Photonics*, vol. 1, no. 3, pp. 438–483, 2009.

[4] P. Biagioni, J.-S. Huang, and B. Hecht, "Nanoantennas for visible and infrared radiation," *Reports on Progress in Physics*, vol. 75, no.2, pp. 024402, 2012.

[5] J. Kern, R. Kullock, J. Prangsma, M. Emmerling, M. Kamp, and B. Hecht, "Electrically driven optical antennas," *Nature Photonics*, vol. 9, no. 9, pp. 582–586, 2015.

[6] A. G. Curto, G. Volpe, T. H. Taminiau, M. P. Kreuzer, R. Quidant, and N. F. van Hulst, "Unidirectional emission of a quantum dot coupled to a nanoantenna," *Science*, vol. 329, no. 5994, pp. 930–933, 2010.

[7] T. H. Feichtner, O. Selig, and B. Hecht, "Plasmonic nanoantenna design and fabrication based on evolutionary optimization," *Optics Express*, vol. 25, no. 10, pp. 10828-10842, 2017.

[8] K. L. Kelly, E. Coronado, L. L. Zhao, and G. C. Schatz, "The optical properties of metal nanoparticles: The influence of size, shape, and dielectric environment," *The Journal of Physical Chemistry B*, vol. 107, no. 3, pp. 668–677, 2003.

[9] E. Ringe, M. R. Langille, K. Sohn, J. Zhang, J. Huang, C. A. Mirkin, R. P. V. Duyne, and L. D. Marks, "Plasmon length: A universal parameter to describe size effects in gold nanoparticles," *The Journal of Physical Chemistry Letters*, vol. 3, no. 11, pp. 1479–1483, 2012.

[10] L. Novotny and B. Hecht, Principles of Nano-Optics. Cambridge University Press, 2006.

[11] D. K. Gramotnev and S. I. Bozhevolnyi, "Plasmonics beyond the diffraction limit," *Nature Photonics*, vol. 4, no. 2, pp. 83–91, 2010.

[12] N. P. de Leon, B. J. Shields, C. L. Yu, D. E. Englund, A. V. Akimov, M. D. Lukin, and H. Park, "Tailoring Light-Matter Interaction with a Nanoscale Plasmon Resonator," *Physical Review Letters*, vol. 108, no. 22, pp. 226803, 2012.

[13] A. G. Curto, T. H. Taminiau, G. Volpe, M. P. Kreuzer, R. Quidant, and N. F. van Hulst, "Multipolar radiation of quantum emitters with nanowire optical antennas," *Nature Communications*, vol. 4, no. 1, pp. 1750, 2013.

[14] J. A. Schuller, E. S. Barnard, W. Cai, Y. C. Jun, J. S. White, and M. L. Brongersma, "Plasmonics for extreme light concentration and manipulation," *Nature Materials*, vol. 9, no. 3, pp. 193–204, 2010.

[15] V. Giannini, A. I. Fernández-Domínguez, S. C. Heck, and S. A. Maier, "Plasmonic nanoantennas: Fundamentals and their use in controlling the radiative properties of nanoemitters," *Chemical Reviews*, vol. 111, no. 6, pp. 3888–3912, 2011.

[16] P. Nordlander, C. Oubre, E. Prodan, K. Li, and M. I. Stockman, "Plasmon Hybridization in Nanoparticle Dimers," *Nano Letters*, vol. 4, no. 5, pp. 899–903, 2004.

[17] J. Aizpurua, G. W. Bryant, L. J. Richter, F. J. García de Abajo, B. K. Kelley, and T. Mallouk, "Optical properties of coupled metallic nanorods for field-enhanced spectroscopy," *Physical Review B*, vol. 71, no. 23, pp. 235420, 2005.

[18] N. J. Halas, S. Lal, W.-S. Chang, S. Link, and P. Nordlander, “Plasmons in strongly coupled metallic nanostructures,” *Chemical Review*, vol. 111, no. 6, pp. 3913–3961, 2011.
[19] S. Palomba and L. Novotny, “Nonlinear excitation of surface plasmon polaritons by four-wave mixing,” *Physical Review Letters*, vol. 101, no. 5, pp. 056802, 2008.
[20] K. Kneipp, Y. Wang, H. Kneipp, L. T. Perelman, I. Itzkan, R. R. Dasari, and M. S. Feld, “Single Molecule Detection Using Surface-Enhanced Raman scattering (SERS),” *Physical Review Letters*, vol 78, no. 9, pp. 1667–1670, 1997.
[21] H. A. Atwater and A. Polman, “Plasmonics for improved photovoltaic devices,” *Nature Materials*, vol. 9, no. 3, pp. 205–213, 2010.
[22] J. Zhang, J. Yang, X. Wu, and Q. Gong, “Electric field enhancing properties of the V-shaped optical resonant antennas,” *Optics Express*, vol. 15, no. 25, pp. 16852–16859, 2007.
[23] D.P. Fromm, A. Sundaramurthy, P.J. Schuck, G. Kino, and W.E. Moerner, “Gap-Dependent Optical Coupling of Single “Bowtie” Nanoantennas Resonant in the Visible,” *Nano Letters*, vol. 4, no. 5, pp. 957 – 961, 2004.
[24] T. Kosako, Y. Kadoya, and H.F. Hofmann, “Directional control of light by a nano-optical Yagi-Uda antenna,” *Nature Photonics*, vol. 4, no. 5, pp. 312-315, 2010.
[25] H. Husu, J. Mäkitalo, J. Laukkanen, M. Kuittinen, and M. Kauranen, "Particle plasmon resonances in L-shaped gold nanoparticles," *Optics Express*, vol. 18, no. 16, pp. 16601-16606, 2010.
[26] J. Yang and J. Zhang, “Subwavelength Quarter-Waveplate Composed of L-Shaped Metal Nanoparticles,” *Plasmonics*, vol. 6, no. 2, pp. 251–254, 2011.
[27] P. R. Wiecha, L.-J. Black, Y. Wang, V. Paillard, C. Girard, O. L. Muskens, and A. Arbouet, “Polarization conversion in plasmonic nanoantennas for metasurfaces using structural asymmetry and mode hybridization,” *Scientific Reports*, vol. 7, no. 1, pp. 40906, 2017.
[28] S. Chen, L. Zeng, J. Li, J. Weng, J. Li, Z. Guo, P. Xu, W. Liu, J. Yang, Y. Qin, and K. Wen, “Tunable plasmon-induced transparency with coupled L-shape graphene metamaterial”, *Results in Physics*, vol. 38, pp. 105537, 2022.
[29] J. Yang and J. Zhang, “Nano-polarization-converter based on magnetic plasmon resonance excitation in and L-shaped slot antenna,” *Optics Express*, vol. 21, no. 7, pp. 7934 – 7942, 2013.
[30] Y.Bai, L.Zhao, D.Ju, Y.Jiang, and L.Liu, “Wide-angle, polarization-independent and dual-band infrared perfect absorber based on L-shaped metamaterial,” *Optics Express*, vol. 23, no.7, pp. 8670-8680, 2015.
[31] Y. Jing, Z. Jia-Sen, W. Xiao-Fe, and G. Qi-Huang, “Resonant modes of L-shaped gold nanoparticles,” *Chinese Physics Letters*, vol. 26, no. 6, pp. 067802, 2009.
[32] A. Tahir, S. A. Schulz, I. D. Leon, and R. W. Boyd, “Design principles for wave plate metasurfaces using plasmonic L-shaped nanoantennas,” *Journal of Optics*, vol. 19, no. 3, pp. 035001, 2017.
[33] Y. Miao, R. C. Boutelle, A. Blake, V. Chandrasekaran, C. J. Sheehan, J. Hollingsworth, D. Neuhauser, and S. Weiss, “Super-resolution imaging of plasmonic near-fields: overcoming emitter mislocalizations,” *The Journal of Physical Chemistry Letters*, vol. 13, no. 20, pp. 4520–4529, 2022.
[34] L. J. Black, P. R. Wiecha, Y. Wang, C. H. Groot, V. Paillard, C. Girard, O. L. Muskens, and A. Arbouet, “Tailoring second-harmonic generation in single L-shaped plasmonic

nanoantennas from the capacitive to conductive coupling regime," *ACS Photonics*, vol. 2, no. 11, pp. 1592–1601, 2015.
[35] W. Wang, Z. Guo, Y. Sun, F. Shen, Y. Li, Y. Lio, X. Wang, and S. Qu, "Ultra-thin optical vortex phase plate based on the L-shaped nanoantenna for both linear and circular polarized incidences," *Optics Communications*, vol. 355, pp. 321–325, 2015.
[36] N. Bralović, U. Lemmer, and M. Hussein, "Asymmetric L-shaped resonant optical antennas with plasmon length tuning and high-electric field enhancement," *Optical and Quantum Electronics*, vol. 55, no. 9, pp. 824, 2023.
[37] P. Biagioni, M. Savoini, J.-S. Huang, L. Duò, M. Finazzi, and B. Hecht, "Near-field polarization shaping by a near-resonant plasmonic cross antenna," *Physical Review B*, vol. 80, no. 15, pp. 153409, 2009.
[38] P. Biagioni, X. Wu, M. Savoini, J. Ziegler, J.-S. Huang, L. Duò, M. Finazzi, and B. Hecht, "Tailoring the interaction between matter and polarized light with plasmonic optical antennas," *Proceedings of SPIE*, vol. 7922, pp. 79220C, 2011.
[39] J. Trevino, G. F. Walsh, E. F. Pecora, S. V. Boriskina, and L. Dal Negro, "Photonic–plasmonic-coupled nanoantennas for polarization-controlled multispectral nanofocusing," *Optics Letters*, vol. 38, no. 22, pp. 4861-4863, 2013.
[40] N. Bralović, U. Lemmer, and M. Hussein, "Asymmetric Cross-Shaped Optical Antennas with Wide Spectral Tunability and High Optical Cross-Sections," *Plasmonics*, vol. 19, no. 1, pp. 179-191, 2023.
[41] L. Lin and Y. Zheng, "Optimizing plasmonic nanoantennas via coordinated multiple coupling," *Scientific Reports*, vol. 5, no. 1, pp. 14788, 2015.
[42] U. K. Khalil, W. Farooq, J. Iqbal, S. Z. U. A. Kazmi, A. D. Khan, A. U. Rehman, and S. Ayub, "Design and optimization of bowtie nanoantenna for electromagnetic field enhancement," *The European Physical Journal Plus*, vol. 136, no. 7, pp. 754, 2021.
[43] V. Veselago, "The Electrodynamics of substances with simultaneously negative values of $\boldsymbol{\varepsilon}$ and μ," *Soviet Physics Uspekhi*, vol. 10, no. 4, pp. 504, 1968.
[44] J. C. Maxwell, "A dynamical theory of the electromagnetic field," *Philosophical Transactions of the Royal Society*, vol. 155, pp. 459-512, 1865.
[45] P. Mulvaney, "Surface Plasmon Spectroscopy of Nanosized Metal Particles," *Langmuir*, vol. 12, no. 3, pp. 788–800, 1996.
[46] I. R. Hooper, J. R. Sambles, "Dispersion of surface plasmon polaritons on short-pitch metal gratings," *Physical Review B*, vol. 65, no. 16, pp. 165432, 2002.
[47] Y. Fang, M. Sun, "Nanoplasmonic waveguides: towards applications in integrated nanophotonic circuits," *Light: Science & Applications*, vol. 4, no. 6, pp.294, 2015.
[48] A. V. Zayats, I. I. Smolyaninov, and A. A. Maradudin, "Nano-optics of surface plasmon polaritons," *Physics Reports*, vol. 408, no. 3, pp. 131-314, 2005.
[49] T. Thio, K. M. Pellerin, R. A. Linke, H. J. Lezec, and T. W. Ebbesen, "Enhanced light transmission through a single subwavelength aperture," *Optics Letters*, vol. 26, no. 24, pp. 1972-1974, 2001.
[50] P. Drude, "Zur Elektronentheorie der Metalle," *Annalen der Physik*, vol. 306, no. 3, pp. 566–613, 1900.
[51] P. B. Johnson and R. W. Christy, "Optical Constants of the Noble Metals," *Physical Review B*, vol. 6, no. 12, pp. 4370–4379, 1972.
[52] E. D. Palik, *Handbook of optical constants of solids*, vol. 3. Academic press, 1998.
[53] J. Kraus and R. Marhefka, *Antennas For All Applications*. McGraw-Hill, 2002.
[54] C. A. Balanis, *Antenna Theory: Analysis and Design*. Wiley-Interscience, 2005.
[55] W. Stutzman and G. Thiele, *Antenna Theory and Design*. Wiley, 2012.

[56] L. D. Landau, E. M. Lifshitz, und L. P. Pitaevskii, *Electrodynamics of continuous media*, Vol. 8 in Course of theoretical physics, 2000.
[57] J. A. Stratton and L. J. Chu, "Diffraction theory of electromagnetic waves," *Physical Review*, vol. 56, no. 1, pp. 99–107, 1939.
[58] G. A. E. Vandenbosch and Z. Ma, "Upper bounds for the solar energy harvesting efficiency of nano-antennas," *Nano Energy*, vol. 1, no. 3, pp. 494-502, 2012.
[59] A. A. Oliner, "Historical Perspectives on Microwave Field Theory," *IEEE Transactions on Microwave Theory and Techniques*, vol. 32, no. 9, pp. 1022–1045, 1984.
[60] M. Mazilu and K. Dholakia, "Optical impedance of metallic nano-structures," *Optics Express*, vol. 14, no. 17, pp. 7709-7722, 2006.
[61] R. L. Olmon and M. B. Raschke, "Corrigendum: Antenna–load interactions at optical frequencies: impedance matching to quantum systems," *Nanotechnology*, vol. 24, no. 22, pp. 229501, 2013.
[62] P. Grimm, G. Razinskas, J.-S. Huang, and B. Hecht, "Driving plasmonic nanoantennas at perfect impedance matching using generalized coherent perfect absorption," *Nanophotonics*, vol. 10, no. 7, pp. 1879-1887, 2021.
[63] Y. Ren, J. Zhang, X. Gao, X. Zheng, L. P. Zhang, and T. J. Cui, "Miniaturized Spoof Plasmonic Antennas with Good Impedance Matching," *Nanomaterials*, vol. 13, no. 1, 2021.
[64] A. Afridi and Ş. E. Kocabaş, "Beam steering and impedance matching of plasmonic horn nanoantennas," *Optics Express*, vol. 24, no. 22, pp. 25647-25652, 2016.
[65] M. Bettenhausen, S. Grüßing, E. Hardt, J. Flesch, F. Römer, C. A. Chavarin, W. M. Klesse, C. You, J. Piehler, G. Copallini, and B. Witzigmann, "Impedance Matching of THz Plasmonic Antennas," *Journal of Infrared, Millimeter, and Terahertz Waves*, vol. 40, no. 9, pp. 929–942, 2019.
[66] K. Q. da Costa, J. L. Souza, and V. Dmitriev, "Impedance Matching Analysis of Cylindrical Plasmonic Nanoantennas Fed by Optical Transmission Lines," Chapter 12 in Nanoplasmonics - Fundamentals and Applications, *IntechOpen*, 2017.
[67] Y. Sachkou, A. Andryieuski and A. V. Lavrinenko, "Impedance conjugate matching of plasmonic nanoantenna in optical nanocircuits," *Proceedings ELMAR-2011*, Zadar, Croatia, pp. 389-391, 2011.
[68] H.-F. Zhu, J. Li, S.-C. Zhong, L.-H. Du, Q.-W. Shi, B. Peng, H.-K. Yuan, W.-X. Huang, and L.-G. Zhu, "Continuously tuning the impedance matching at the broadband terahertz frequency range in VO_2 thin film," *Optical Materials Express*, vol. 9, no. 1, pp. 315-329, 2019.
[69] J. W. Lee, M.A. Seo, J. Y. Sohn, D. J. Park, Y. H. Ahn and D. S. Kim, "Impedance Matching Plasmonic Metamaterials to Vacuum," *Journal of the Korean Physical Society*, vol. 48, no. 1, pp. 103, 2006.
[70] W. Sun, X. Qin, S. Wang, and Y. Li, "General Guided-Wave Impedance-Matching Networks with Waveguide-Metamaterial Elements," *Physical Review Applied*, vol. 18, no. 3, pp. 034070, 2022.
[71] S. Li, Y. Wang, W. Zhang, W. Lu, B. Hou, J. Luo and Y. Lai, "Observation of wide-angle impedance matching in terahertz photonic crystals," *New Journal of Physics*, vol. 22, no. 2, pp. 023033, 2020.
[72] M. Afzelius and C. Simon, "Impedance-matched cavity quantum memory," *Physical Review A*, vol. 82, no. 2, 022310, 2010.

[73] S. J. Oh, I. Maeng, K. S. Nam, Y. J. Yoon, J.-K. Shim, J. S. Kim, S.-G. Kang, M. Y. Jeon, and H.-C. Ryu, "Exploring the impedance-matching effect in terahertz reflection imaging of skin tissue," *Biomedical Optics Express*, vol. 15, no. 2, pp. 834-842, 2024.
[74] M. Agio and A. Alu, Optical Antennas. Cambridge University Press, 2013.
[75] L. Novotny and N. van Hulst, "Antennas for light," *Nature Photonics*, vol. 5, no. 2, pp. 83–90, 2011.
[76] W. L. Barnes, A. Dereux, and T. W. Ebbesen, "Surface plasmon subwavelength optics," *Nature*, vol. 424, no. 6950, pp. 824–830, 2003.
[77] A. V. Zayats, I. I. Smolyaninov, and A. A. Maradudin, "Nano-optics of surface plasmon polaritons," *Physics Reports*, vol. 408, no. 3-4, pp. 131–314, 2005.
[78] A. Otto, "Excitation of nonradiative surface plasma waves in silver by the method of frustrated total reflection," *Zeitschrift für Physik A hadrons and nuclei*, vol. 216, no. 4, pp. 398–410, 1968.
[79] E. Kretschmann und H. Raether, "Radiative decay of non- radiative surface plasmons excited by light," *Zeitschrift für Naturforschung A*, vol. 23, no. 12, pp. 2135–2136, 1968.
[80] H. Raether, *Surface Plasmons on Smooth and Rough Surfaces and on Gratings*. no. 111 in Springer Tracts in Modern Physics, Springer, 1988.
[81] J. B. Jackson and N. J. Halas, "Surface-enhanced Raman scattering on tunable plasmonic nanoparticle substrates," *Proceedings of the National Academy of Sciences*, vol. 101, no. 52, pp. 17930-17935, 2004.
[82] T. H. Taminiau, F. D. Stefani, F. B. Segerink, and N. F. Van Hulst, "Optical antennas direct single-molecule emission," *Nature Photonics*, vol. 2, no. 4, pp. 234-237, 2008.
[83] W. Murray and W. Barnes, "Plasmonic materials," *Advanced Materials*, vol. 19, no. 22, pp. 3771–3782, 2007.
[84] A. Mohammadi, V. Sandoghdar, and M. Agio, "Gold, copper, silver and aluminum nanoantennas to enhance spontaneous emission," *Journal of Computational and Theoretical Nanoscience*, vol. 6, no. 9, pp. 2024–2030, 2009.
[85] M. Castro-Lopez, D. Brinks, R. Sapienza, and N. F. van Hulst, "Aluminum for nonlinear plasmonics: Resonance-driven polarized luminescence of Al, Ag, and Au nanoantennas," *Nano Letters*, vol. 11, no. 11, pp. 4674–4678, 2011.
[86] J. M. McMahon, G. C. Schatz, and S. K. Gray, "Plasmonics in the ultraviolet with the poor metals Al, Ga, In, Sn, Tl, Pb, and Bi," *Physical Chemistry Chemical Physics*, vol. 15, no. 15, pp. 5415–5423, 2013.
[87] C. F. Bohren und D. R. Huffman, *Absorption and Scattering of Light by Small Particles*. Wiley, 1998.
[88] G. Mie, "Beiträge zur Optik trüber Medien, speziell kolloidaler Metallösungen," *Annalen der Physik*, vol. 330, no. 3, pp. 377–445, 1908.
[89] S. Eustis and M. A. El-Sayed, "Why Gold Nanoparticles Are More Precious than Pretty Gold: Noble Metal Surface Plasmon Resonance and Its Enhancement of the Radiative and Nonradiative Properties of Nanocrystals of Different Shapes," *Chemical Society Reviews*, vol. 35, no. 3, pp. 209–217, 2006.
[90] S. Link and M. A. El-Sayed, "Spectral Properties and Relaxation Dynamics of Surface Plasmon Electronic Oscillations in Gold and Silver Nanodots and Nanorods," *The Journal of Physical Chemistry B*, vol. 103, no. 40, pp. 8410–8426, 1999.
[91] F. Tam, A. L. Chen, J. Kundu, H. Wang, and N. J. Halas, "Mesoscopic Nanoshells: Geometry-Dependent Plasmon Resonances Beyond the Quasistatic Limit," *The Journal of Chemical Physics*, vol. 127, no. 20, pp. 204703, 2007.

[92] J. E. Toney, “Incorporation of Nonlinearity and Dispersion into Time-Dependent Optical Propagation Models,” *The Proceedings of the COMSOL Conference 2008 Boston*, (2008).
[93] U. Kreibig and L. Genzel, “Optical Absorption of Small Metallic Particles,” *Surface Science*, vol. 156, part 2, pp. 678–700, 1985.
[94] S. K. Ghosh and T. Pal, “Interparticle Coupling Effect on the Surface Plasmon Resonance of Gold Nanoparticles: From Theory to Applications,” *Chemical Reviews*, vol. 107, no. 11, pp. 4797–4862, 2007.
[95] C. J. G. Murphy, M. Anand, S. E. Hunyadi, J. W. Stone, P. N. Sisco, A. Alkilany, B. E. Kinard, and P. Hankins, “Chemical Sensing and Imaging with Metallic Nanorods,” *Chemical Communications*, no. 5, pp. 544–557, 2007.
[96] H. R. Gordon, “Light scattering and absorption by randomly-oriented cylinders: dependence on aspect ratio for refractive indices applicable for marine particles,” *Optics Express*, vol. 19, no. 5, pp. 4673-4691, 2011.
[97] X. Lu, M. Rycenga, S. E. Skrabalak, B. Wiley, and Y. Xia, “Chemical Synthesis of Novel Plasmonic Nanoparticles,” *Annual Review of Physical Chemistry*, vol. 60, pp. 167–192, 2009.
[98] B. J. Wiley, S. H. Im, Z.-Y. Li, J. McLellan, A. Siekkinen, and Y. Xia,”Maneuvering the Surface Plasmon Resonance of Silver Nanostructures through Shape-Controlled Synthesis,” *The Journal of Physical Chemistry B*, vol. 110, no. 32, pp. 15666–15675, 2006.
[99] J. Tao, Y.-H. Lu, R.-S. Zheng, K.-Q. Lin, Z.-G. Xie, Z.-F. Luo, S.-L. Li, P. Wang, and H. Ming, “Effect of Aspect Ratio Distribution on Localized Surface Plasmon Resonance Extinction Spectrum of Gold Nanorods,” *Chinese Physics Letters*, vol. 25, no. 12, pp. 4459, 2008.
[100] B. Wiley, Y. Sun, Y. Xia, “Synthesis of Silver Nanostructures with Controlled Shapes and Properties,” *Accounts of Chemical Research Journal*, vol. 40, no. 10, pp. 1067–1076, 2007.
[101] M. Quinten and U. Kreibig, “Optical Properties of Aggregates of Small Metal Particles,” *Surface Science*, vol. 172, no. 5, pp. 557–577, 1986.
[102] T. J. Norman, C. D. Grant, D. Magana, J. Z. Zhang, J. Liu, D. Cao, F. Bridges, A. Van Buuren, “Near Infrared Optical Absorption of Gold Nanoparticle Aggregates,” J. The *Journal of Physical Chemistry B*, vol. 106, no. 28, pp. 7005–7012, 2002.
[103] O. Benson, "Assembly of hybrid photonic architectures from nanophotonic constituents," *Nature*, vol. 480, pp. 193-199, 2011.
[104] A. V. Akimov, A. Mukherjee, C. L. Yu, D. E. Chang, A. S. Zibrov, P. R. Hemme, H. Park, and M. D. Lukin M, “Generation of single optical plasmons in metallic nanowires coupled to quantum dots,” *Nature*, vol. 450, pp. 402-406, 2007.
[105] W. Srituravanich, N. Fang, C. Sun, Q. Luo, and X. Zhang, “Plasmonic nanolithography,” *Nano Letters*, vol. 4, no. 6, pp. 1085–1088, 2004.
[106] J.-P. Berenger, “A perfectly matched layer for the absorption of electromagnetic waves,” *Journal of Computational Physics*, vol. 114, no. 2, pp. 185 – 200, 1994.
[107] S. G. Johnson, “Notes on perfectly matched layers (PMLs),” https://arxiv.org/pdf/2108.05348, 2008.
[108] P. Monk, *Finite Element Methods for Maxwells Equations*. Numerical mathematics and scientific computation; Oxford science publications, Oxford: Clarendon Press, repr. ed., 2008.

[109] G. Veronis and S. Fan, “Overview of simulation techniques for plasmonic devices in Surface Plasmon Nanophotonics,” *Springer Netherlands*, pp. 169–182, 2007.
[110] M. N. O. Sadiku, *Numerical Techniques in Electromagnetics 2nd ed*. CRC Press, New York, 2001.
[111] “http://www.comsol.com,” (2016).
[112] Y. Saad, *Iterative Methods for Sparse Linear Systems*. Society for Industrial and Applied Mathematics, 2003.
[113] O. C. Zienkiewicz, R. L. Taylor, and J. Z. Zhu, *Finite element method: its basis and fundamentals*. Butterworth Heinemann, 2005.
[114] M. D. Wissert, A. W. Schell, K. S. Ilin, M. Siegel, and H.-J. Eisler, “Nanoengineering and characterization of gold dipole nanoantennas with enhanced integrated scattering properties,” *Nanotechnology*, vol. 20, no. 42, pp. 425203, 2009.
[115] K.Dopf, C.Moosmann, S.W.Kettlitz, P.M.Schwab, K.Ilin, M.Siegel, U.Lemmer, and H.-J.Eisler, “Coupled T-Shaped Optical Antennas with Two Resonances Localized in a Common Nanogap,” *ACS Photonics*, vol .2, no, 11, pp. 1644–1651, 2015.
[116] P.M.Schwab,,C.Moosmann, M.D.Wissert, E.W.-G. Schmidt, K.S.Ilin, M.Siegel, U.Lemmer, and H.-J. Eisler, “Linear and Nonlinear Optical Characterization of Aluminum Nanoantennas,” *Nano Letters*, 2013, vol. 13, no. 4, pp. 1535–1540, 2013.
[117] L. Novotny, “Effective Wavelength Scaling for Optical Antennas,” *Physical Review Letters*, vol 98, no. 26, pp. 266802, 2007.
[118] “http://www.lumerical.com,” (2013).
[119] J. Babinet, “Sur les couleurs des réseaux,” *Annales de chimie et de physique*, vol. 40, 1829.
[120] C.-C. Chen, “Transmission Through a Conducting Screen Perforated Periodically with Apertures,” *IEEE Transactions on Microwave Theory and Techniques*, vol. 18, no. 9, pp. 627–632, 1970.
[121] T. Ebbesen, H. Lezec, H. F. Ghaemi, T. Thio, und P. Wolff, “Extraordinary optical transmission through sub-wavelength hole arrays,” *Nature*, vol. 391, pp. 667–669, 1998.
[122] John Volakis, *Antenna engineering handbook*. McGraw-Hill, 2007.
[123] E. Schubert, *Antennenarrays aus Hohlleiterschlitzen für das 35GHz Band*. Hochschule für Telekommunikation Leipzig
[124] H. M. El Misilmani, M. Al-Husseini, K. Y. Kabalan and A. El-Hajj, "A design procedure for slotted waveguide antennas with specified sidelobe levels," *International Conference on High Performance Computing & Simulation (HPCS)*, pp. 828-832, 2014.
[125] U. Petri, *Die Berechnung von geschlitzten Koaxialkabeln für den UKW-Funk*. Dissertation Technische Hochschule Aachen, 1977.
[126] J. Wang, Y. Li, Z. Zhang, and M. Chen, “Radiation mechanism and polarization properties of leaky coaxial cables,” *Radio Science*, vol. 46, no. 2, pp. 1–12, 2011.
[127] C. Enkrich, M. Wegener, S. Linden, S. Burger, L. Zschiedrich, F. Schmidt, J. F. Zhou, T. Koschny, and C. M. Soukoulis, “Magnetic Metamaterials at Telecommunication and Visible Frequencies,” *Physical Review Letters*, vol. 95, no. 20, pp. 203901, 2005.
[128] X. Luo, Y. Xing, D. D. Galvan, E. Zheng, P. Wu, C. Cai, and Q. Yu, “Plasmonic Gold Nanohole Array for Surface-Enhanced Raman Scattering Detection of DNA Methylation,” *ACS Sensors*, vol. 4, no. 6, pp. 1534 −1542, 2019

[129] Q. Yu, G. Guan, D. Qin, G. Golden, and P. G. Wallace, “Inverted Size-Dependence of Surface-Enhanced Raman Scattering on Gold Nanohole and Nanodisk Arrays,” *Nano Letters*, vol. 8, no. 7, pp. 1923 – 1928, 2008.
[130] A. G. Brolo, E. Arctander, R. Gordon, B. Leathem, and K. L. Kavanagh, “Nanohole-Enhanced Raman Scattering,” *Nano Letters*, vol. 4, no. 10, pp. 2015 – 2018, 2004.
[131] Q. Yu, S. Braswell, B. Christin, J. Xu J., P. M. Wallace, H. Gong, and D. Kaminsky, *“*Surface-enhanced Raman scattering on gold quasi-3D nanostructure and 2D nanohole arrays,” *Nanotechnology*, vol. 21, no. 35, pp. 355301, 2010.
[132] P. Zheng, S. K. Cushing, S. Suri, and N. Wu, “Tailoring plasmonic properties of gold nanohole arrays for surface-enhanced Raman scattering,” *Physical Chemistry Chemical Physics*, vol. 17, pp. 21211–21219, 2015.
[133] Y. Park, J. Kim, Y.-G. Roh, and Q.-H. Park, "Optical slot antennas and their applications to photonic devices," *Nanophotonics*, vol. 7, no. 10, pp. 1617-1636, 2018.
[134] H. Guo, T. P. Meyrath, T. Zentgraf, N. Liu, L. Fu, H. Schweizer, and H. Giessen, “Optical resonances of bowtie slot antennas and their geometry and material dependence,” *Optics Express*, vol. 16, no. 11, pp. 7756–7766, 2008.
[135] R. Gordon, A. G. Brolo, A. McKinnon, A. Rajora, B. Leathem, and K. L. Kavanagh, “Strong polarization in the optical transmission through elliptical nanohole arrays,” *Physical Review Letters*, vol. 92, no. 3, pp. 037401, 2004.
[136] L. Y. Wu, B. M. Ross, and L. P. Lee, "Optical Properties of the Crescent-Shaped Nanohole Antenna,” *Nano Letters*, vol 9, no. 5, pp. 1956 – 1961, 2009.
[137] J. Yang, S. Zhou, C. Hu, W. Zhang, X. Xiao, and J. Zhang, “Broadband spin-controlled surface plasmon polariton launching and radiation via L-shaped optical slot nanoantennas,” *Laser Photonics Review*, vol. 8, pp. 590–595, 2014.
[138] Y. Xu, B. Gao, A. He, T. Zhang, and J. Zhang, "Three-dimensional plasmonic nano-router via optical antennas," *Nanophotonics*, vol. 10, no. 7, pp. 1931-1939, 2021.